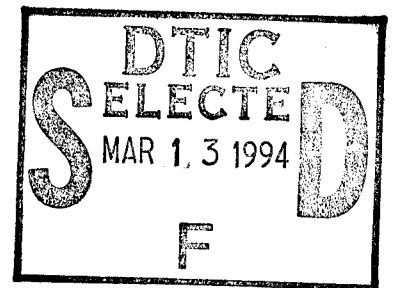# NAVAL POSTGRADUATE SCHOOL

Monterey, California

THESIS

SPACECRAFT ATTITUDE CONTROL SYSTEM PERFORMANCE USING PULSE-WIDTH PULSE-FREQUENCY MODULATED THRUSTERS

by

Robert S. McClelland

March, 1994

Thesis Advisor: Prof. Brij N. Agrawal

19950308 017

REPORT DOCUMENTATION PAGE		Form Approved OMB No. 0704-0188

1a. REPORT SECURITY CLASSIFICATION Unclassified		1b. RESTRICTIVE MARKINGS	
2a. SECURITY CLASSIFICATION AUTHORITY		3. DISTRIBUTION/AVAILABILITY OF REPORT Approved for public release; distribution is unlimited.	
2b. DECLASSIFICATION/DOWNGRADING SCHEDULE			
4. PERFORMING ORGANIZATION REPORT NUMBER(S)		5. MONITORING ORGANIZATION REPORT NUMBER(S)	
6a. NAME OF PERFORMING ORGANIZATION Naval Postgraduate School	6b. OFFICE SYMBOL (If applicable) 31	7a. NAME OF MONITORING ORGANIZATION Naval Postgraduate School	
6c. ADDRESS (City, State, and ZIP Code) Monterey, CA 93943-5000		7b. ADDRESS (City, State, and ZIP Code) Monterey, CA 93943-5000	
8a. NAME OF FUNDING/SPONSORING ORGANIZATION	8b. OFFICE SYMBOL (If applicable)	9. PROCUREMENT INSTRUMENT IDENTIFICATION NUMBER	
8c. ADDRESS (City, State, and ZIP Code)		10. SOURCE OF FUNDING NUMBERS	

	PROGRAM ELEMENT NO.	PROJECT NO.	TASK NO.	WORK UNIT ACCESSION NO.

11. TITLE (Include Security Classification)
SPACECRAFT ATTITUDE CONTROL SYSTEM PERFORMANCE USING PULSE-WIDTH PULSE-FREQUENCY MODULATED THRUSTERS

12. PERSONAL AUTHOR(S)
Robert S. McClelland

13a. TYPE OF REPORT Master's Thesis	13b. TIME COVERED FROM _____ TO _____	14. DATE OF REPORT (Year,Month,Day) March 1994	15. PAGE COUNT 102

16. SUPPLEMENTARY NOTATION
The views expressed in this thesis are those of the author and do not reflect the official policy or position of the Department of Defense or the U.S. Government.

17. COSATI CODES			18. SUBJECT TERMS (Continue on reverse if necessary and identify by block number)
FIELD	GROUP	SUB-GROUP	Attitude Control; Flexible Spacecraft; Thrust-Modulation

19. ABSTRACT (Continue on reverse if necessary and identify by block number)

Many current satellites employ on-off thrusters to accomplish attitude control tasks which may include initial acquisition, rotational maneuvers, and on-orbit stabilization. This work shows that the use of pulse-width pulse-frequency (PWPF)-modulated thrusters provides several important advantages over conventional bang-bang thruster control methods, including less thruster activity and closer-to-linear actuation. The PWPF modulator is implemented in simulations using the $Matrix_x$/Systembuild software package. Simulations assuming a rigid spacecraft are first performed to compare the performance of the PWPF-modulated thrust controller with that of conventional bang-bang and time-optimal bang-bang controllers. The discussion is then extended to the case of a spacecraft with structural flexibility, as is encountered quite often in three-axis stabilized vehicles with large fold-out solar arrays. Simulations for comparison of the controllers are performed using the flexible spacecraft dynamics model. The control loop design in the presence of flexibility and possible interaction with the PWPF modulator nonlinearity are addressed. Using a describing function model of the modulator, stability margin with respect to the structural mode limit cycle is predicted. Simulations are then conducted to verify the predicted stability margin.

DTIC QUALITY

20. DISTRIBUTION/AVAILABILITY OF ABSTRACT [X] UNCLASSIFIED/UNLIMITED [ ] SAME AS RPT. [ ] DTIC USERS	21. ABSTRACT SECURITY CLASSIFICATION Unclassified	
22a. NAME OF RESPONSIBLE INDIVIDUAL Brij N. Agrawal	22b. TELEPHONE (Include Area Code) (408) 656-3338	22c. OFFICE SYMBOL AA/Ag

SPACECRAFT ATTITUDE CONTROL SYSTEM PERFORMANCE USING PULSE-WIDTH PULSE-FREQUENCY MODULATED THRUSTERS

by

Robert S. McClelland
Naval Research Laboratory
B.S. Aerospace Engineering, Virginia Polytechnic Institute and State University, 1988
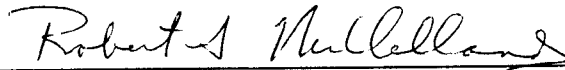
Submitted in partial fulfillment of the requirements for the
degree of
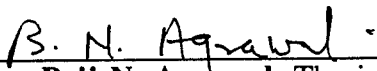
MASTER OF SCIENCE IN MECHANICAL ENGINEERING

from the
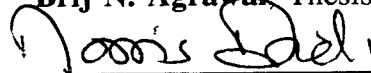
NAVAL POSTGRADUATE SCHOOL
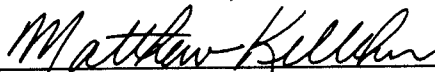## March 1994

Author: _____
Robert S. McClelland

Approved by: _____
Brij N. Agrawal, Thesis Advisor

_____
Morris Driels, Second Reader

_____
Matthew D. Kelleher, Chairman,
Department of Mechanical Engineering

ii

ABSTRACT

Many current satellites employ on-off thrusters to accomplish attitude control tasks which may include initial acquisition, rotational maneuvers, and on-orbit stabilization. This work shows that the use of pulse-width pulse-frequency (PWPF)-modulated thrusters provides several important advantages over conventional bang-bang thruster control methods, including less thruster activity and closer-to-linear actuation. The PWPF modulator is implemented in simulations using the Matrix$_x$/Systembuild software package. Simulations assuming a rigid spacecraft are first performed to compare the performance of the PWPF-modulated thrust controller with that of conventional bang-bang and time-optimal bang-bang controllers. The discussion is then extended to the case of a spacecraft with structural flexibility, as is encountered quite often in three-axis stabilized vehicles with large fold-out solar arrays. Simulations for comparison of the controllers are performed using the flexible spacecraft dynamics model. The control loop design in the presence of flexibility and possible interaction with the PWPF modulator nonlinearity are addressed. Using a describing function model of the modulator, stability margin with respect to the structural mode limit cycle is predicted. Simulations are then conducted to verify the predicted stability margin.

Accesion For		
NTIS CRA&I	N	
DTIC TAB	☐	
Unannounced	☐	
Justification		
By		
Distribution /		
Availability Codes		
Dist	Avail and / or Special	
A-1		

iii

TABLE OF CONTENTS

I. INTRODUCTION

A. REASON FOR RESEARCH

This work was performed in support of ongoing research in flexible spacecraft dynamics and control being conducted under the direction of Dr. Brij Agrawal. Justification is presented for implementing pulse-width pulse-frequency (PWPF) modulated thruster control as an alternative to conventional bang-bang control methods. The goal was to provide smoother control for improved pointing accuracy with less thruster activation and reduced excitation of the elastic modes of vibration. Simulation and analysis are presented to illustrate the improvement afforded by PWPF modulation and to address the stability issues which arise in the presence of nonlinear actuation. The research provides foundation for future thruster control experiments using the Spacecraft Dynamics Laboratory facilities.

B. BACKGROUND

1. Attitude Control System Overview

A satellite attitude control system (ACS) is employed to provide vehicle acquisition, rotation maneuvers, and on-orbit stabilization. In acquisition, the control system acts to null initial angular velocity errors and bring the spacecraft to its operational configuration. This situation is often encountered immediately after spacecraft separation from the final launch vehicle stage, whereby the separation event has introduced initial angular rates. Rotational (or slewing) maneuvers are sometimes performed to reorient the spacecraft to meet mission objectives, or to prepare for translational propulsive maneuvers. On-orbit stabilization refers to the nominal mode of operation whereby the control system

1

typically acts in the regulator mode to maintain a particular pointing attitude with respect to the earth.

An ACS must provide stability under the influence of various types of external disturbance torques. These may include the secular disturbance due to thrust misalignment during a translational propulsive maneuver, or cyclical environmental torques, e.g. from solar pressure or gravity gradient. Internal disturbances are applied by the motion of satellite components such as steerable antennas, sensor suites or sun-tracking solar arrays.

2. Introduction to Thruster Attitude Control

Most modern satellite attitude control systems incorporate several types of actuators to include both internal momentum exchange devices (e.g. momentum wheels, reaction wheels, control moment gyros) along with a complement of thrusters. Thrusters are used in situations when disturbance torques exceed the control authority of the momentum exchange devices, and are often capable of much faster reorientation maneuvers. PWPF-modulated thrusters have been used to maintain stability during translational maneuvers [Reference 1].

Momentum exchange type actuators can usually be treated as proportional devices. On the other hand, thrusters are typically on-off devices, only capable of providing a single fixed thrust level. Because this is inherently nonlinear actuation, thruster control systems cannot be analyzed in the same systematic and straightforward manner as a linear system. Response characteristics are not scalable as with a linear system, but rather are highly dependent on input amplitude. By considering the system operation for the various attitude control modes (i.e., various levels of error signal amplitude), a general understanding of the control system behavior can be obtained.

The main concern in design of a thruster control system is in performing the control operations within the required accuracy, with the least amount of thruster activity. Lower thruster activity directly translates into lower propellant consumption and less

thruster/ valve wear. Thus mission benefits such as longer mission life and/or more available payload weight for the same amount of fuel can be realized.

3. The Complication of Flexibility

Structural flexibility must be addressed in ACS design. In the presence of the flexibility, the possibility exists that natural frequencies of the structure can fall within the control bandwidth. This can lead to control-structure interaction problems which compromise the stability and pointing accuracy objectives (and possibly harm the structure). The dominant natural frequencies of vibration must be predicted, which often requires finite element modeling of the structure. The nonlinearity of the thruster-actuated control system can interact with the flexibility, resulting in self-sustained oscillation of the structure and back-and-forth thruster activity.

II. THRUSTER ATTITUDE CONTROL SYSTEM DESCRIPTION

A. SIMPLE BANG-BANG CONTROL SYSTEM

The block diagram representation of a simple satellite bang-bang control system with angular position and rate feedback is shown in **Figure 1**. The satellite, depicted in **Figure 2**, is modeled as a rigid rotational inertia which is controlled by a complement of thrusters which provide either a positive or negative torque of constant magnitude U or $-U$ [adapted from Reference 2].

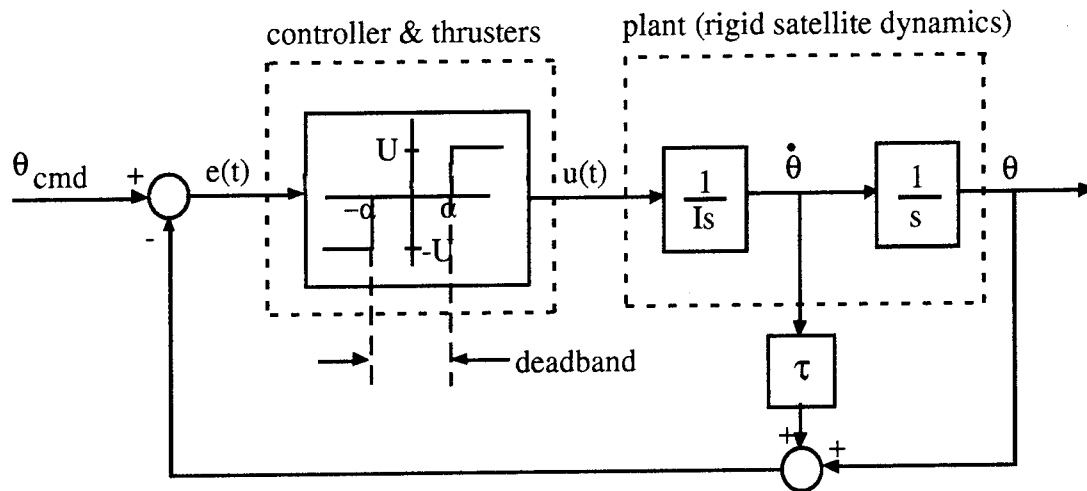**Figure 1. Bang-Bang Attitude Control System**

Here s is the Laplace variable, I is the total spacecraft inertia, θ is the controlled satellite pointing angle, and the factor $1/Is^2$ is the familiar s-domain representation of the rigid body dynamics. The control torque of magnitude $+/-U$ is commanded based on the sign of the error signal, $e(t)$, which is
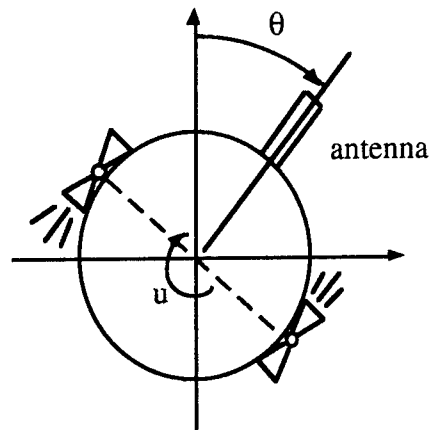

Figure 2. Simple Satellite

4

a combination of gained velocity and position error. For this system the controller is defined by

$$u(t) = \begin{cases} U\ sgn(e(t)) & \text{if } |e(t)| \geq \alpha \\ 0 & \text{if } |e(t)| < \alpha \end{cases}$$

where   (1)

$$e(t) = \theta_{ref} - \theta(t) - a\dot{\theta}(t)$$

and α is the deadband half-width

A phase plane trajectory for the control system of **Figure 1**, ignoring the deadband for now, is shown in **Figure 3**. Since rate feedback introduces damping to the system, the phase plane trajectory shows that the time response decays toward the origin where both rate and position are zero. In the absence of rate feedback the system is marginally stable, with undamped oscillation occurring with a unique amplitude for each unique initial condition.
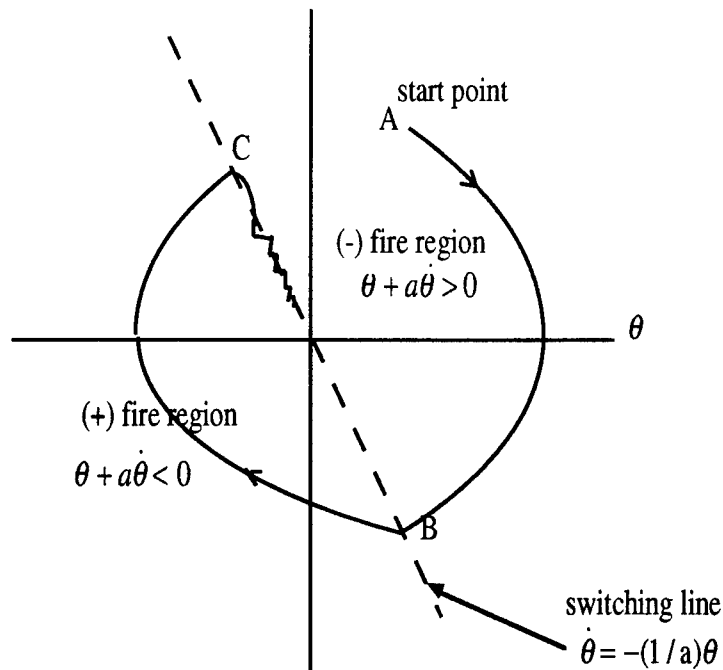

Figure 3. Phase Trajectory for Damped Thruster ACS with No Deadband

Note that the switching line with no deadband passes through the origin of the phase space. Each period of constant thrust, from starting point A to switching point B, and from point B to switching point C, etc., forms a parabola in the phase space [Reference 3].

1. The Limit Cycle

A limit cycle can be described as a self-sustained oscillation condition which arises in nonlinear systems. Viewed in terms of the phase plane trajectory, a limit cycle is a closed path which is approached from a starting condition either from inside the closed path (usually with the exception of the origin), or from the outside. The system trajectory will continue to trace the limit cycle path ad infinitum (given that it is a stable limit cycle). In thruster control, the "rigid body" limit cycle is due to the minimum on-time of the thruster (the "structural mode" limit cycle due to the interaction of the nonlinearity with a flexible structure is discussed in Chapter V) . Consider the phase trajectory of **Figure 4**, the trajectory near the origin of the phase space for the bang-bang controller of **Figure 1**.
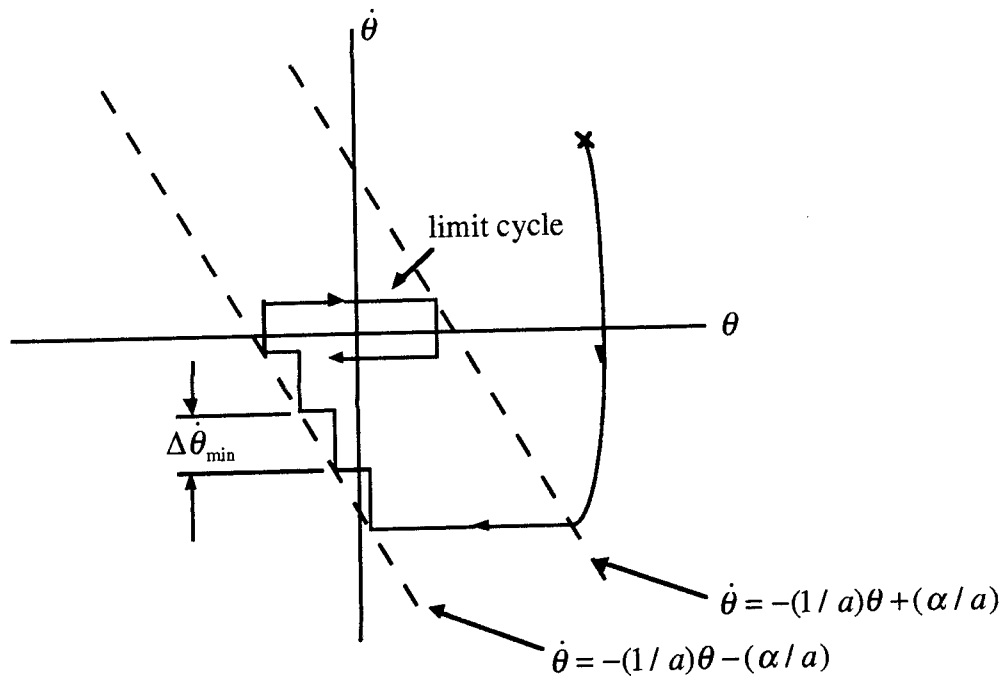

Figure 4. Phase Trajectory in Limit Cycle Region with Dead Band

6

The deadband affords periods of coasting which are represented as horizontal lines in the phase plot. Each vertical segment (actually a small section of a parabola) corresponds to a thruster pulse. Due to the minimum on-time of the thrust, the minimum impulse and hence minimum change in rate, $\Delta\dot{\theta}_{min}$, produces the ladder-step approach toward the origin. It is this minimum on-time or minimum impulse of the thrusters which produces the limit cycle seen near the origin. Note that a trajectory starting from inside the limit cycle boundary will also eventually end up in the limit cycle condition (assuming a nonzero rate). The frequency of the limit cycle is of great concern to the thruster control system designer because it dictates the fuel usage for the nominal mode of operation which is the predominant mode through the life of the satellite. However, the desire for a minimum frequency limit cycle is often in conflict with the pointing requirements since a tighter requirement on θ for instance will result in less coast period and hence higher limit cycle frequency. Note that in **Figure 3**, after switching point C the absence of the deadband and associated coast periods cause "chatter" in the approach to the origin. This is wasteful of fuel, and upon arrival in the region of the origin, the limit cycle is of much greater frequency than in the system with the deadband.

2. Time-Optimal Bang-Bang Control

Time-optimal bang-bang control for a rest-to-rest maneuver is accomplished using the control law

$$u(t) = -Usgn\left[\theta - \theta_{cmd} + \frac{I\dot{\theta}|\dot{\theta}|}{2U}\right] \qquad (2)$$

where all terms are defined as in Figure 1.

For any initial condition the phase plane trajectory consists of two parabolas with a single switching point, corresponding to full-on acceleration until the half-time of the maneuver, followed by full-on deceleration along the second parabolic trajectory straight to

the origin. This maneuver has been studied and modified in many reports, since it is the most time-efficient approach.

B. PULSE-WIDTH PULSE-FREQUENCY MODULATION

Most thrusters used for attitude control are designed for on-off operation. Pulse-width pulse-frequency (PWPF) modulation provides a means of producing a variable average thrust using a simple on-off thruster, hence an approximation to proportional control is achieved.

A PWPF modulator is depicted in **Figure 5**. The average output of the pulse train is approximately proportional to the demanded torque input. Other forms of pulse modulation, for instance pulse width (or pulse frequency) or derived rate modulation are used in other applications which are not considered here.
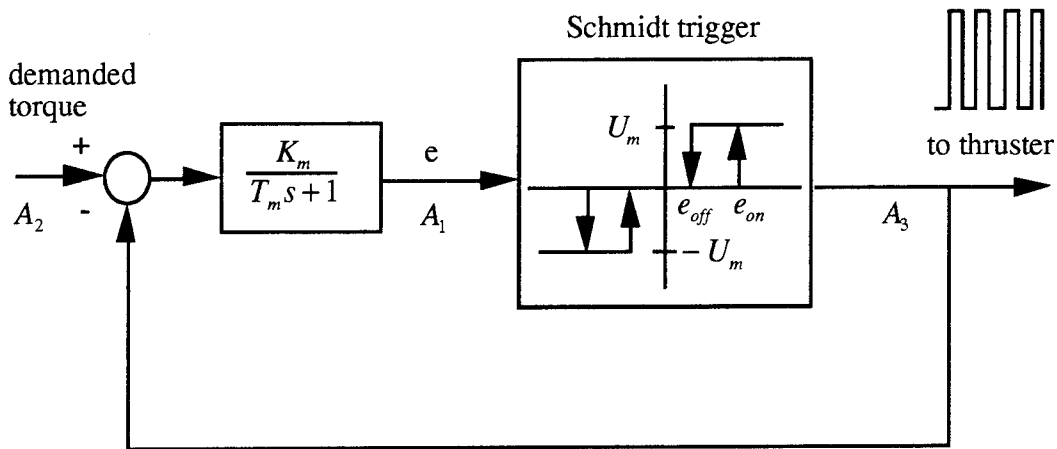

Figure 5. PWPF Modulator

The modulator includes a relay with dead-zone and hysteresis, or Schmidt trigger, and an integrator (filter). A limiter after the filter was included in the digital implementation. The feedback from the output of the relay is subtracted from the input signal A_2. The formation of pulses can be explained with the aid of **Figure 6**, which depicts the output of the discretized modulator and the filter used in this study, for a constant input. The filter

8

integrates the error signal $(A_2 - A_3)$. Before the formation of a pulse the feedback from the relay is zero. So the magnitude of A_2 determines the rate of integration, and thus the rate of growth of the output of the filter. When the filter output reaches the threshold e_{on} of the Schmidt trigger, the relay switches on and turns on the thruster. The feedback signal then resets the integrator at a rate proportional to $(U_m - A_2)$ until the filter output falls below e_{off} at which time the thruster signal is turned off and the feedback signal is again zeroed out. Note that the appearance of the pulses as being other than square is due to the integration time step of 10 milliseconds. The first pulse is commanded on at .06 seconds and commanded off at .08 seconds.
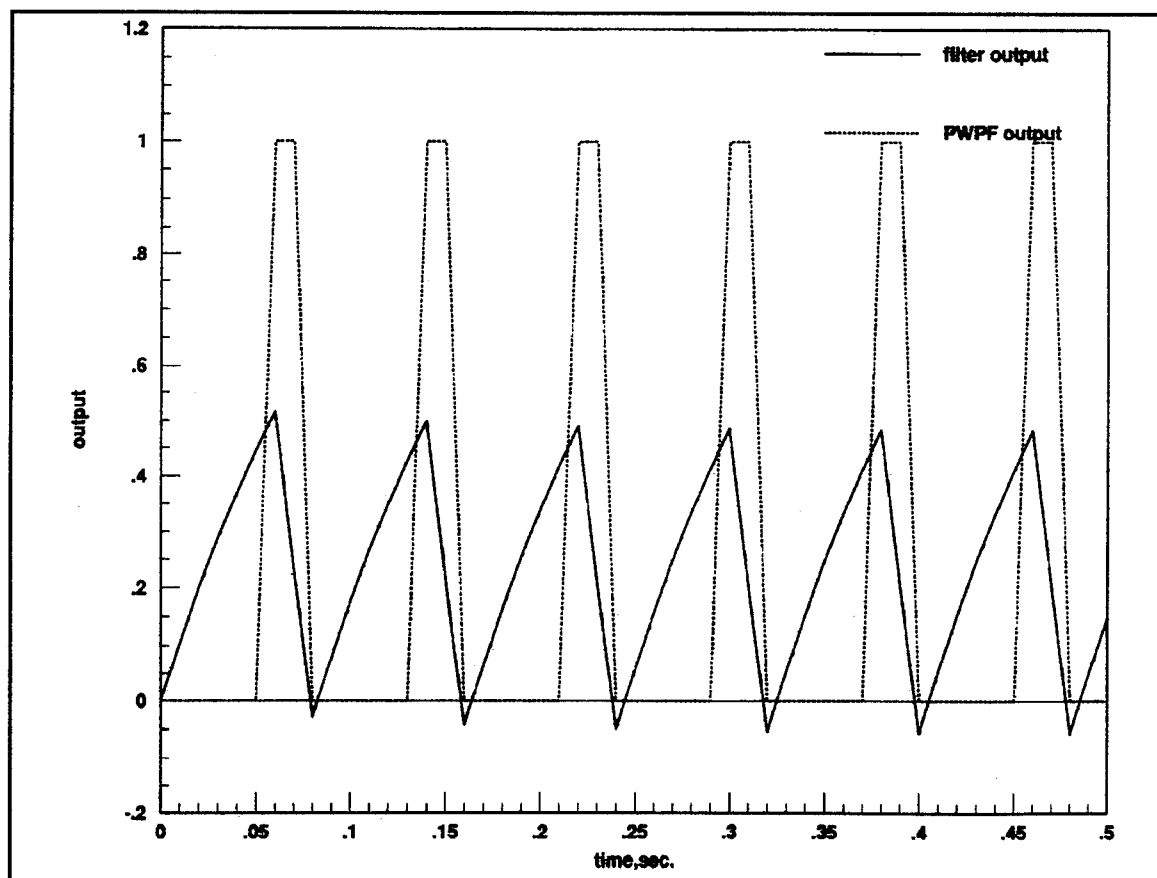

Figure 6. PWPF Modulator Output for Constant Input

9

Reference 1 notes the modulator tends to contribute control loop gain reduction at low frequency and phase lag at higher frequency, and presents design parameters based on tradeoffs between phase lag and internal deadband size:

$$K_m = 4.5$$
$$T_m = 0.12976$$
$$e_{on} = 0.45 \tag{3}$$
$$e_{off} = 0.15$$
$$U_m = 1.0$$

The modulator was discretized for digital simulation. Using the signal labels from Figure 5, the filter output can be written

$$A_1 = (A_2 - A_3)\frac{K}{1+sT} \tag{4}$$

Considering the signal at two consecutive time steps n and $(n+1)$, and replacing the Laplace variable with its time equivalent (a discrete-time first derivative), Equation (4) can be reformulated as

$$(A_2 - A_3)K = A_1 + sA_1T$$
$$= A_1(n) + \frac{A_1(n+1) - A_1(n)}{dt} \times T \tag{5}$$

Solving for the new value of the filter output,

$$A_1(n+1) = \frac{A_2(n+1) - A_3(n)}{T}Kdt + A_1(n) \times \left(1 - \frac{dt}{T}\right) \tag{6}$$

where dt is the sampling interval of the digital simulation to represent the modulator, which is chosen to produce a minimum on-time or minimum pulse width of dt. The digital implementation of the modulator is included in **Appendix A**. Simulation of the PWPF

10

modulator was performed using a sampling interval of 10 milliseconds. **Figure 7** illustrates operation of the modulator for two sinusoidal inputs and a ramp.
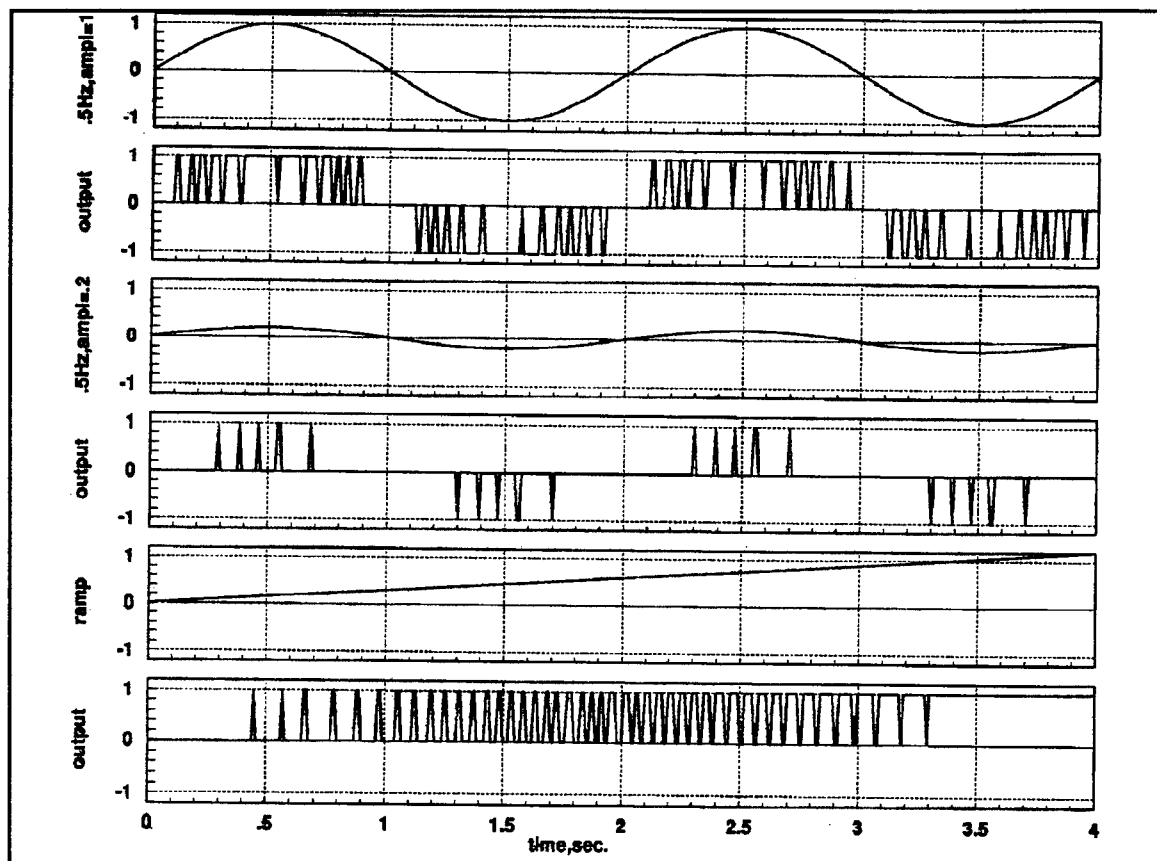

Figure 7. PWPF Modulator Output for Various Inputs

The modulation factor or duty cycle is defined as the average output of the modulator. Pulse trains for various constant inputs were analyzed to verify the expected linear relationship between input and duty cycle. The pulse trains are included in **Appendix A**. Once the pulse width and frequency are determined, the duty cycle is simply determined by:

$$duty\ cycle = pulse\ width \times pulse\ frequency \qquad (7)$$

The output characteristics are tabulated in **Table 1** and shown graphically in **Figure 8**. The gains computed in the table are the average values of the duty cycle for a given input.

11

TABLE 1. MODULATOR RESPONSE TO CONSTANT INPUTS

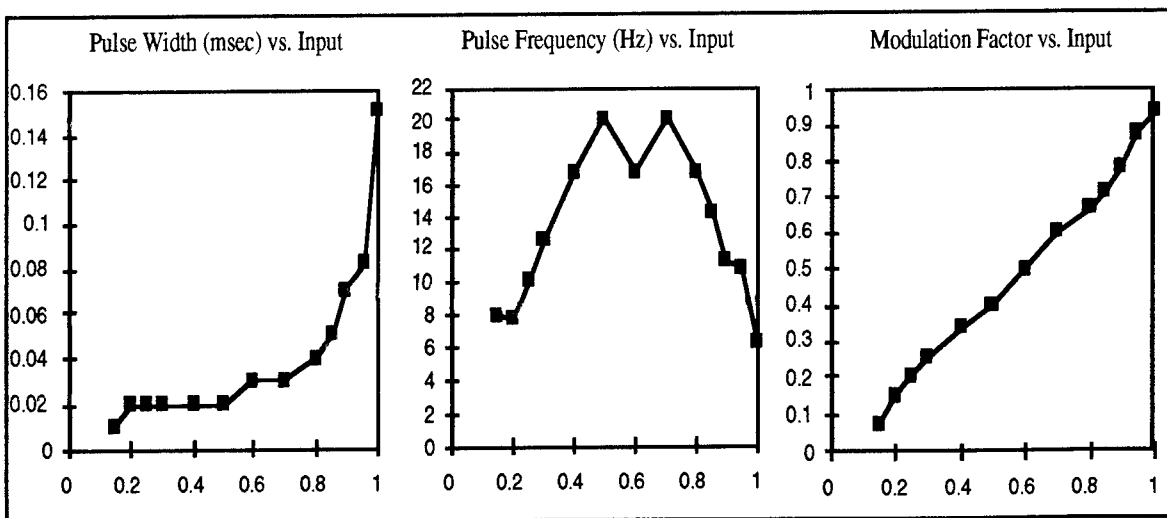| INPUT	DUTY CYCLE (10 msec)	PULSE WIDTH (msec)	PERIOD (msec)	FREQUENCY (Hz)	GAIN
0.15	1/13 (50%)	10	125	8	0.08
	1/12 (50%)				
0.2	2/13	20	130	7.69	0.15
0.25	2/10	20	100	10	0.2
0.3	2/8	20	80	12.5	0.25
0.4	2/6	20	60	16.67	0.33
0.5	2/5	20	50	20	0.40
0.6	3/6	30	60	16.67	0.5
0.7	3/5	30	50	20	0.6
0.8	4/6	40	60	16.67	0.67
0.85	5/7	50	70	14.29	0.71
0.9	7/9	70	90	11.11	0.78
0.95	8/9 (64.2%)	81.8	93.6	10.69	0.87
	8/10 (17.9%)				
	9/10 (17.9%)				
1	15/16 (80.7%)	152	162	6.17	0.94
	16/17 (19.3%)				
1.05	continuous				

Figure 8. Output Pulse Width, Pulse Frequency, and Duty Cycle

12

The modulation factor versus input graph of **Figure 8** verifies the nearly proportional operation. Note that the modulator has an internal deadband, whereby a pulse will not be triggered for an input signal lower than about *0.15*. It is important to remember that even though the output relationship is fairly linear, the relay constitutes a hard nonlinearity and hence nonlinear analysis must be employed to study the details of control system performance.

C. INTRODUCTION TO SIMULATIONS

Digital simulations were used for verifying basic control system operation, comparing the performance of different types of thruster control, and exploring system response with structural flexibility and variation of various parameters. In most cases simplified block diagrams are included in the text portion of the thesis for clarity and ease of interpretation, with corresponding $Matrix_x$/Systembuild block diagrams included in **Appendix B**. All simulations were performed for the single axis control case, neglecting cross-axis momentum coupling effects. Hence the rigid body equation of motion is simply:

$$I\ddot{\theta} = T_c \qquad (8)$$

from which the Laplace transform yields the s-domain transfer function representation:

$$\frac{\Theta(s)}{T_c(s)} = \frac{1}{Is^2} \qquad (9)$$

where θ is the controlled pointing angle, I is the total moment of inertia, and T_C the control torque. For the case of thruster control T_C is approximated as a square pulse.

Unless otherwise noted, all block diagram elements were discretized with a sampling interval of 10 milliseconds. This enforced the minimum on-time of the thruster, while providing a sample rate fast enough to sufficiently capture the dynamic response.

13

All simulations were run using the parameters of the flexible spacecraft simulator (FSS) experimental system (but assumed a rigid body for the simulations of Chapter III). The values used for total moment of inertia and thruster control torque were 11.4 kg-m^2 and 0.35 N-m, respectively. The FSS was designed as a scale version of the pitch axis of a typical geosynchronous momentum-biased satellite, so that results representative of a realistic satellite control system could be expected. Indeed these values scale nicely to the pitch axis inertia and control torque values (440 kg-m^2 and 10 N-m) for the operational satellite of Reference 1.

A pointing accuracy goal of +/- .1 degrees was used throughout the study as a basis for comparison. This is a realistic (if not lenient) requirement for a communications satellite at geosynchronous altitude.

III. COMPARISON OF THRUSTER CONTROL METHODS FOR RIGID SPACECRAFT

Simulations were run to demonstrate the performance of the pulse modulated control system and to compare it with the performance of bang-bang control systems. A block diagram control system representation for rigid body simulations is shown in **Figure 9**. Implementation of the pulse modulator involved replacing the elements from Figure 5 with a single Usercode Block in Systembuild which calls the FORTRAN routine for the discrete modulator in each integration step. For the time-optimal bang-bang control system the
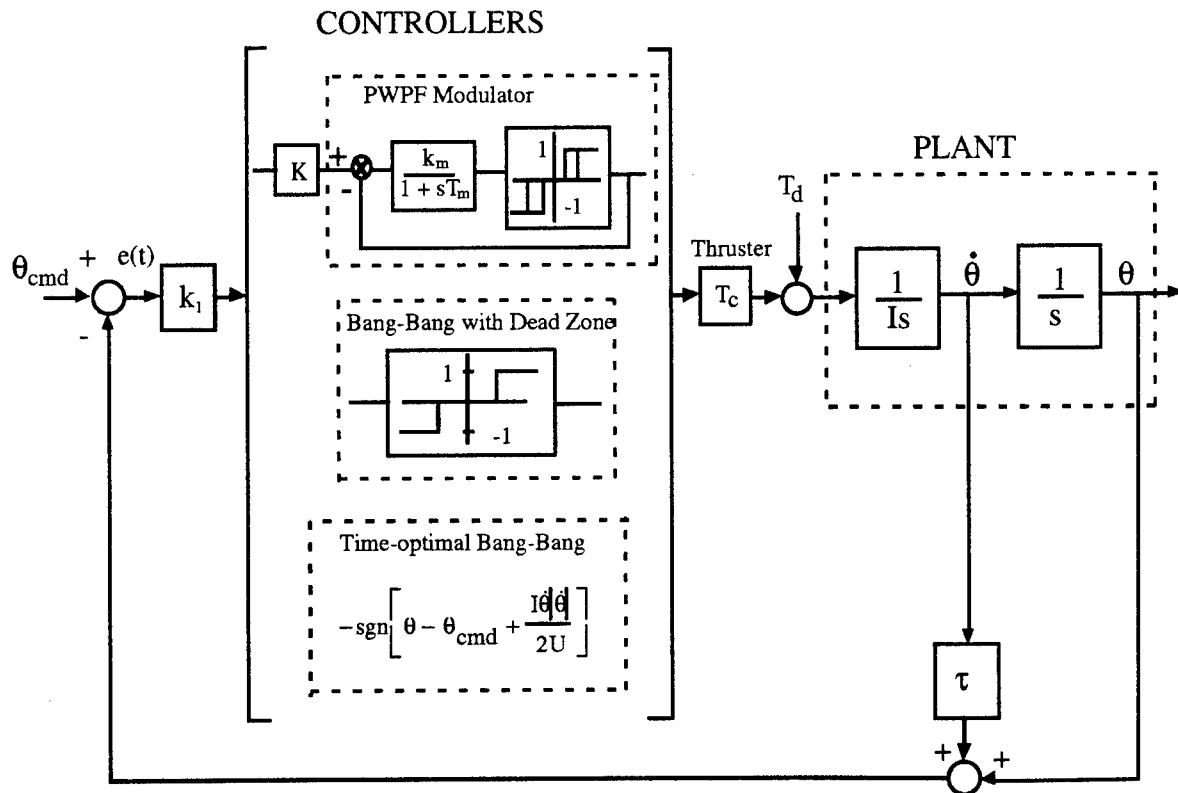

Figure 9. Attitude Control Systems for Rigid Body Simulations

feedback gain and forward loop gain are not applicable. A linear (non-thruster) controller with position and rate feedback would bypass the controllers and the thruster block. The PWPF modulator incorporates an additional gain K which will be considered separately from the gain k_1. The disturbance torque T_d is included in some simulations. The error signal, $e(t)$, includes the error between the commanded angular position and the actual angular position, and the error between the commanded and actual angular rates where the commanded rate is always implicitly zero.

The linear controller was used to size gains for a particular desired performance. The same gains were then used with the nonlinear controllers and for the simulations with flexible dynamics, in order to form a basis for comparison. The closed loop transfer function of the system for the case of linear actuation is:

$$\frac{\Theta_{out}(s)}{\Theta_{ref}(s)} = \frac{k_1/I}{s^2 + \frac{k_1\tau}{I}s + \frac{k_1}{I}} \tag{10}$$

The equation is of the same form as the general equation for a viscously damped single-degree-of-freedom system,

$$\frac{\omega_n^2}{s^2 + 2\zeta\omega_n s + \omega_n^2} \tag{11}$$

where ζ and ω_n are the damping ratio and natural frequency, respectively. Equating coefficients of (10) and (11) it follows that

$$\omega_n = \sqrt{\frac{k_1}{I}} \qquad \text{and} \qquad \zeta = \frac{\tau}{2}\sqrt{\frac{k_1}{I}} \tag{12}$$

For the linear design a damping factor of .84 was chosen for minimal overshoot. The value of ω_n can be thought of as the control bandwidth, and was selected as .06 Hz in order to minimize interaction with the first pole and zero of the flexible dynamics in later

16

simulations (.12Hz and .15Hz, respectively). Based on these values Equations (12) yield the gain values

$$k_1 = 1.4 \quad \text{N-m/rad}$$

$$k_1\tau = 6.7 \quad \text{N-m-s/rad}$$

The response to a ten degree step input with linear actuation is shown below in **Figure 10**. Graphs are shown for angular position in degrees, angular rate in degrees per second, the gained error signal $k_1e(t)$, and the phase plane trajectory. A 2% settling time of 13.6 seconds is achieved, with less than one percent overshoot.
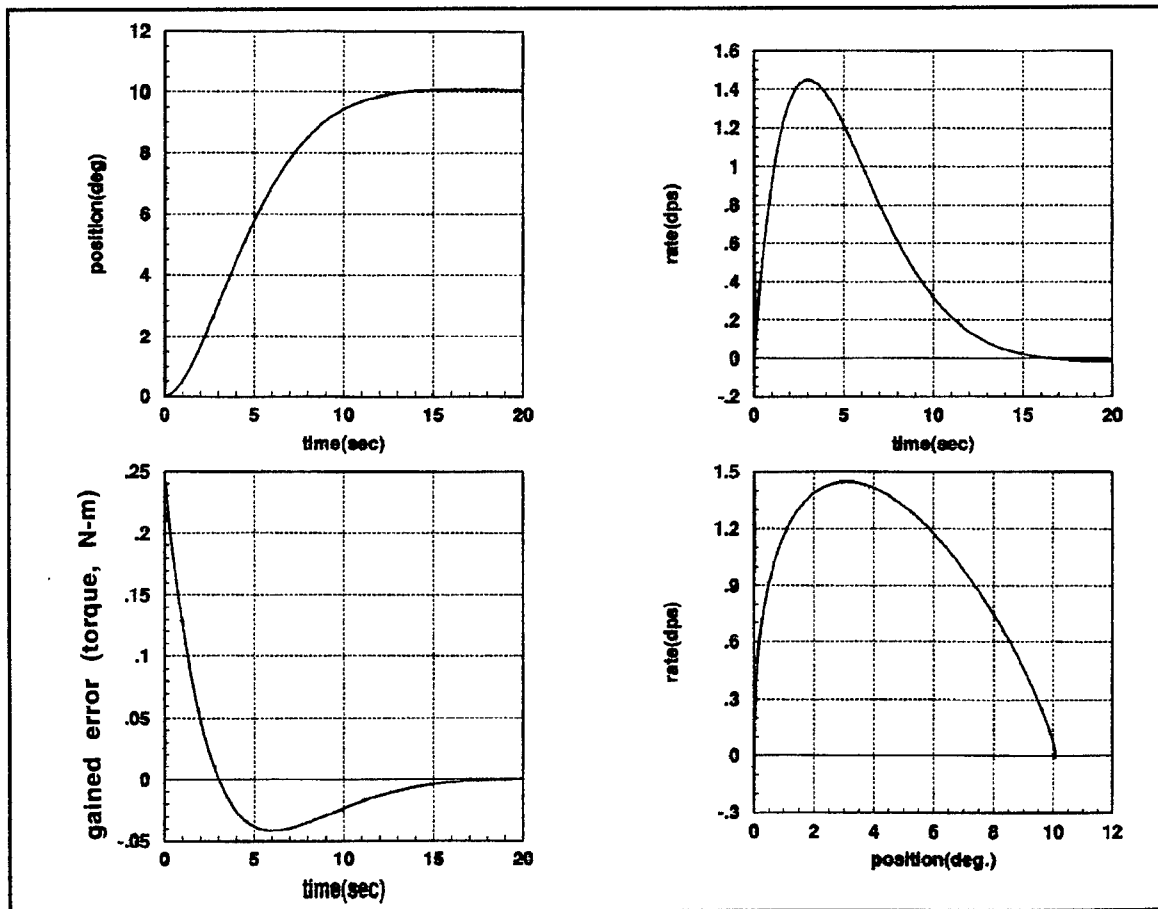

Figure 10. Step Response for Linear Actuation with Position and Rate Feedback

A. THRUSTER CONTROL STEP RESPONSE (SLEW MANEUVER)

For large values of the error signal the system response with thrust-modulation is similar to the simple bang-bang system because the PWPF modulator tends to operate above its linear range. This is demonstrated by comparing **Figures 11** and **12** below, where a 10° slew maneuver has been commanded from rest for bang-bang and modulated thruster control. Both controllers complete the maneuver in about 24 seconds, slower than the linear case but with essentially no overshoot as was desired.
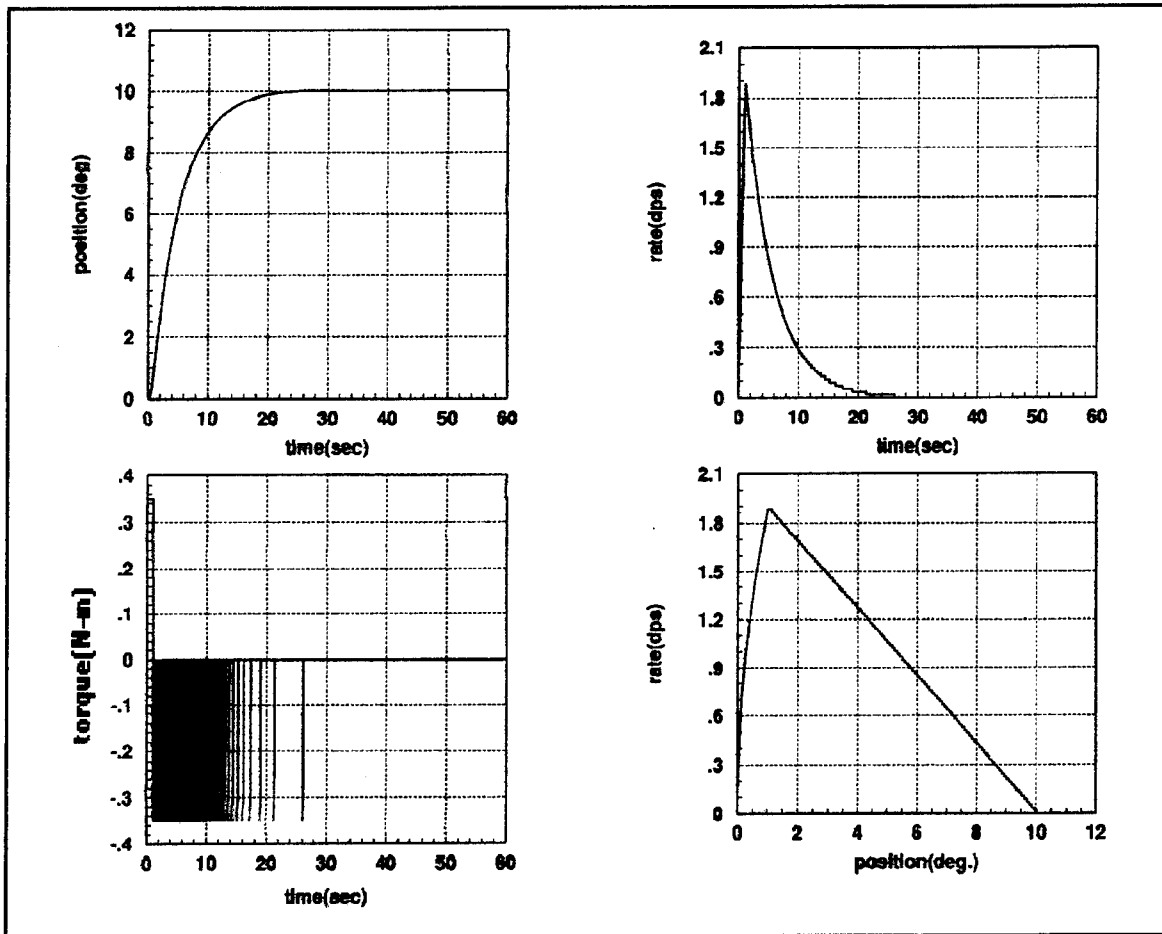

Figure 11. Slew Maneuver with Bang-Bang Controller

The control torque pulses change in frequency for both controllers. This can be understood by referring back to Figure 4, which depicted the "ladder-step" phase plane approach to the final commanded state. The coast period (horizontal line in phase plane)

18

between each pulse increases as the trajectory approaches $\dot{\theta} = 0$, hence the pulse frequency decreases. The trajectory rides the boundary of the deadband from just after one second until the completion of the maneuver.
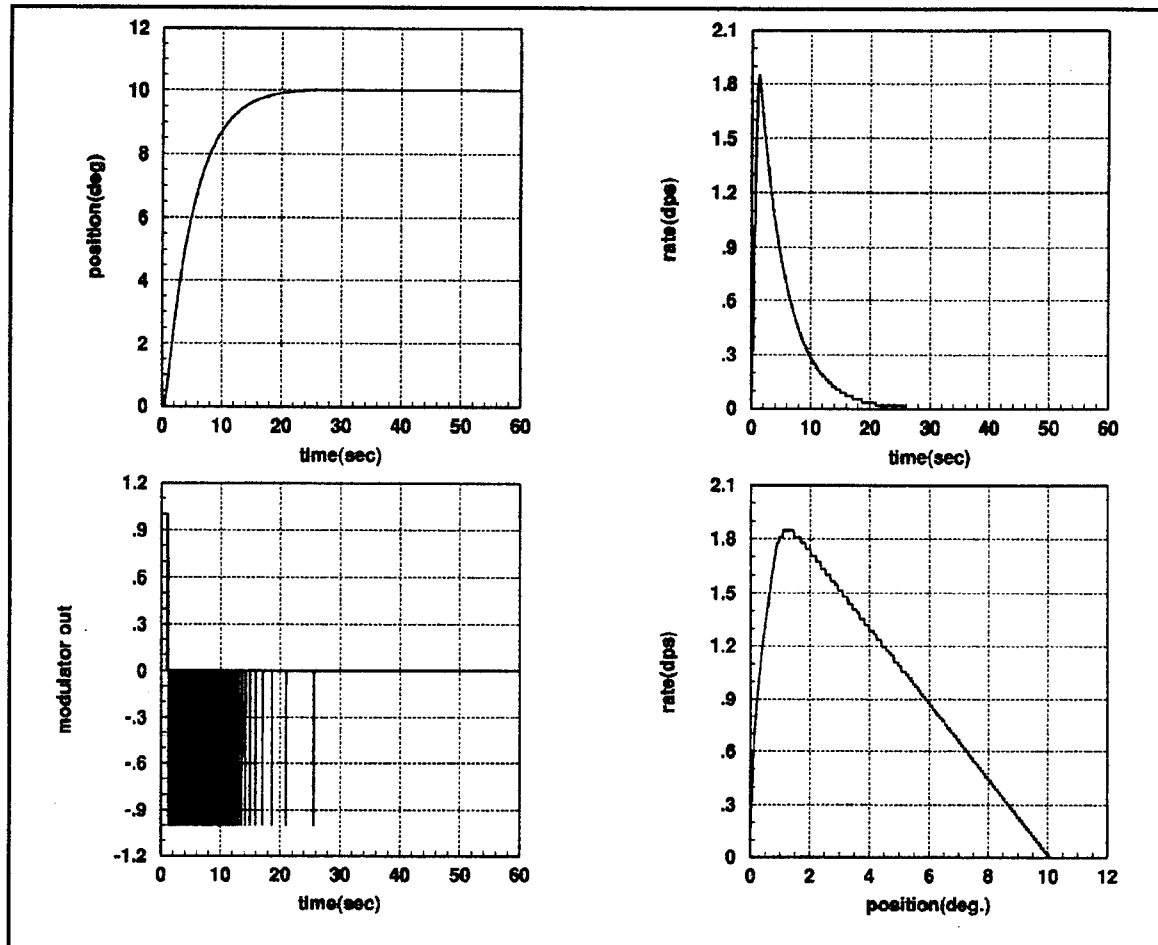

Figure 12. Slew Maneuver with Thrust-Modulated Controller, K=39

Note that the modulated maneuver is slightly smoother in the phase plane. The response is closer to the characteristically smooth phase trajectory of the linear system (Figure 10) because the PWPF modulator is closer to approximating linear actuation. The smoothness of the trajectory is an important factor in the presence of flexibility. An abrupt change in velocity curve from positive slope to negative slope indicates an abrupt change in acceleration and hence jerk as well. The faster the acceleration is reversed, the more jerk is applied, which for a flexible structure results in more stored flexural energy. Whereas the

19

bang-bang controller only operates according to the sign of the error signal, the PWPF modulator responds to both the magnitude and the sign of the error. The difference in phase trajectory smoothness is shown more dramatically in simulations where the feedback gains and k_j are all set to unity (**Figures 13-15**). The resulting damping ratio of .15 (for the linear controller) produces excessive overshoot but also a faster rise time. Both of these effects are seen to some extent with the nonlinear controllers, however the modulated system provides a smoother transition between the reversal of acceleration.
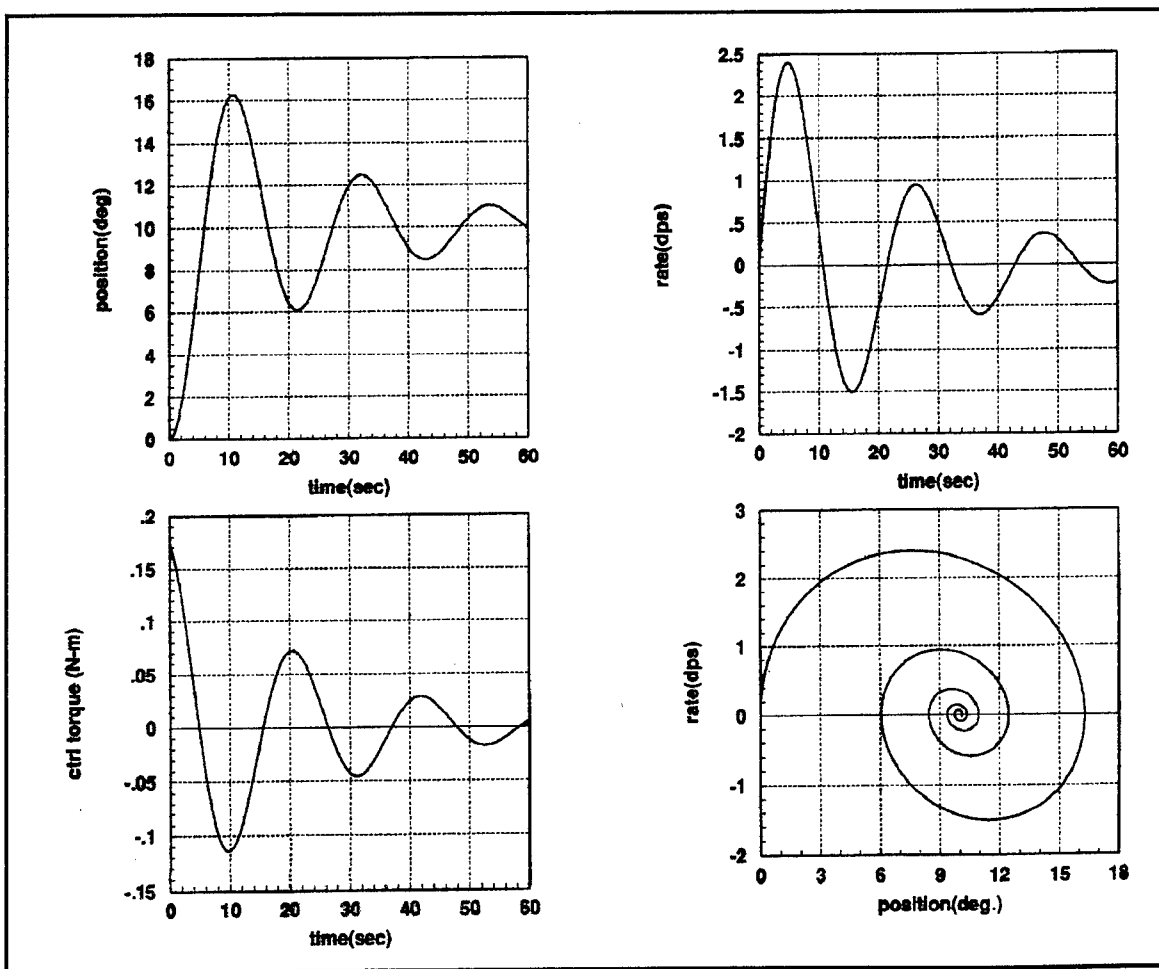

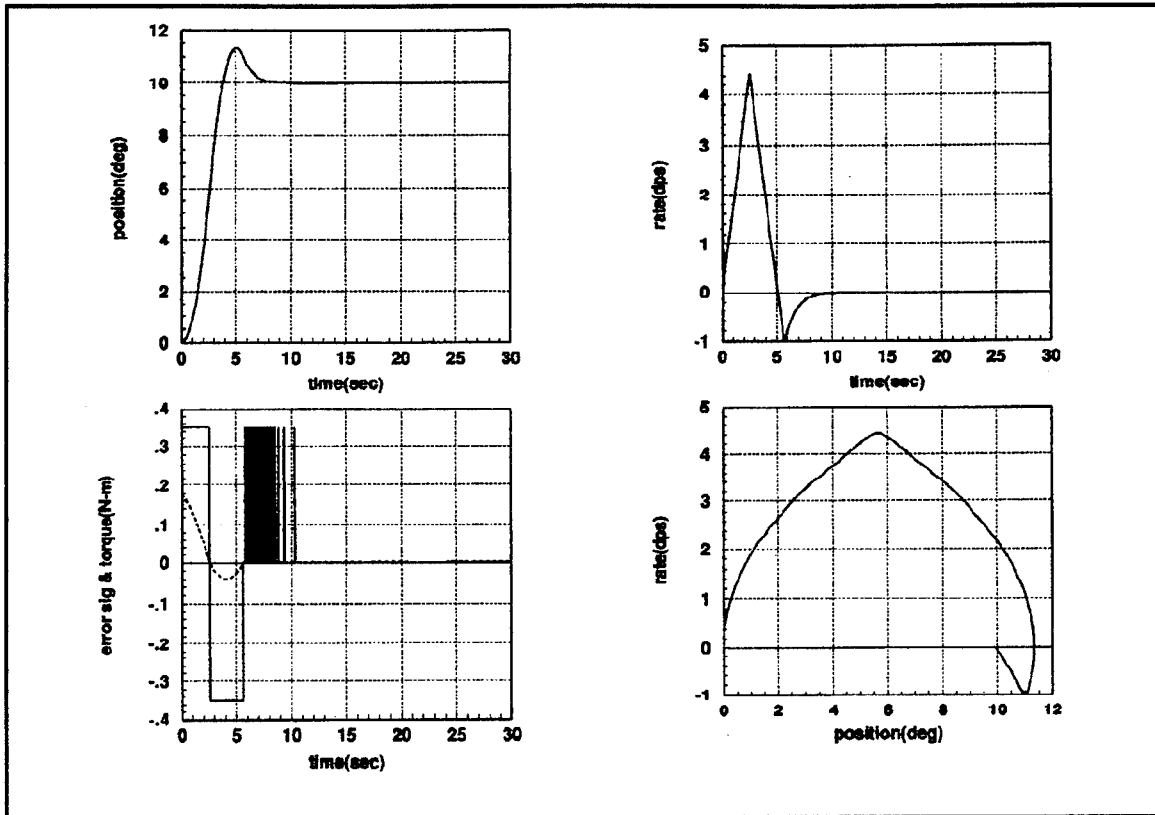**Figure 13. Underdamped Slew Maneuver with Linear Controller**

20

Figure 14. Underdamped Slew Maneuver with Simple Bang-Bang Control
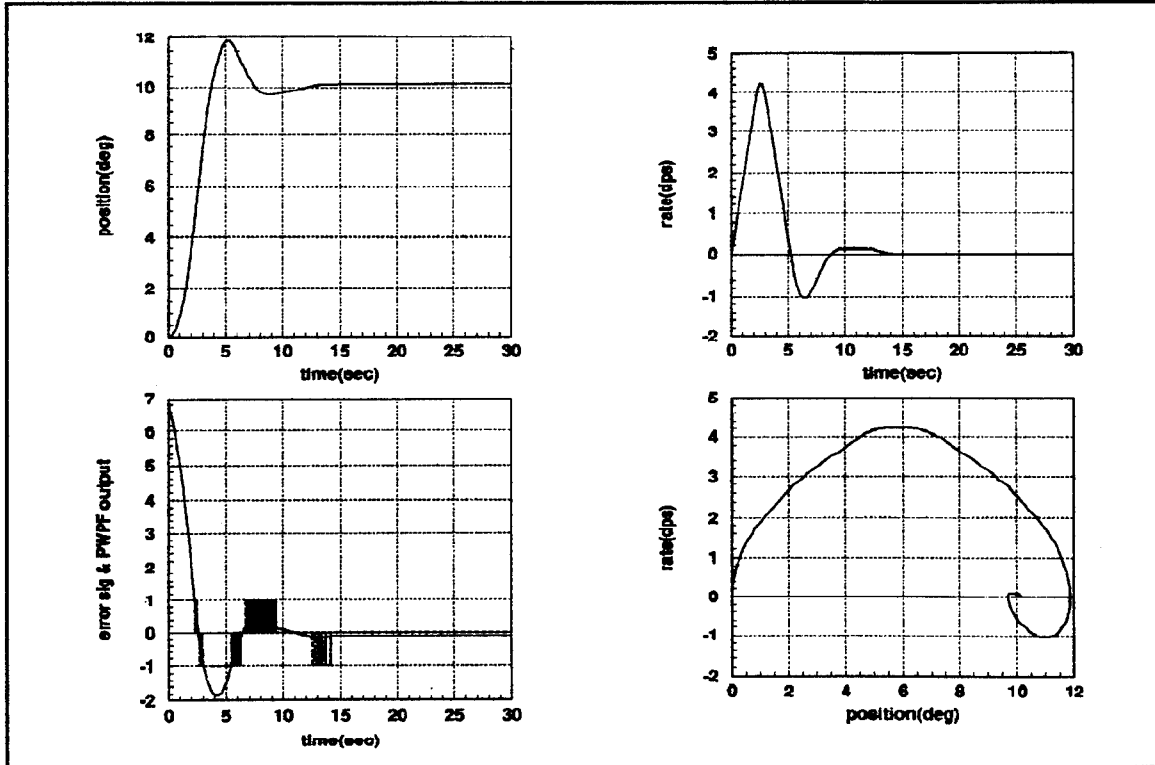

Figure 15. Underdamped Slew Maneuver with PWPF Modulator, K=30

21

Note from **Figure 15** that the pulse-modulated response would closer match the linear simulation if the modulator were operating in its linear region over the maneuver. As the time history of gained error signal shows, the modulator input is above the modulator saturation level of 1.05 (see Figure 8) until about 2.5 seconds, causing continuous-on operation.

For the linear control loop, application of the final value theorem indicates that the steady state error to a step input is zero. The PWPF modulator on the other hand contains an internal dead zone which results in a steady state error (or defines the amplitude of the rigid body limit cycle), such as can be seen in Figure 15. The small steady state error is achieved only by using a high value of modulator input gain K (=39 for the previous runs). The need for a substantial value of input gain can be understood by considering the magnitude of the signal prior to the modulator input gain. The initial error signal is due to the commanded input only, since the spacecraft is initially at rest:

$$e(0) \times k_1 = 10° \left(\frac{\pi}{180°} \right) \times 1.0 = .174$$

which is the maximum value of this signal over the entire maneuver, already quite small considering the modulator dead zone of approximately +/- *0.15*. Because the thruster is full-on for the first 2.5 seconds, the angular rate increases quickly to nullify the error signal:

$$e(\sim 2.5 \text{ sec}) \times k_1 = (10° \times 1 - 6° \times 1 - 4.2°/\text{sec} \times 1) \times \frac{\pi}{180°} = -.003$$

which is much too low to trigger the modulator. So a dramatic gain factor is needed to keep the modulator input signal above its internal deadband. It was found, however, that the value of modulator input gain could be substantially lower, say $K =10$, while still achieving the maneuver (**Figure 16**).
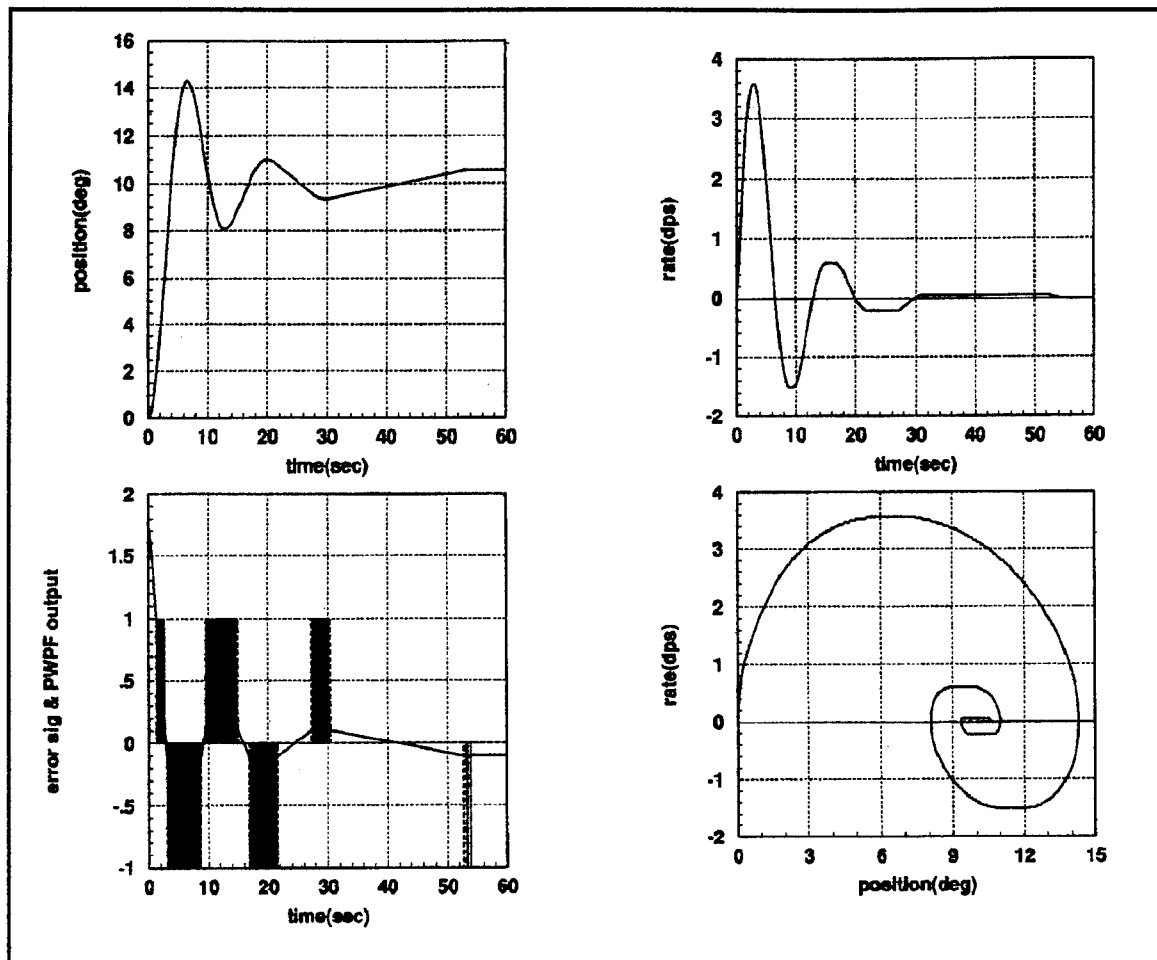
Figure 16. Underdamped Slew Maneuver with PWPF Modulator, K=10

The rise time is not affected appreciably by the lower input gain, since the modulator is still initially saturated, producing a period of constant thrust. The lower value of K however results in more steady state error because the deadband is reached sooner. As with a linear system, an increase in the loop gain (via the modulator input gain) decreases the steady state error in the presence of a disturbance torque; this is discussed further in Chapter IV.

Note that limit cycle behavior was not seen after maneuver completion in the previous simulations. This is because the final thruster pulse brings the velocity to zero. With non-zero initial conditions the limit cycle is seen at the completion of the maneuver (**Figure 17**).
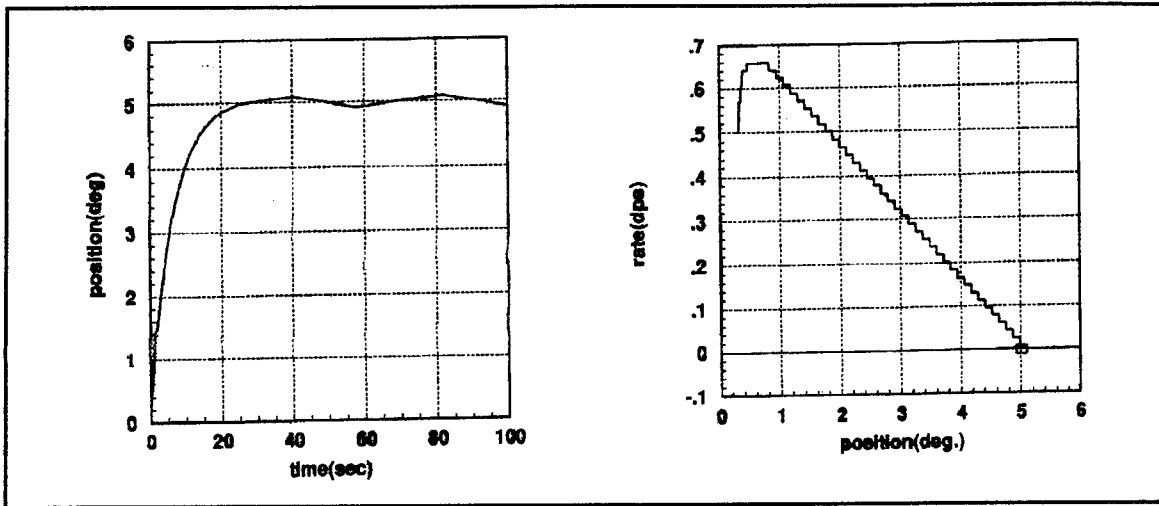
23

Figure 17. Thrust-Modulated Slew Maneuver with Non-Zero Initial Conditions

A ten degree slew maneuver performed using the time-optimal bang-bang controller is shown in **Figure 18**. Although the maneuver is faster than the other types of thruster control, the acceleration is by definition of the control law reversed instantaneously at the half-maneuver time. The effects of this with a flexible structure can be seen in the results presented in Reference 4, which show the maximum strain in the structure occurring just after the half-maneuver point. The stored energy then produces a whip-like motion of the flexible appendage which contributes to overshoot at the end of the maneuver. In rigid body simulations without dead zone, the sampling interval alone constituted enough of a delay to cause switching instability at the end of the maneuver. Hence it was necessary to include dead bands on position error, $(\theta_{cmd} - \theta_{out})$, and rate $\dot{\theta}_{out}$, in order to avoid thruster chatter at the sampling rate of 100 Hz. Even with the dead zone, Figure 18 shows a slight imperfection in the half-time switching. Note that the maximum velocity reached (approximately 4.5 deg/sec) is over twice the velocity achieved using the other controllers. In many systems rate limiting is necessary, which of course diminishes the intended advantage of time-optimal switching.
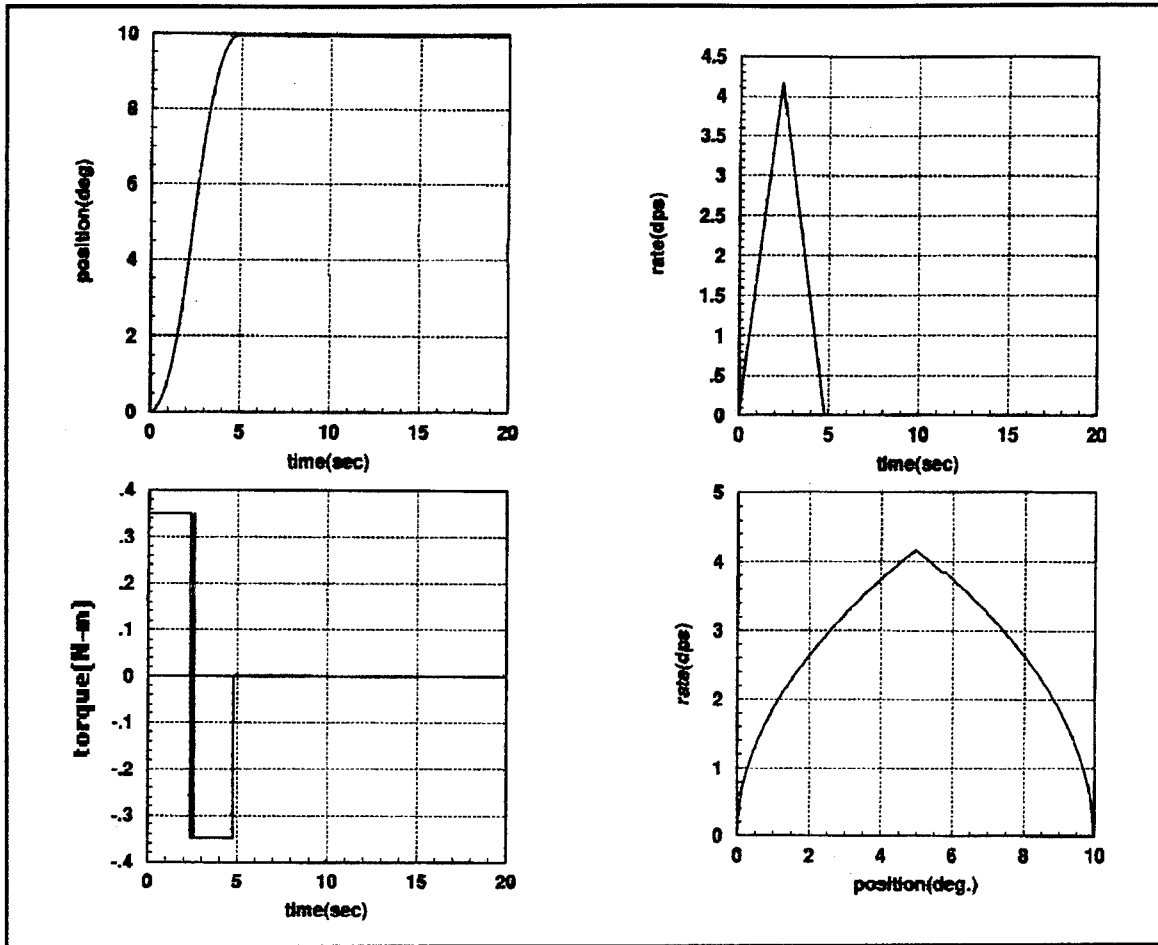
24

Figure 18. Time-Optimal Bang-Bang Maneuver

Sensitivity of the time-optimal control system to parameter uncertainty was studied. Note that the switching law (Equation (2)) contains the thrust value and the total moment of inertia. Since these parameters are generally not known exactly, the values used in the switching law are only a best estimate. Though a thruster may be accurately calibrated, the actual torque produced is subject to mounting misalignment tolerances and plume impingement effects. Also, the moment of inertia of the satellite changes over the orbit lifetime with the depletion of propellant. Uncertainty manifests as overshoot (or undershoot) and subsequent unintended thruster firing (see **Figures 19** and **20**). Note the rigid body limit cycle which is established after completion of the maneuver.
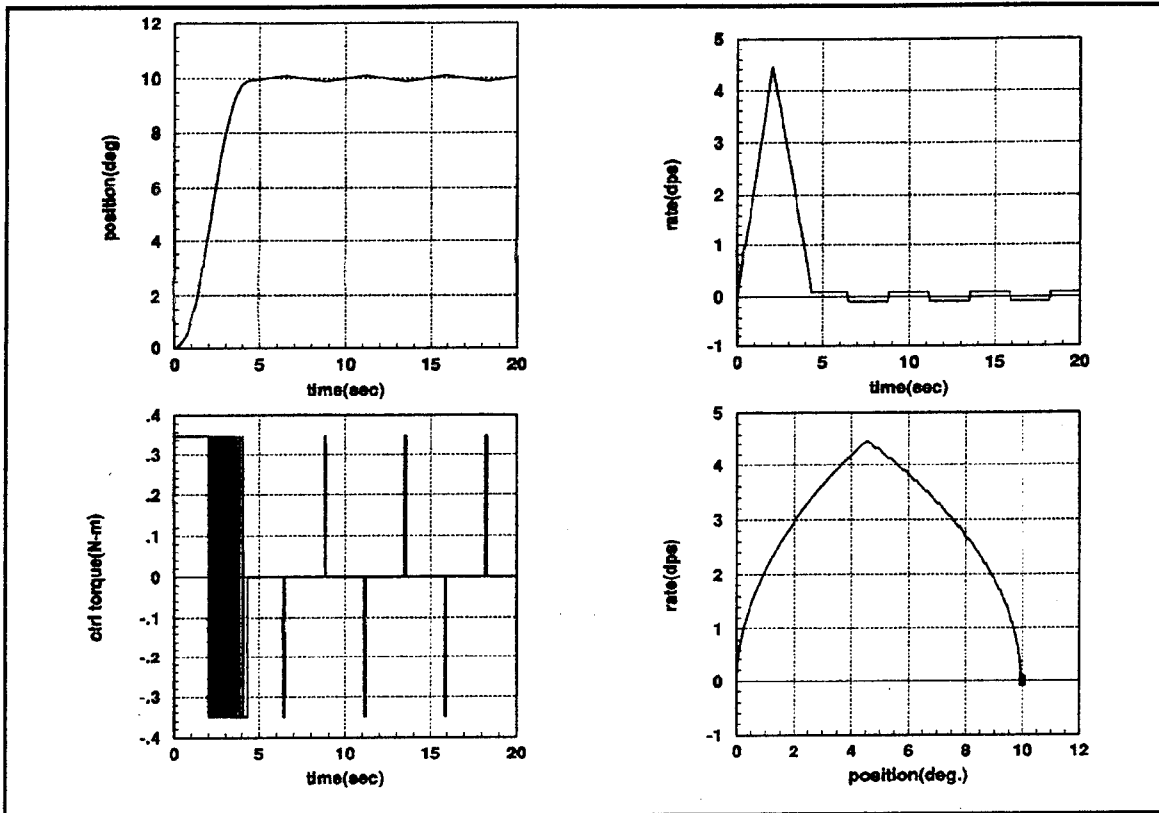
25

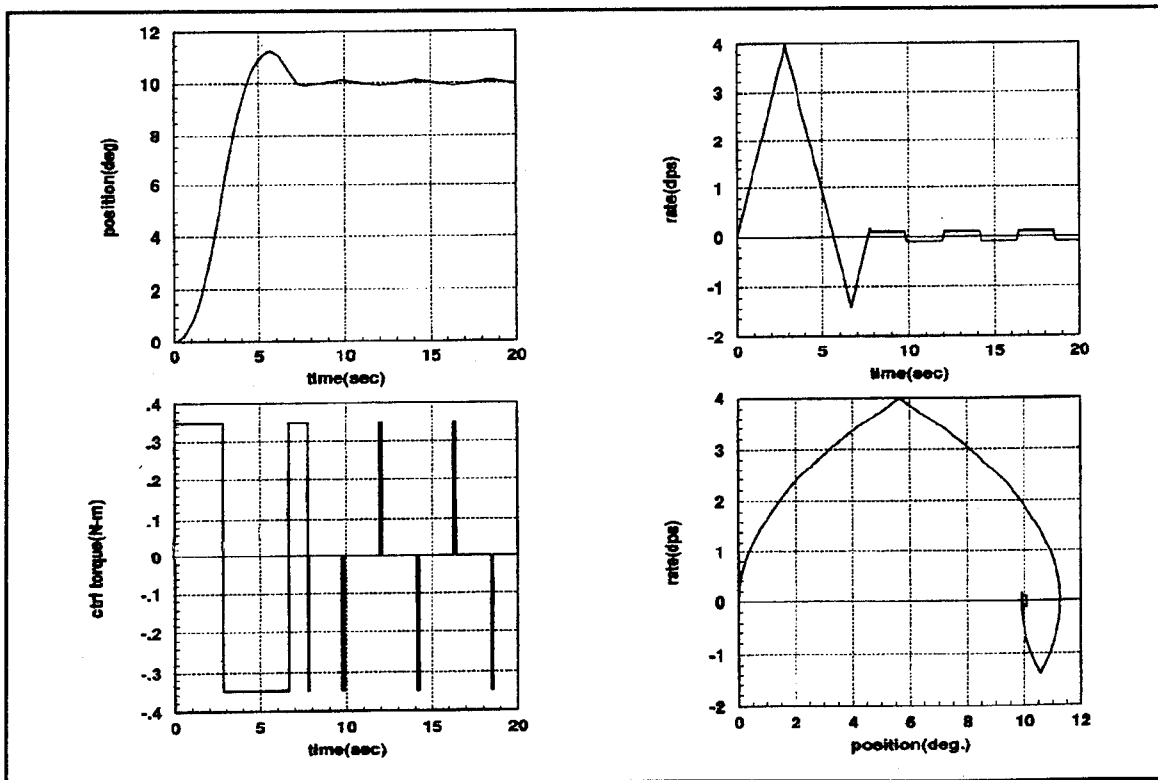**Figure 19. Time-Optimal Bang-Bang, 20% Overestimate of Moment of Inertia**

Figure 20. Time-Optimal Bang-Bang, 20% Underestimate of Moment of Inertia

26

With the PWPF-modulator uncertainty does not play as critical a role since an estimate of the inertia and the control torque are not part of the control law formulation.

B. NOMINAL CONTROL MODE: RIGID BODY LIMIT CYCLE PERFORMANCE

The rigid body limit cycle performance was determined for each controller by simulating the response to small initial conditions. Limit cycles of the same size in the phase plane correspond to equivalent limit cycle frequencies. With the goal of keeping within +/- 0.1° pointing accuracy, the deadband of the bang-bang controller and the input gain for the modulated controller were adjusted accordingly. In the case of the simple on-off controller with deadband, the limit cycle behavior is shown in **Figure 21**. From the position graph the limit cycle frequency is determined to be about .026 Hz.
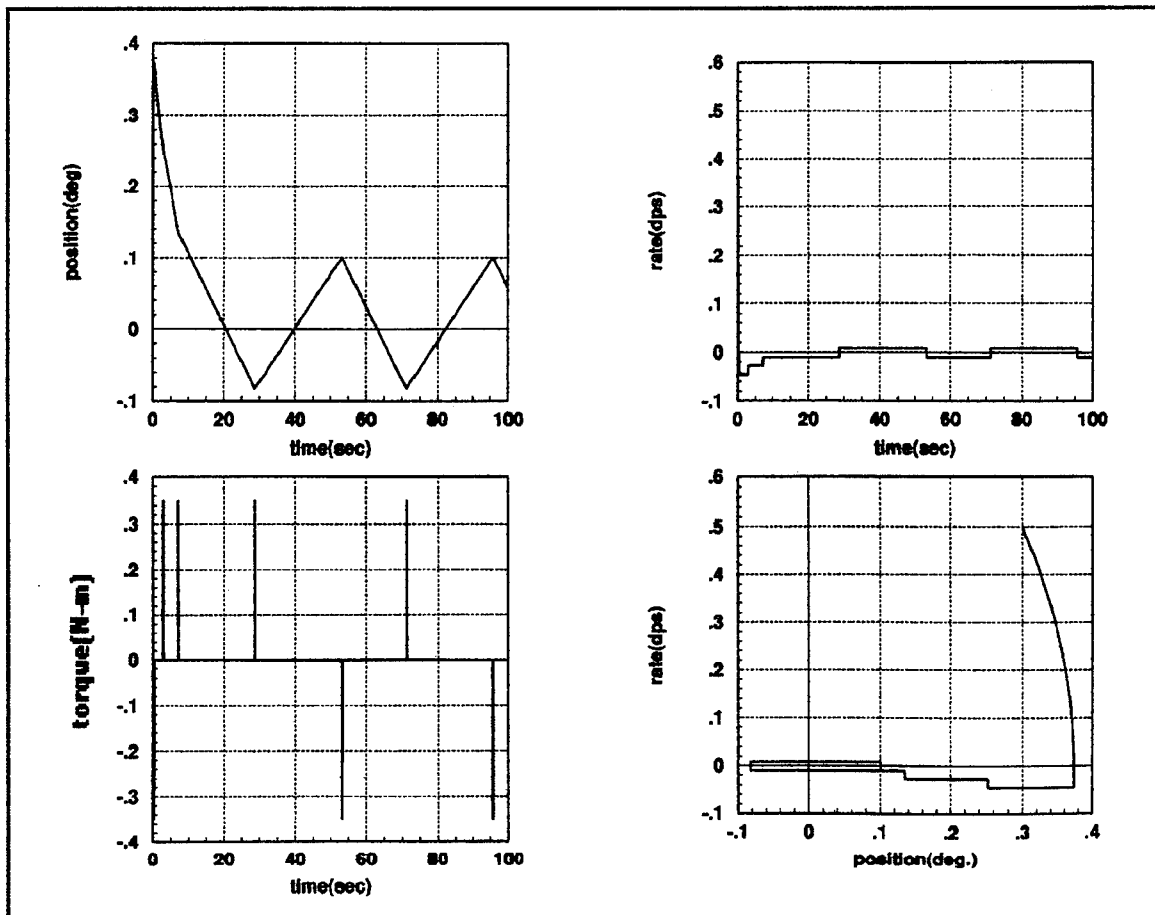

Figure 21. Rigid-Body Limit Cycle with Bang-Bang Controller

27

A limit cycle of similar frequency is achieved with the PWPF modulator (**Figure 22**) with an input gain K of 39. Treatment of the rigid body limit cycle in more general mathematical terms for any thruster system can be found in Reference 5, which also notes that with position and rate feedback, the limit cycle is stable.
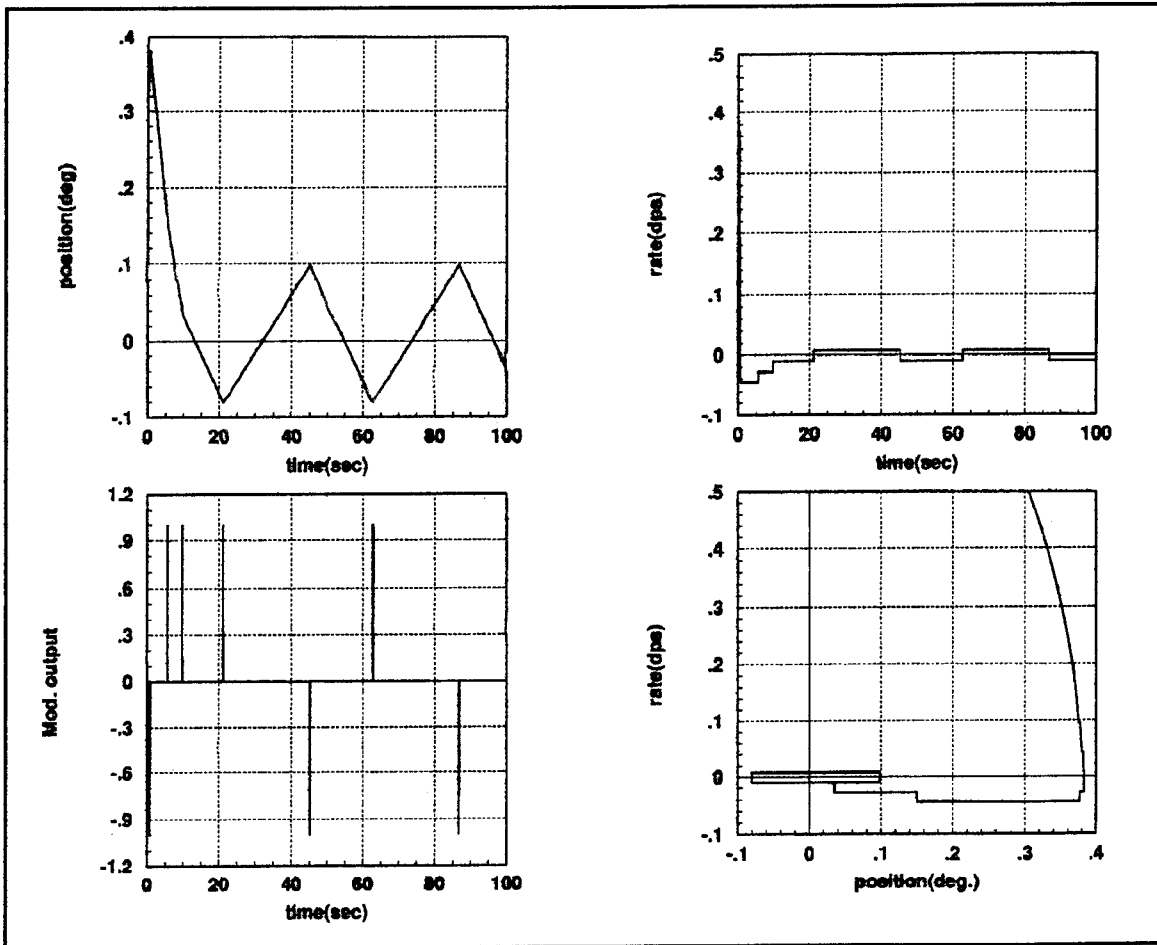
Figure 22. Rigid-Body Limit Cycle with Thrust-Modulated Controller

The same limit cycle is established for both controllers because minimum-impulse operation is established, i.e. each vertical portion of the limit cycle corresponds to the minimum .01 second thruster pulse (with $\Delta\dot{\theta}_{min}= .02$ deg/sec). This is unexpected since early literature indicates a conventional bang-bang controller would not converge to

28

minimum impulse operation, but would rather form the higher frequency limit cycle shown in **Figure 23** [adapted from Reference 6].
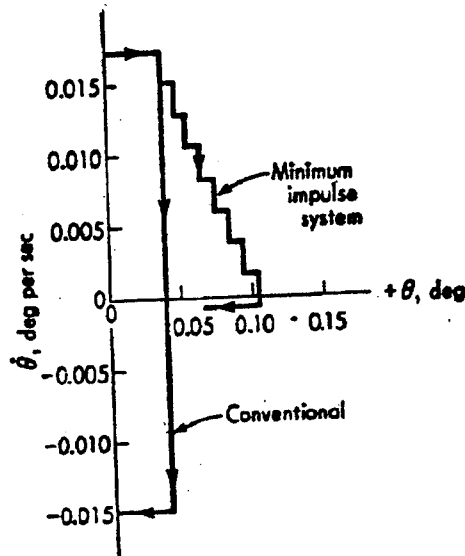
Figure 23. Expected Limit Cycles for Conventional (Bang-Bang) and Minimum Impulse (PWPF) Systems

Though time-optimal switching would probably not be used for nominal attitude control, a limit cycle of comparable size can be produced by introducing plant inertia uncertainty (here -20% was used as in Figure 20). **Figure 24** shows that minimum-impulse operation is not established and the resulting frequency is determined to be about .18 Hz, substantially higher than the other controllers.
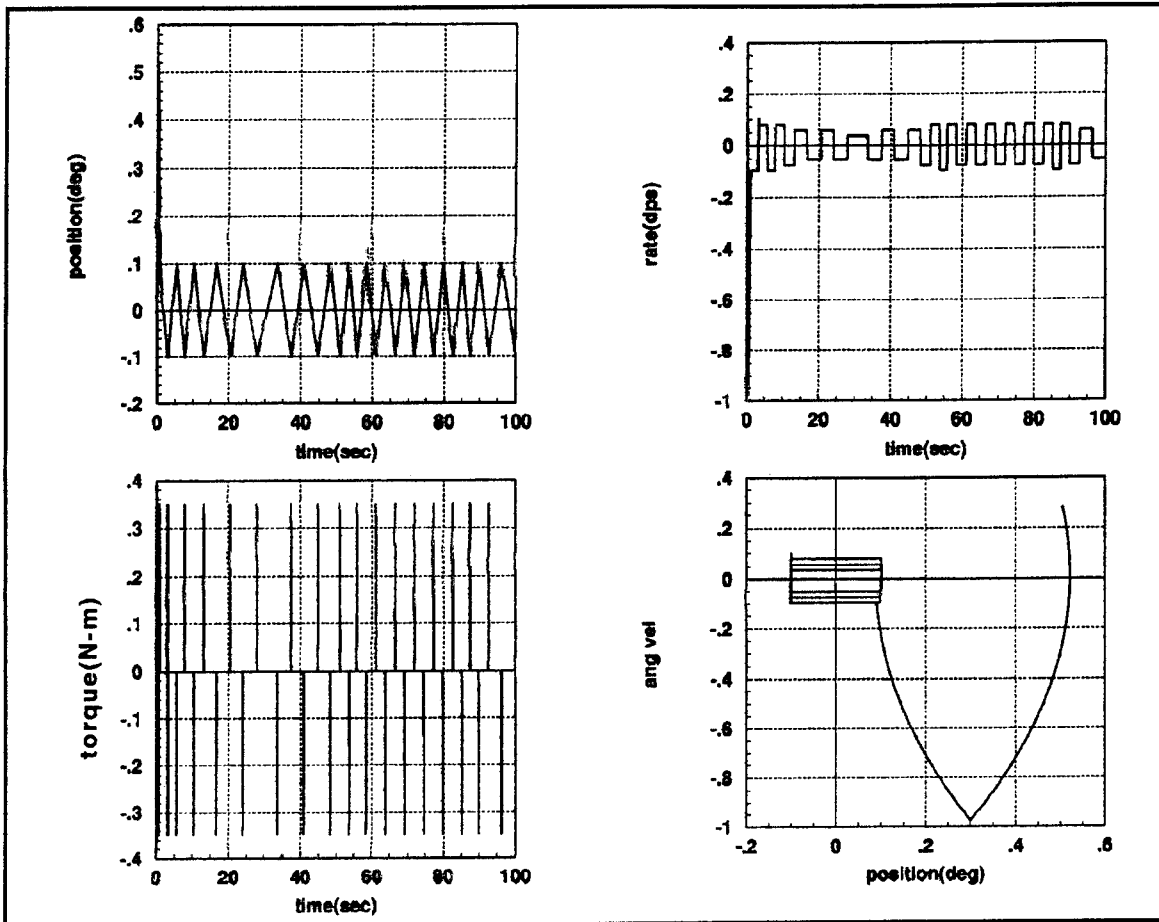
Figure 24. Rigid-Body Limit Cycle with Time-Optimal Switching

C. DISTURBANCE REJECTION

The response of the various control systems to a constant disturbance torque was studied. A constant torque of .015 N-m was applied in most cases. This value was originally used in Reference 7 to model the torque applied due to cabling wind-up in the experimental FSS setup. The value scales nicely to the thruster misalignment disturbance torque countered by the controller in Reference 1. The assumption of a constant disturbance torque is adequate for the case of disturbance due to thruster misalignment during a translational maneuver. The response to stochastic disturbances such as sensor noise are not considered.

A typical phase portrait for the thruster systems [Ref. 5, Ref. 6] converges to a disturbed limit cycle of the shape shown in **Figure 25**. The time history of **Figure 26** shows that as the deadband is reached due to the disturbance, a thrust pulse is commanded to counter the disturbance. The plot of θ shows that the satellite periodically "bounces" off the deadband. These plots were generated using a more powerful thruster and are therefore intended for illustrative purposes only.
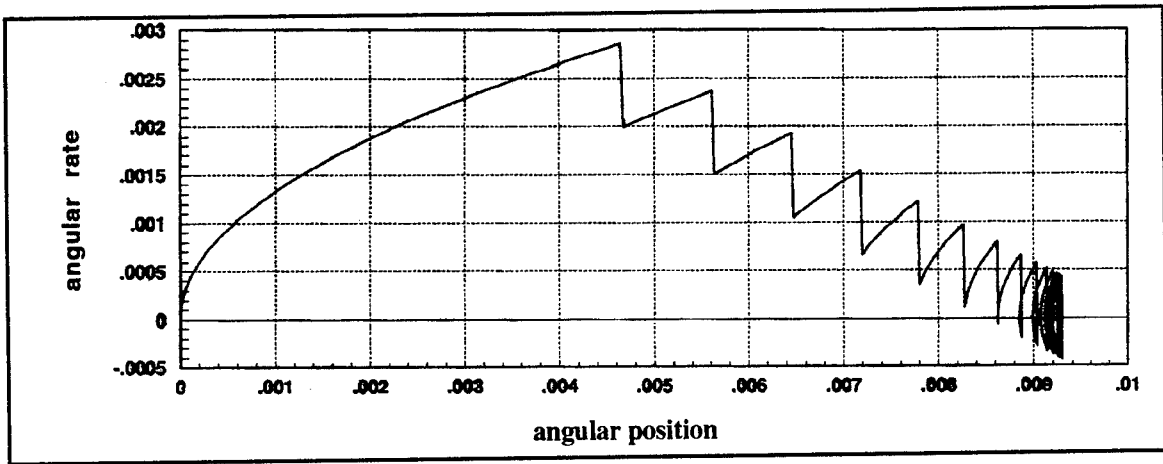

Figure 25. Phase Plane Trajectory with Convergence to Disturbed Limit Cycle
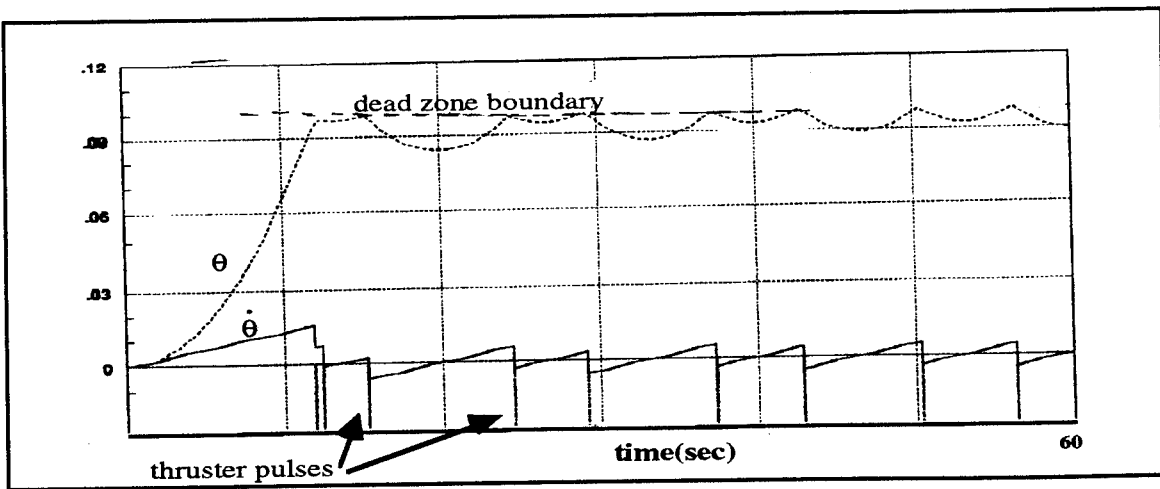
Figure 26. Typical Response to Constant Disturbance Torque

Using the system parameters considered thus far, the angular position responses for the bang-bang and the PWPF-modulated systems (with K=39) are shown in **Figures 27**

31

and **28.** Both results show thruster activity at 4.2 Hz, where the disturbance torque keeps the satellite at the edge of the deadband.

Figure 27. Response of Bang-Bang Control System to Constant Disturbance Torque

Figure 28. Response of Pulse-Modulated Control System to Constant Disturbance Torque

Note that the modulated controller does not provide the required pointing accuracy of .1 degrees. With a linear controller the steady state error under the influence of a constant disturbance torque is inversely proportional to the controller gain. With the PWPF

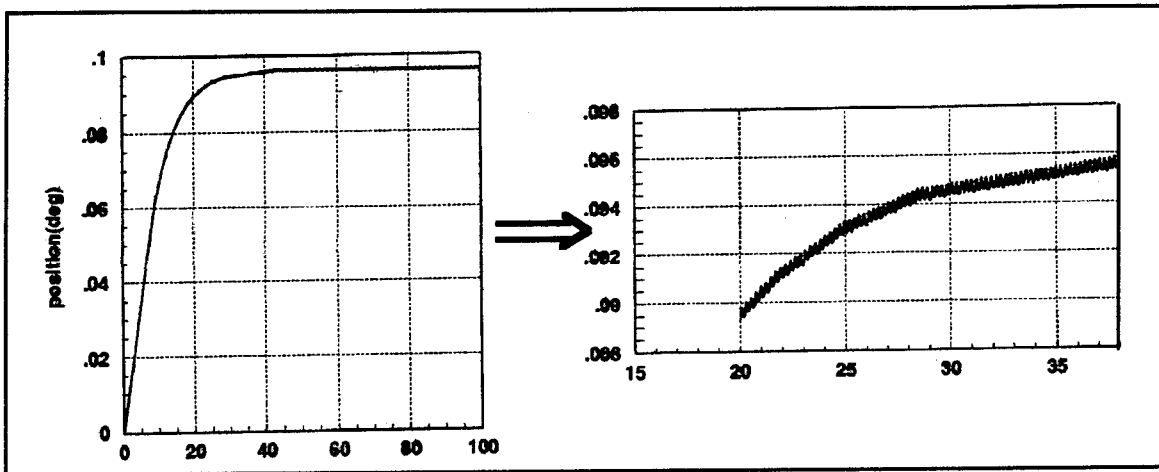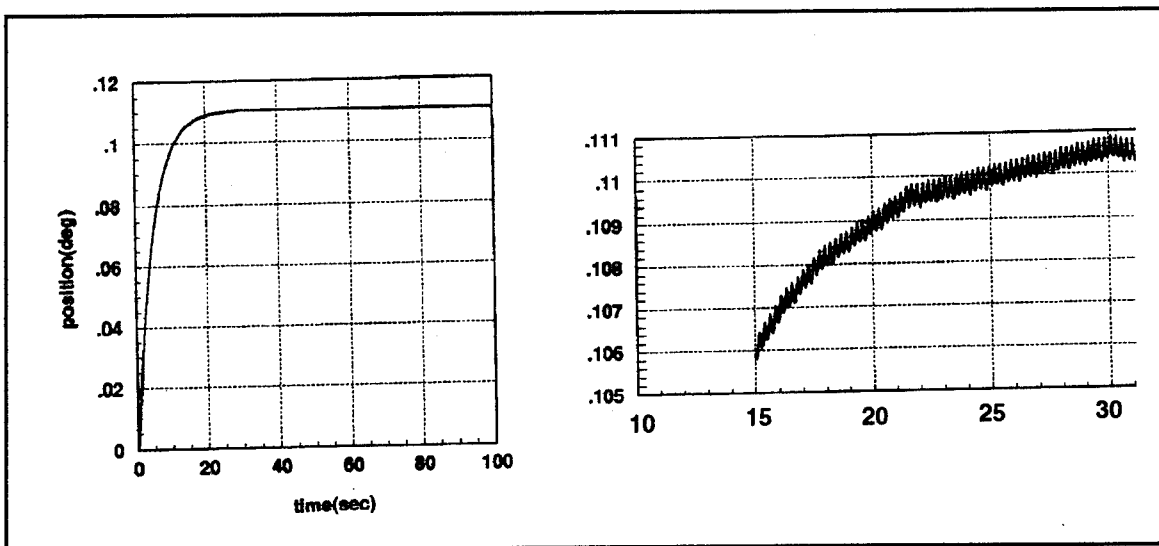modulator the gain on the error signal can similarly be increased in order to lower the steady state error. This is demonstrated in flexible body simulations in Chapter IV. The flexible body stability problems which can be encountered due to the thruster activity and the increased gain are further discussed in Chapters IV and V.

A closer look at the gained error signal and the resulting pulses (**Figure 29**) for the PWPF-modulated simulation shows that when the error signal reaches the internal deadband of the modulator (point A) a single pulse is fired which decreases the error signal until the end of the pulse (point B). The error signal then grows under the influence of the disturbance until the deadband is reached again, triggering another thruster firing (point C). The pulse width of ten milliseconds is consistent with the response to the input of -.15 as given in Table 1, however the 8 Hz pulse rate cannot be realized since the input signal is not constant, but rather drops with each pulse.
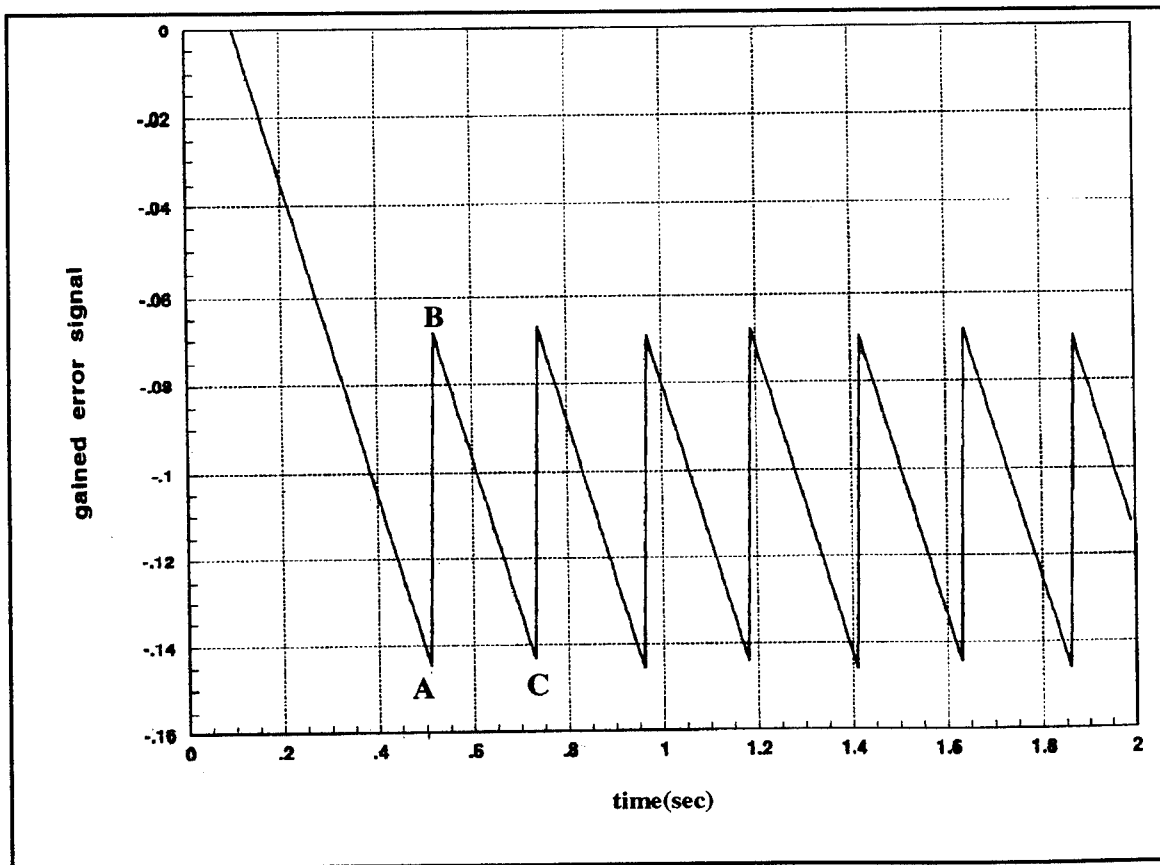
Figure 29. Error Signal During Constant Disturbance Torque

33

IV. FLEXIBLE SPACECRAFT DYNAMICS AND SIMULATIONS

The simulations in Chapter III demonstrated the advantages of PWPF modulation for the rigid body case. The flexible body dynamics are now discussed and comparative simulations presented.

A. FLEXIBLE SPACECRAFT MODELS

It is often necessary to include several vibrational modes of a flexible structure in a spacecraft dynamical model in order to adequately design the control system and to foresee possible modes of interaction between the control system and the structure. It is instructional to first examine the model of a spacecraft with one dominant mode of vibration about the controlled axis. Consider the spacecraft with a flexible solar array pictured in **Figure 30** [adapted from Reference 8].

Figure 30: Spacecraft With Flexibility

Assuming a single undamped dominant torsional mode of vibration, the transfer function from control input to angular position output can be represented as:

$$G(s) = \frac{\theta_b(s)}{T(s)} = \frac{s^2 + \omega_n^2}{s^2 I_b (s^2 + \Omega_n^2)} \qquad (13)$$

with

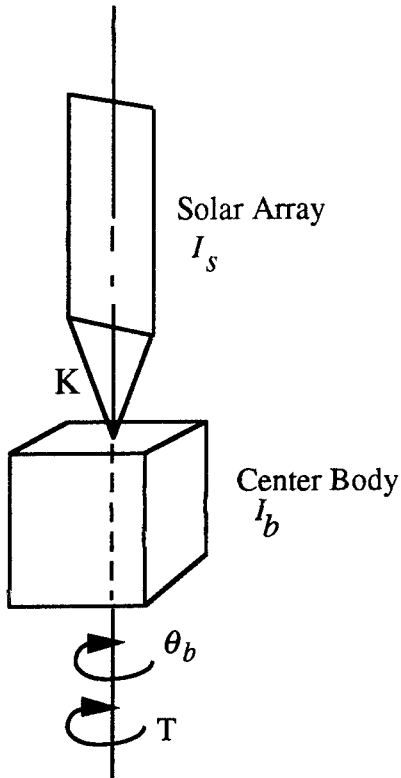$$\omega_n = \sqrt{\frac{K}{I_s}} \qquad \text{and} \qquad \Omega_n = \omega_n \sqrt{1 + \frac{I_s}{I_b}} \qquad (14)$$

where s is the Laplace transform variable, I_b and I_s are respectively the rigid body and solar array inertias about the pictured axis, θ_b is the controlled rotation angle of the rigid central body, T is the control torque, and K is the torsional stiffness. The term ω_n in the numerator is the cantilever frequency (fixed base frequency) of the flexible appendage, and Ω_n in the denominator is the "system mode" or "free-free" mode frequency of vibration, whereby the rigid hub is no longer fixed but vibrates together with the flexible appendage. The s^2 term in the denominator is attributable to the rigid body mode of the spacecraft (zero frequency). An important observation to be made is that the complex zeros of the plant transfer function correspond to the fixed-base vibrational frequency of the flexible structure. So the transfer function implies that while the flexible appendage may be vibrating at its natural frequency, a control torque is supplied to keep the central body from rotating [Ref. 9]. For the more general case of N modes of vibration, the transfer function representation of the dynamics can be represented as

$$G(s) = \frac{\Theta(s)}{T(s)} = \frac{1}{I s^2} \prod_{i=1}^{N} \frac{[s^2 / \omega_i^2 + (2\zeta_i / \omega_i)s + 1]}{[s^2 / \Omega_i^2 + (2\zeta_i / \Omega_i)s + 1]} \qquad (15)$$

where I is the entire spacecraft inertia, ω_i is the ith cantilever mode natural frequency, and Ω_i is the ith system mode natural frequency.

35

The dynamics of Equation (13) can be derived easily because of the simplification that a single vibrational mode and a known stiffness K could represent the solar array flexibility. A higher fidelity dynamical model of a flexible spacecraft can be developed via the hybrid-coordinate representation of the system [Ref. 10], which includes both physical coordinates and modal coordinates. A finite element analysis is performed to determine the cantilever frequencies and mode shapes of the structure. For the general case of three rotational degrees of freedom, the linearized equations of motion are [Ref. 1], for the rigid body:

$$\underline{I}\ddot{\underline{\theta}} + \underline{\underline{H}}\dot{\underline{\theta}} + \underline{D}^T \ddot{\underline{q}} = \underline{T}_c + \underline{T}_d \qquad (16)$$

and for the flexible appendage:

$$\ddot{\underline{q}} + 2\zeta\underline{\omega}\dot{\underline{q}} + \underline{\omega}^2\underline{q} + \underline{D}\ddot{\underline{\theta}} = \underline{0} \qquad (17)$$

where I is the entire spacecraft inertia matrix, H is the momentum coupling matrix, D is the rigid-elastic coupling matrix of the flexible appendage, θ is the attitude angle vector, T_c and T_d are the control and disturbance torque vectors, q is the cantilever modal coordinate vector, and ω^2 is a diagonal matrix of squared cantilever modal frequencies. The inclusion of the damping term of Equation (17) is based on the assumption of modal damping, whereby the damping matrix has been uncoupled and a single value for the modal damping ratio, ζ, is assumed for all modes.

The flexible dynamics model used in this study was derived [Ref. 7, Ref. 11] for the experimental flexible spacecraft system (FSS) using the hybrid-coordinate formulation. The system, pictured in **Figure 31**, free-floats on air pads and vibrates in planar motion, with translational motion restricted by the air bearing. Hence the momentum coupling term H (Equation 16) does not apply and I, θ, Tc and T_d become scalars. Equations (16) and (17) then become [Ref. 7]:

36

$$I_{zz}\ddot{\theta} + \sum_{i=1}^{n} D_i \ddot{q}_i = T_c + T_d$$

(15)

$$\ddot{q}_i + 2\zeta_i \omega_i \dot{q}_i + \omega_i^2 q_i + D_i \ddot{\theta} = 0$$

with the rigid-elastic coupling matrix having reduced to a vector with each element based on the modal vector components in the rigid body frame (ϕ_i^x and ϕ_i^y) and defined for each mode i of the flexible appendage as:

$$D_i = \int_F (x_F \phi_i^y - y_F \phi_i^x) dm$$

(16)

Each D_i is calculated using a FORTRAN subroutine which operates on the cantilever modal frequencies and mode shapes from the finite element analysis output; the integral of Equation (16) becomes a summation over the number of discrete subbodies into which the flexible body has been divided, where x_F and y_F locate each subbody in the rigid center body frame.
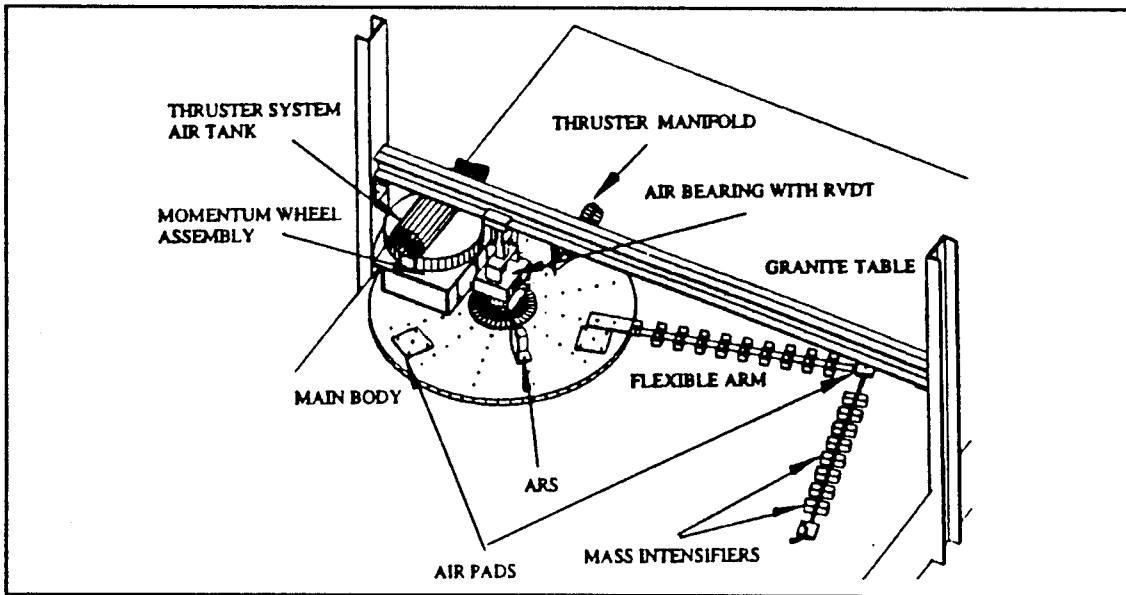

Figure 31. Flexible Spacecraft Simulator

In discretizing the system via the finite element method, the number of modes was truncated at six to obtain a compromise between reasonable model accuracy and

37

computational feasibility. The model was placed into state space in preparation for digital simulation using the Matrix$_X$/Systembuild software package. The state space representation of the system equations is:

$$\dot{x} = Ax + Bu$$
$$y = Cx + Du \tag{20}$$

where the state vector, x, is defined as:

$$x = [\theta \quad q_1.....q_6 \quad \dot{\theta} \quad \dot{q}_1.....\dot{q}_6]^T \tag{21}$$

The output y is the vector of the current states, hence C is a 14x14 identity matrix and it is assumed that the feedback values of angular position and rate are measured exactly. The system matrix form used in Matrix$_X$/Systembuild is

$$S = \begin{bmatrix} A & B \\ \hline C & D \end{bmatrix} \tag{22}$$

The system matrix was discretized for simulations with dt= .01 second. The complete mathematical descriptions of the state matrix A and the input matrix B are given in Reference 11 (p. 20). The direct transmission matrix D is set to zero.

During initial simulations with the flexible dynamics, the natural frequencies of oscillation were found to vary somewhat from the values presented in Reference 7 (pages 21 and 110). In order to find the actual frequencies present in the discretized model, a bode plot of the system was obtained (**Figure 32**). The DBODE command in Matrix$_X$ was used and the normalized frequencies were divided by the sampling period to obtain rad/sec.

38
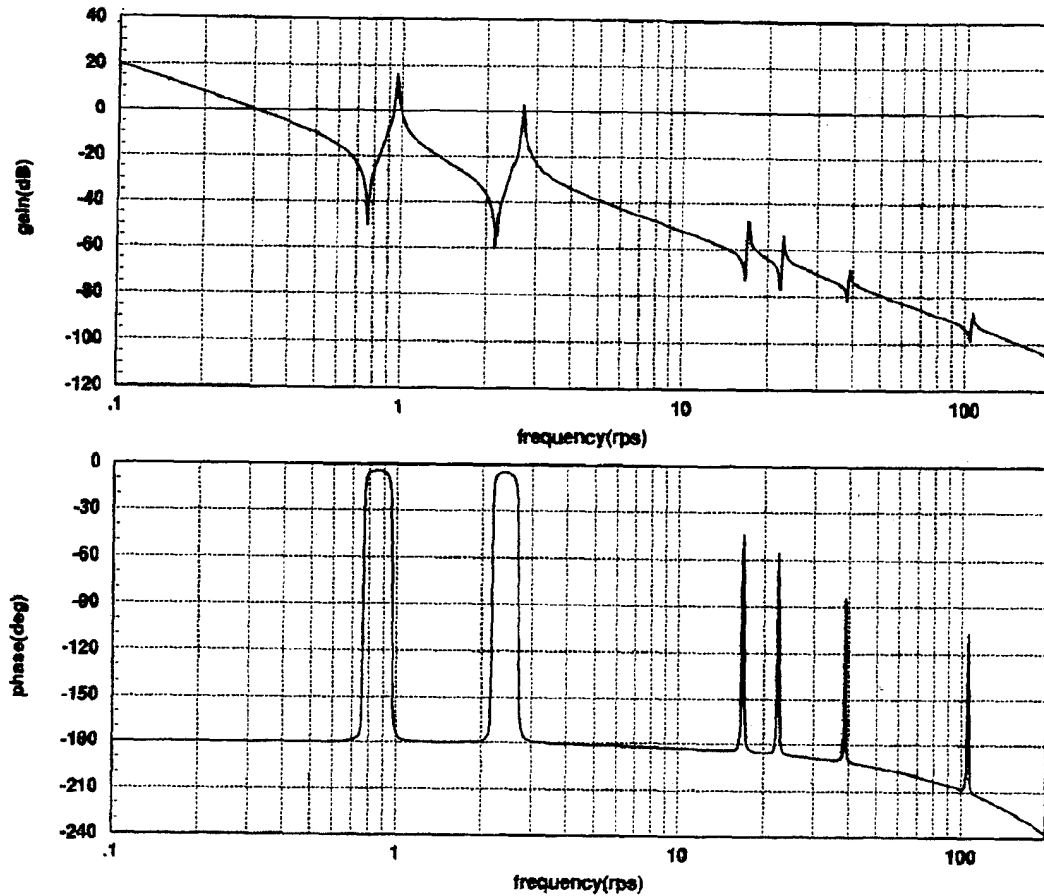
Figure 32. Bode Plot of Discretized Plant Model

Based on the bode plot the bode plot the cantilever and system frequencies were determined and are given in **Table 2**.

TABLE 2. FSS DISCRETE MODEL CANTILEVER AND SYSTEM FREQUENCIES

Mode	Cantilever Frequency (Hz)	(rad/sec)	System Frequency (Hz)	(rad/sec)
1	0.121	0.76	0.153	0.96
2	0.330	2.07	0.410	2.58
3	2.660	16.71	2.730	17.15
4	3.550	22.31	3.630	22.81
5	6.140	38.58	6.210	39.02
6	16.610	104.36	16.900	106.19

39

Reference 7 determined the first cantilever natural frequency to be .139 Hz, and the first system frequency .175 Hz. The discrepancy in the frequencies could partly be due to the method of discretization used. Consider the following continuous representation of a second order notch filter [Ref. 1]:

$$\frac{\dfrac{s^2}{w^2}+1}{\dfrac{s^2}{w^2}+\dfrac{.6}{w}s+1} \tag{23}$$

Figure 33 shows the continuous frequency response plotted with the discrete-time response using two different discretization methods (with $w= .96$). Note the shift in zero frequency introduced by the zero order hold method, whereas the first order hold method provides much better results. The same shift may have occurred when the FSS dynamics model was discretized. (This illustration underscores the difficulty in designing a notch filter for lightly damped poles since only a small inaccuracy in the knowledge of the true pole location would result in poor filter performance.)
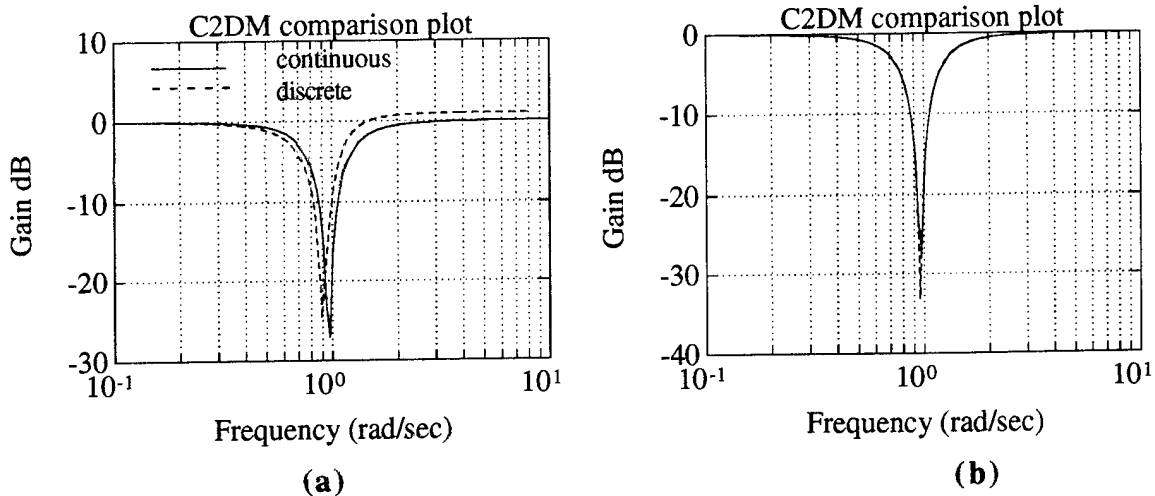

(a)   (b)

Figure 33.   Continuos to Discrete-Time Conversion of Notch Filter using (a) zero order hold method, (b) first order hold method.

40

The state space representation of the system contains the information to form transfer functions between the torque input and each of the fourteen outputs. The transfer function for the central body rotation angle output was given in Equation (15), and can be modified into the form

$$G(s) = \frac{\Theta(s)}{T(s)} = \frac{1}{Is^2} \prod_{i=1}^{N} \left(\frac{\Omega_i^2}{\omega_i^2} \right) \prod_{i=1}^{N} \frac{[s^2 + 2\zeta_i \omega_i s + \omega_i^2]}{[s^2 + 2\zeta_i \Omega_i s + \Omega_i^2]} \tag{24}$$

Using the values of the cantilever and system natural frequencies from **Table 2**, and an assumed modal damping ratio of .4 percent, the transfer function for the first three modes becomes:

$$G(s) = \frac{.23 * (s^2 + .006s + .58)(s^2 + .017s + 4.41)(s^2 + .134s + 279)}{(s^2 + .008s + .922)(s^2 + .021s + 6.76)(s^2 + 138s + 296)} \tag{25}$$

The poles and zeros of the complete six-mode transfer function were computed using a Matlab routine which is included in **Appendix C** and are shown in **Figure 34**.
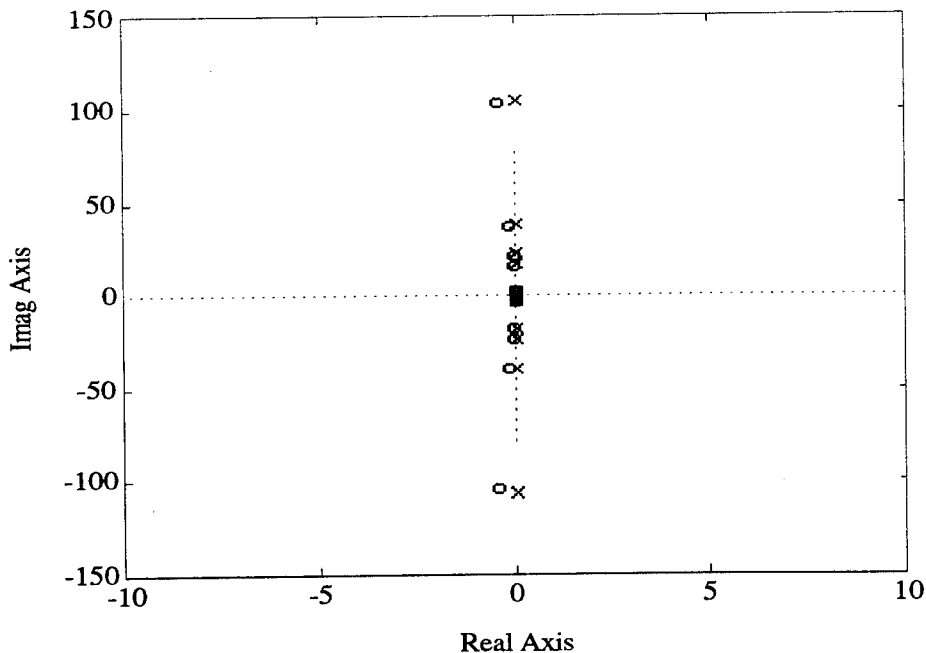

Figure 34: Poles and Zeros of Transfer Function from T to θ

41

Note that the underdamped modes appear as alternating poles and zeros near the imaginary axis. Reference 9 shows that with position and rate feedback or lead compensation, stability of the modes is achieved, that is the root locus from each open loop pole to its adjacent zero will lie in the left half plane. With angular position and rate feedback the loop transfer function is multiplied by the factor $k_1(\tau s + 1)$. The resulting root locus plot near the origin is shown in **Figure 35**, for $\tau = 4.77$. An underlying assumption is that the sensor and actuator are colocated at the "rigid" central hub of the spacecraft. With flexibility between the sensor and actuator, lead compensation can actually cause structural mode instability (see Reference 12, Appendix A.4).
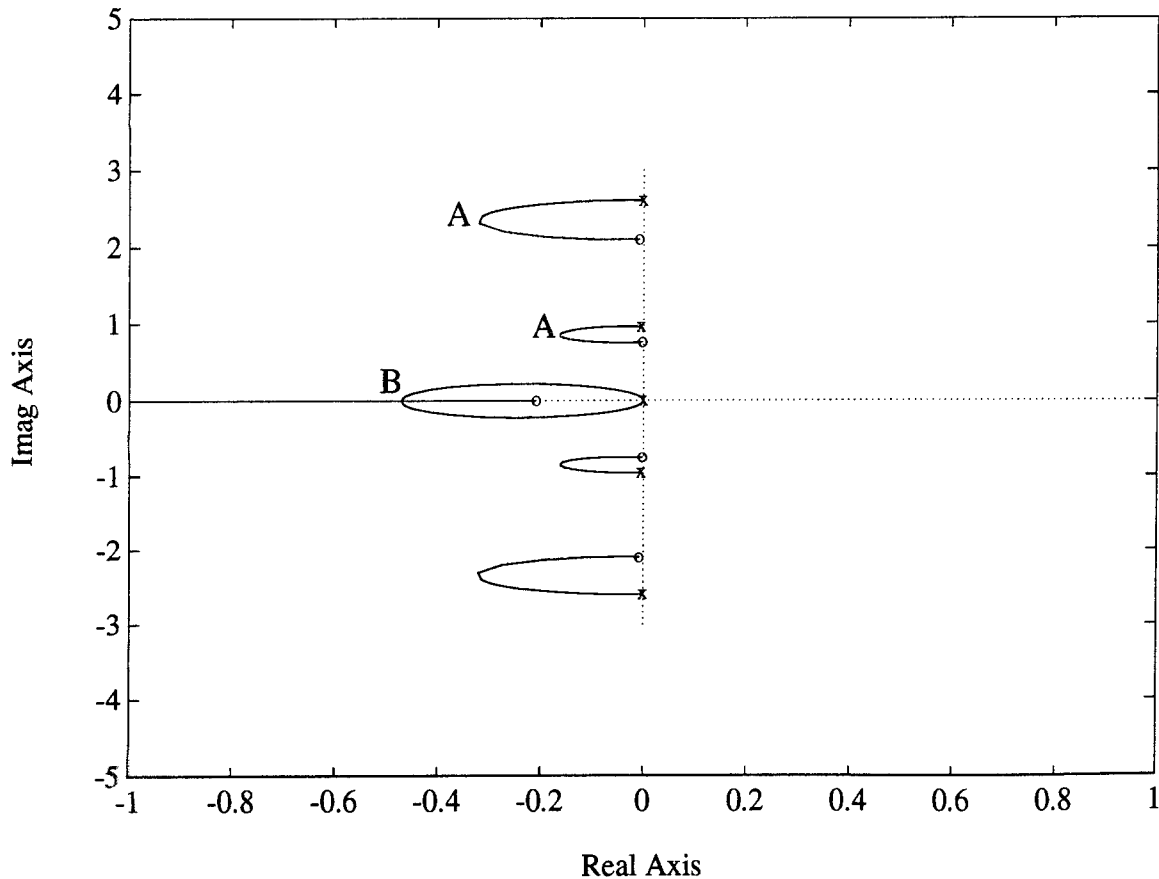

Figure 35. Root Locus vs. Forward Loop Gain With Position and Rate Feedback

If the controller gain were chosen to locate the closed loop poles near points A for maximum damping of the flexible modes, the resulting rigid body control would be considerably underdamped. More realistically, the closed loop poles would probably be placed with the rigid body pole closer to point B, for nearly-critical damping of the center body. Hence the flexible poles would be dictated by the rigid body controller, and would be much nearer the imaginary axis. Although the stable root locus plot is guaranteed with the linear controller, nonlinearity can cause closed loop pole locations to change as a function of time. Nonlinear analysis is discussed in Chapter V.

B. COMPARISON OF THRUSTER CONTROL METHODS FOR FLEXIBLE SPACECRAFT

Comparisons of bang-bang and pulse-modulated thruster control in the presence of structural flexibility are presented in this section. The first two of the six cantilever modal coordinates are plotted to give some feel for the response of the flexible appendage with respect to the central body. The simulations were run at the same sampling rate (100 Hz) and with the same basic block diagrams as the previous rigid body simulations, only the flexible body dynamics were substituted for the rigid.

1. Step Response

The ten-degree step response is shown in **Figures 36-41** for the PWPF-modulator , bang-bang, and time-optimal bang-bang controllers. The time responses of the first two modal coordinates are included to provide some indication of the arm excitation. The PWPF-modulator input gain of 30 (**Figure 36**) was reduced to 10 for the run of **Figure 37**. Note the reduced thruster firing with little loss in accuracy, as well as the rapid decay in the modal coordinate amplitudes. The oscillation in pointing angle is due to the input gain to the modulator, which increases the loop gain. Hence the original linear design with low controller bandwidth to avoid interaction with the first mode is not realized. It is possible that further "optimization" of the modulator could help improve this aspect of the results.

For the first bang-bang run (**Figure 38**), the dead bands were left as were required to provide the minimum-impulse limit cycle from the rigid body simulations (with +/-.1° excursion in θ). The resulting thruster actuation is unsatisfactory, although tight control of the center body is noted. The forward deadband was opened up to +/- .2° to produce the result of **Figure 39**. The increased deadband reduces the "density" of thruster firings, however the oscillations and firings continue until almost 200 seconds. Similar results were obtained using the time-optimal controller. The first run (**Figure 40**)

shows a much faster maneuver (as is expected), however excessive switching occurs at the termination. Again opening up the deadband (**Figure 41**) provides virtually no benefit in terms of reducing thruster firings, and results in undesirable oscillations in pointing angle. The phase plane plot is shown in this run to point out the limit-cycle-like behavior, however further investigation showed thruster firing ends after about 200 seconds. The delayed overshoot occurring just after six seconds is probably due to the "whipping" motion of the flexible appendage as it releases the energy stored during the maneuver. The amplitude of cantilever modal coordinate q_1 reaches .26, much higher than for the thrust-modulated maneuver where the amplitude is .085. The rate of decay is also more gradual than the modulator case.
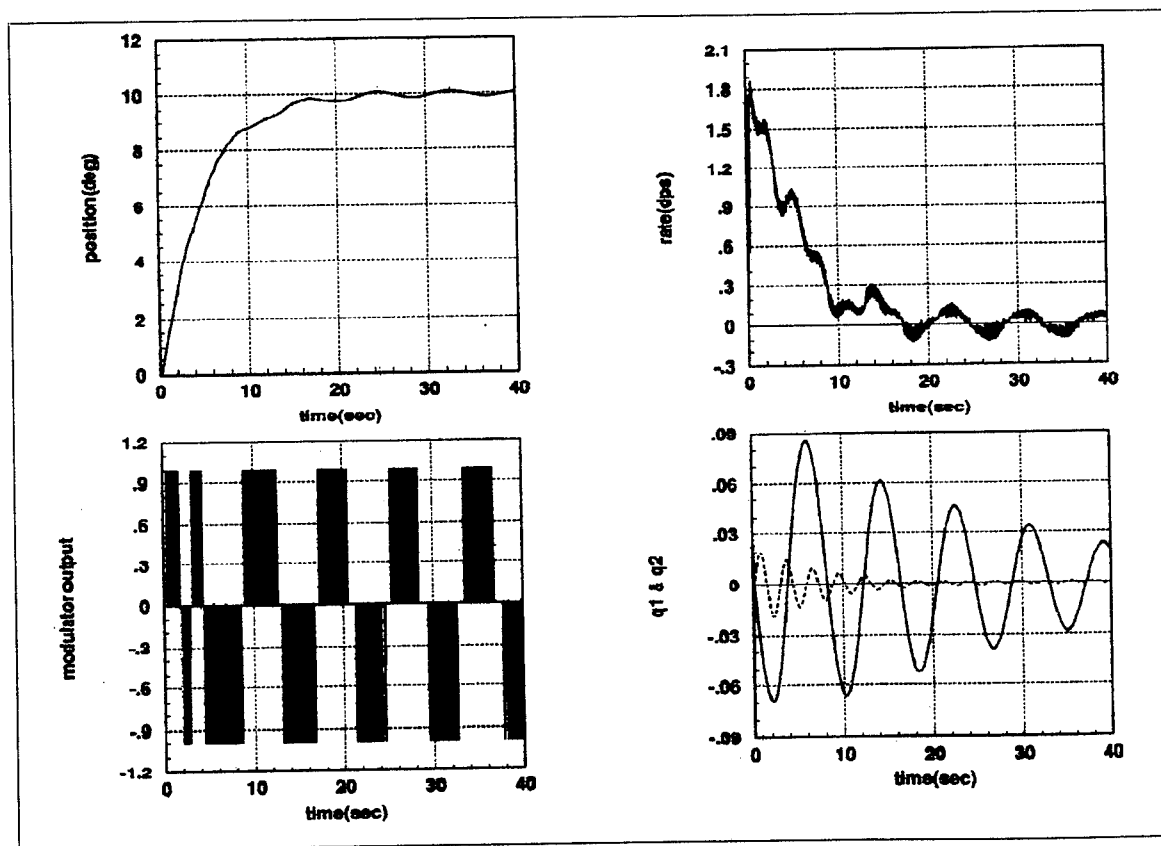

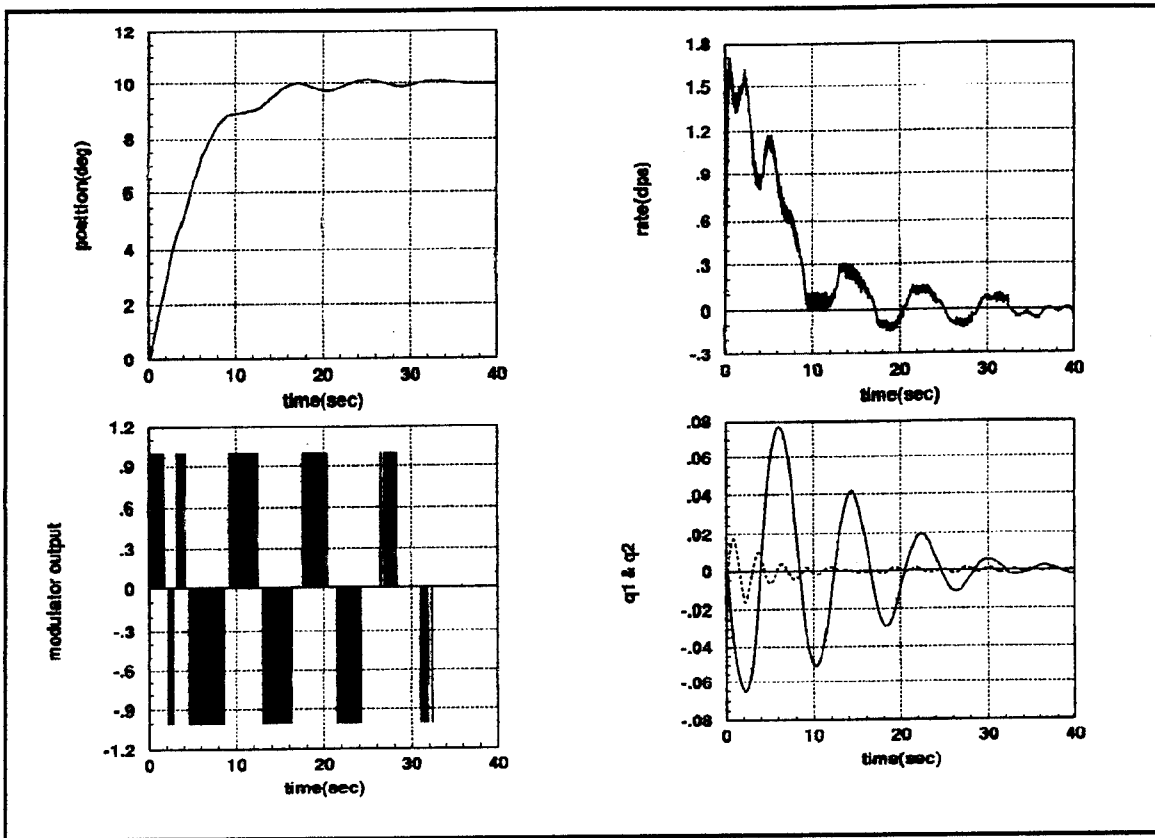**Figure 36.** **PWPF-Modulated Step Response, K=30, Flexible Dynamics**

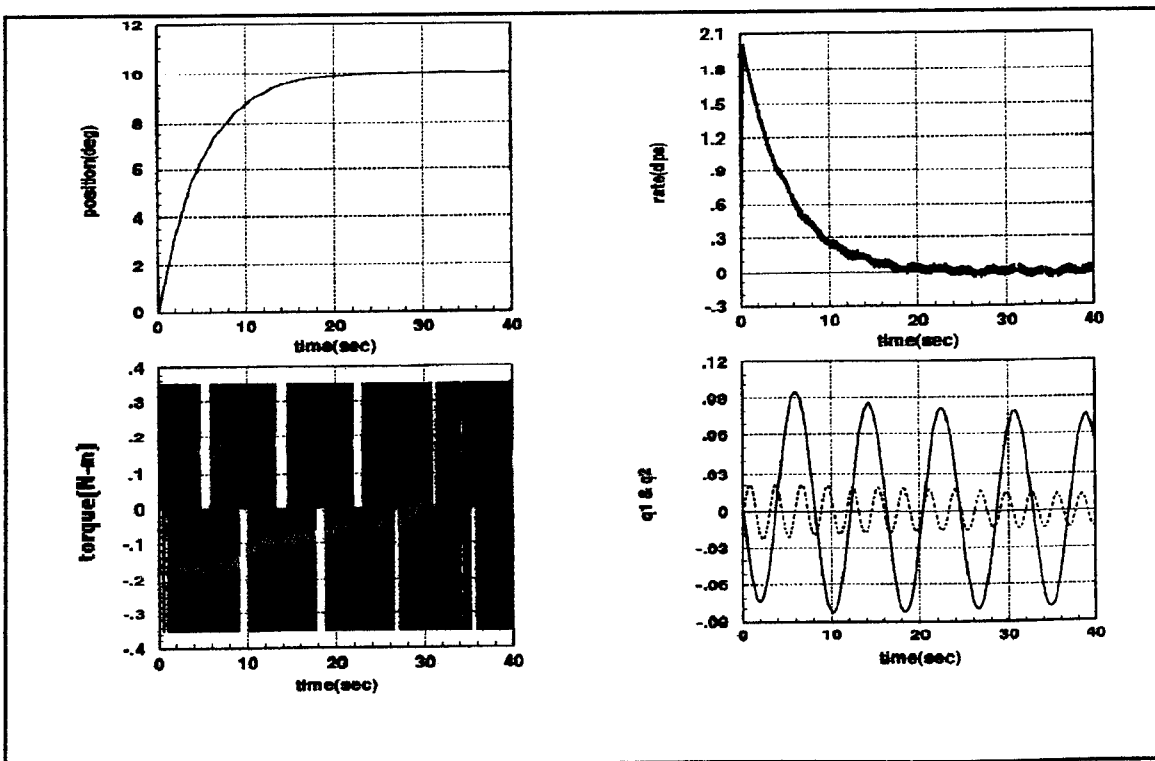Figure 37. PWPF-Modulated Step Response, K=10, Flexible Dynamics

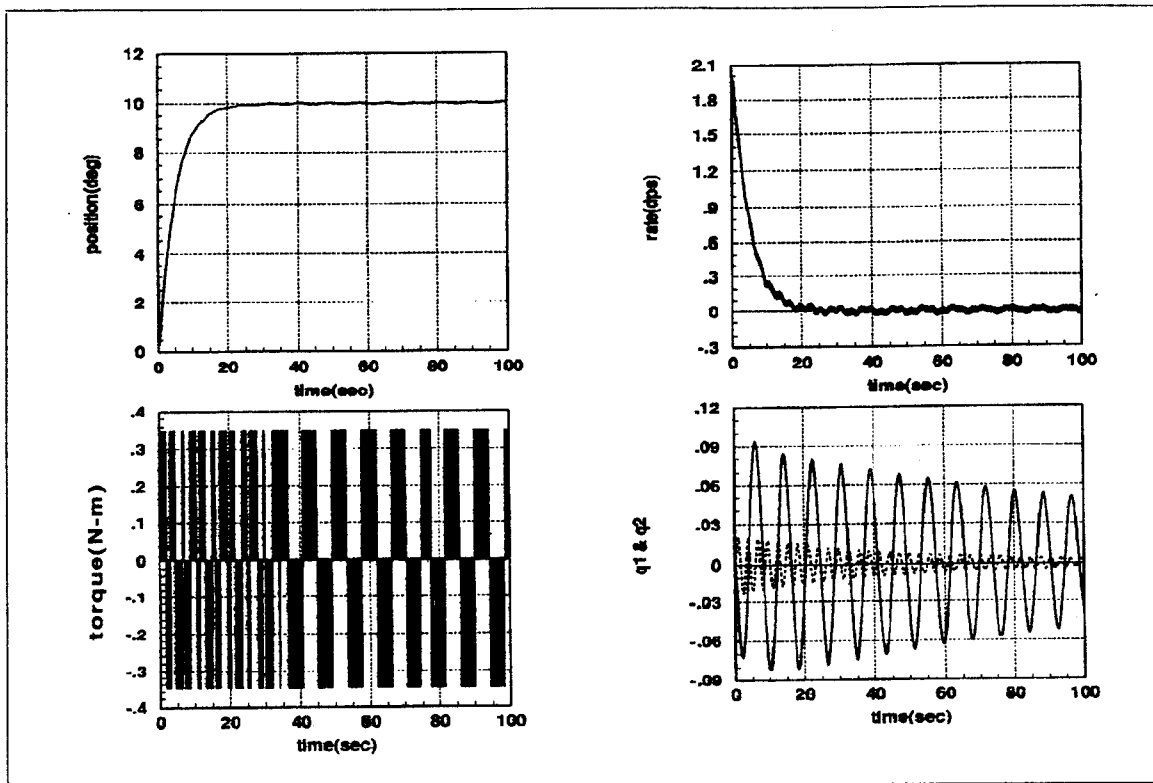Figure 38. Simple Bang-Bang Step Response, Flexible Dynamics

46

Figure 39. Simple Bang-Bang Response with Increased Deadband
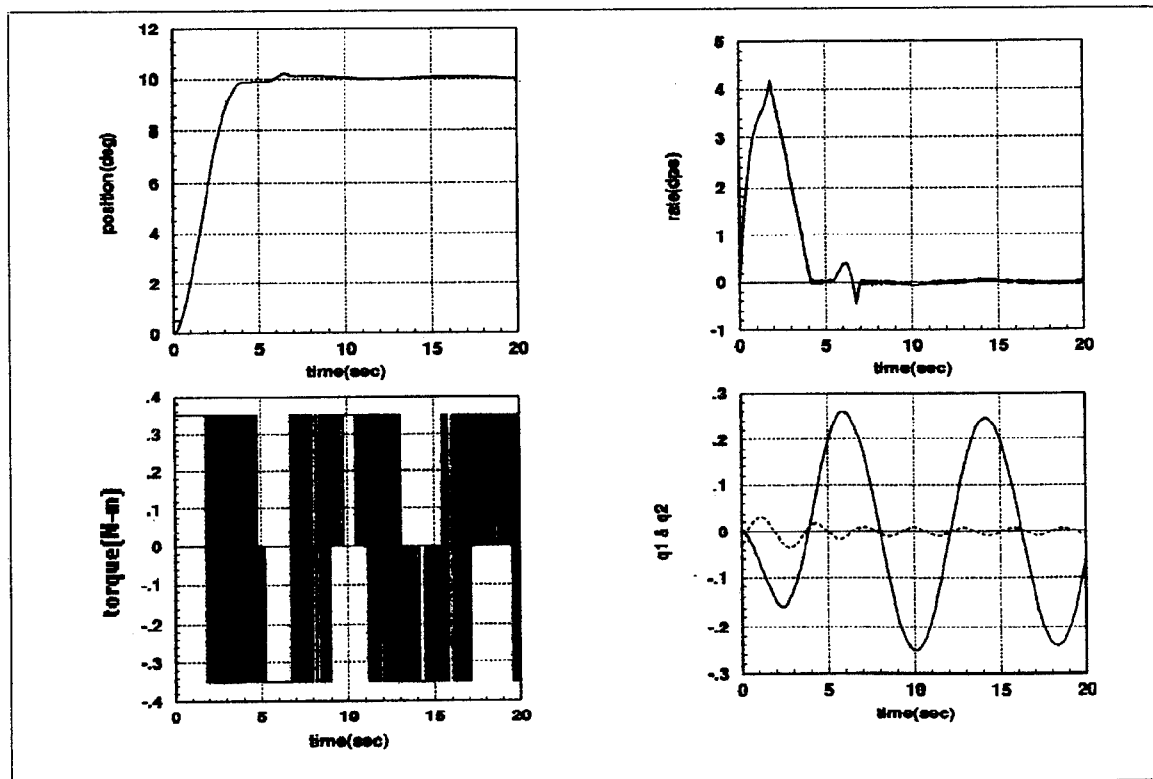
Figure 40. Time-Optimal Bang-Bang Step Response, Flexible Dynamics

47
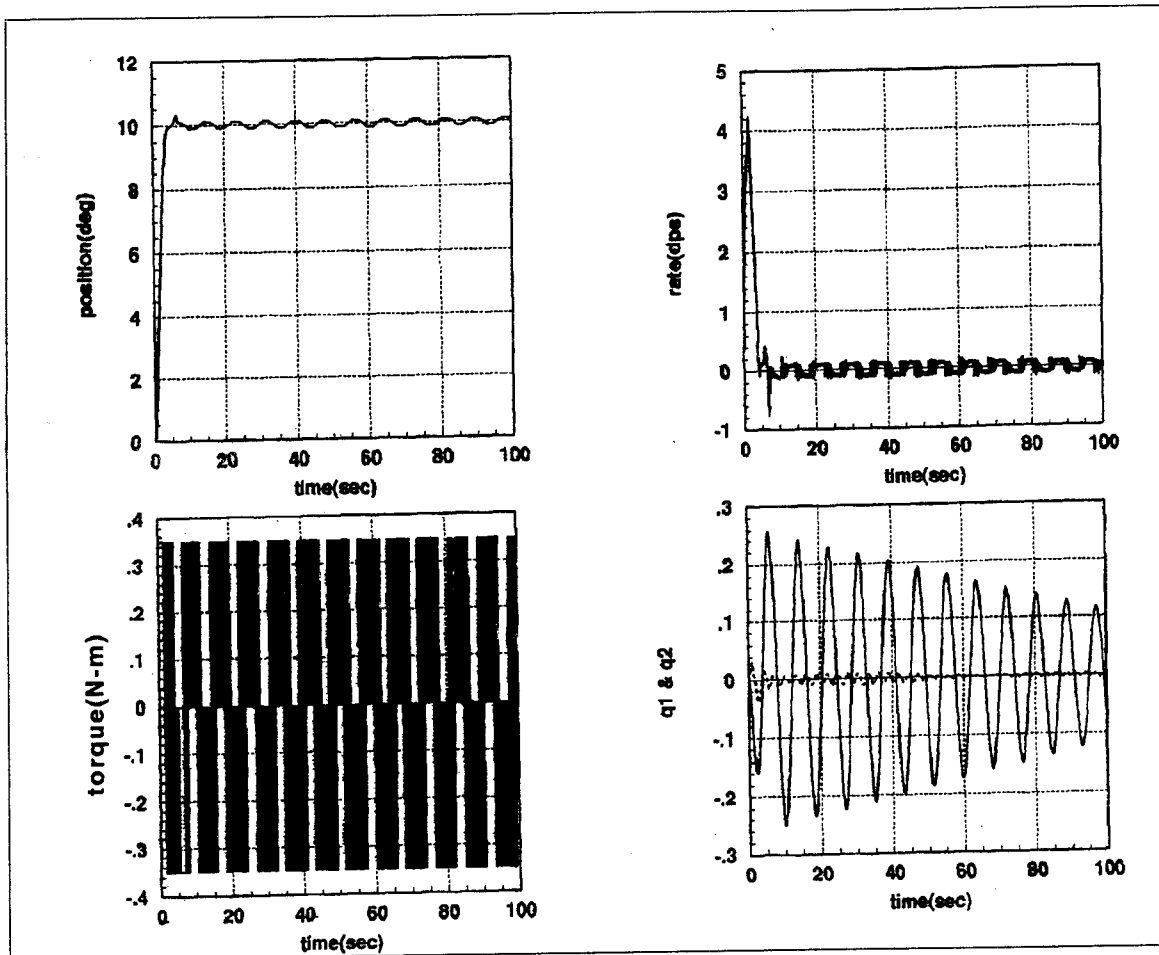
Figure 41. Time-Optimal Bang-Bang Response with Increased Deadband

Though these simulations were intended to point out the advantages of PWPF-modulated thruster control, it is important to remember that variations of each control law have been devised to improve the performance in the presence of flexibility [e.g. Agrawal & Bang, Dodds]. The basic idea in slew maneuvers is to minimize the post-maneuver energy in the flexible structure, however this desire tends to conflict with the fact that a fast slew is also desired. [Hailey] demonstrated a slewing method which developed a more gradual angular acceleration using torque-shaping and resulted in less excitation of the structure. This method and others would show similar improvement for any of the controllers.

48

2. Small Initial Condition Response

Figures 42-45 show the responses of each of the control systems to small initial conditions, where phase plane trajectories are included rather than the modal responses. Thruster activity in the first PWPF case (**Figure 42**) was reduced further by implementing an external deadband of +/- .1° before the modulator (**Figure 43**). The tradeoff is seen to be slightly less accuracy, but still well within the goal of +/- .1°. The simple bang-bang response (**Figure 44**) is comparable to the modulated response. The time-optimal bang-bang, which implements the dead bands directly in the feedback loop, is seen to bounce back and forth within the +/- .1° deadband.
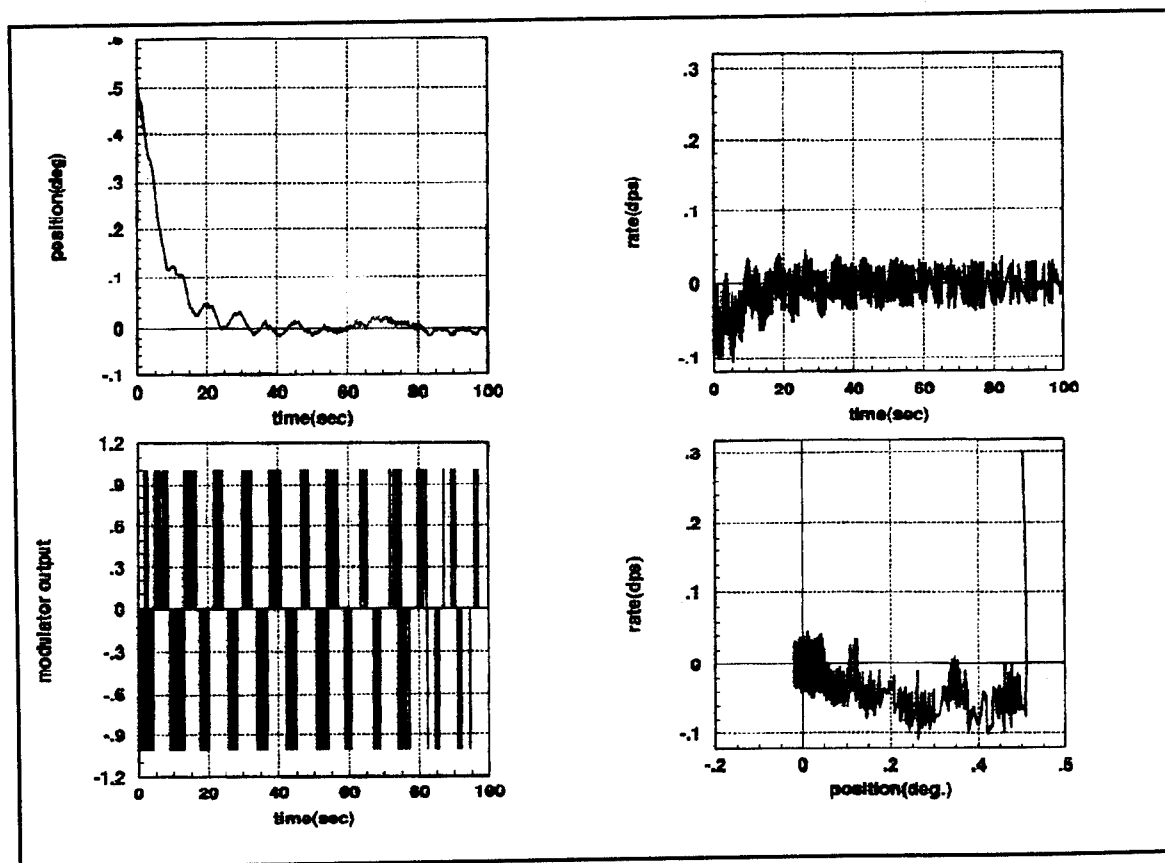

Figure 42. PWPF-Modulated Response to Small Initial Conditions, Flexible Dynamics
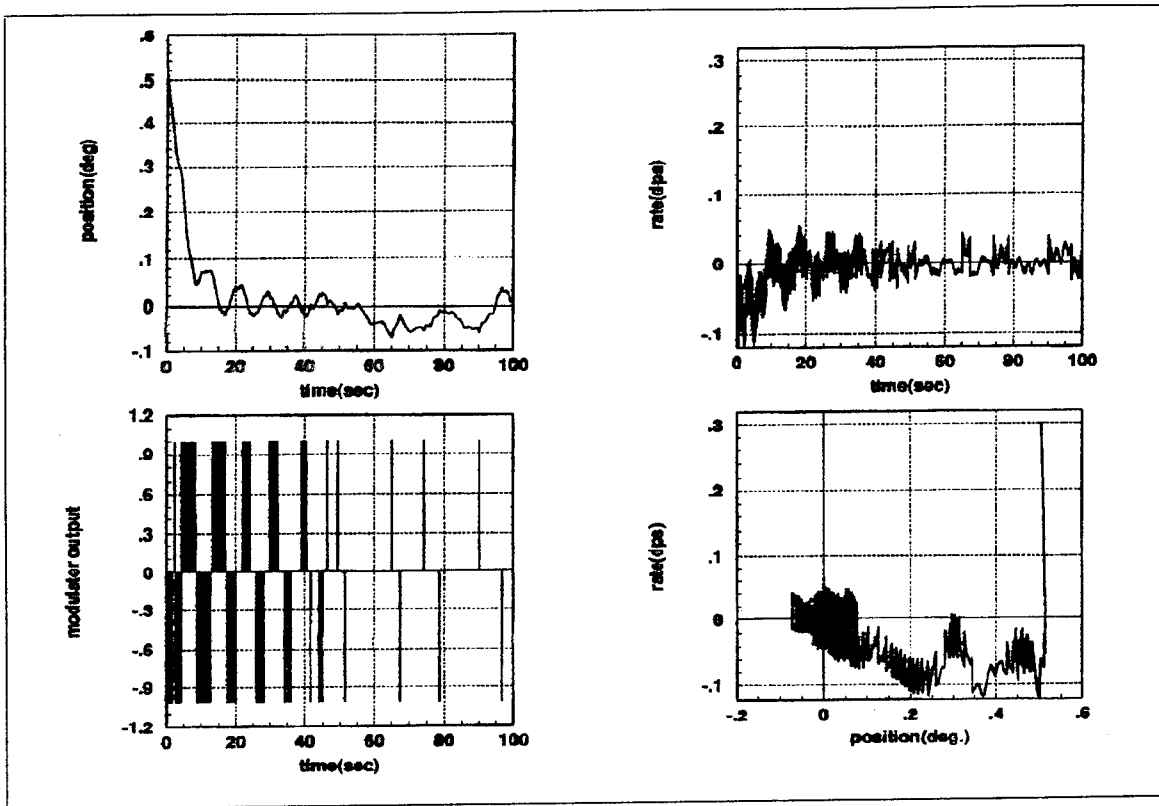
49

Figure 43. PWPF-Modulated IC Response with External Deadband
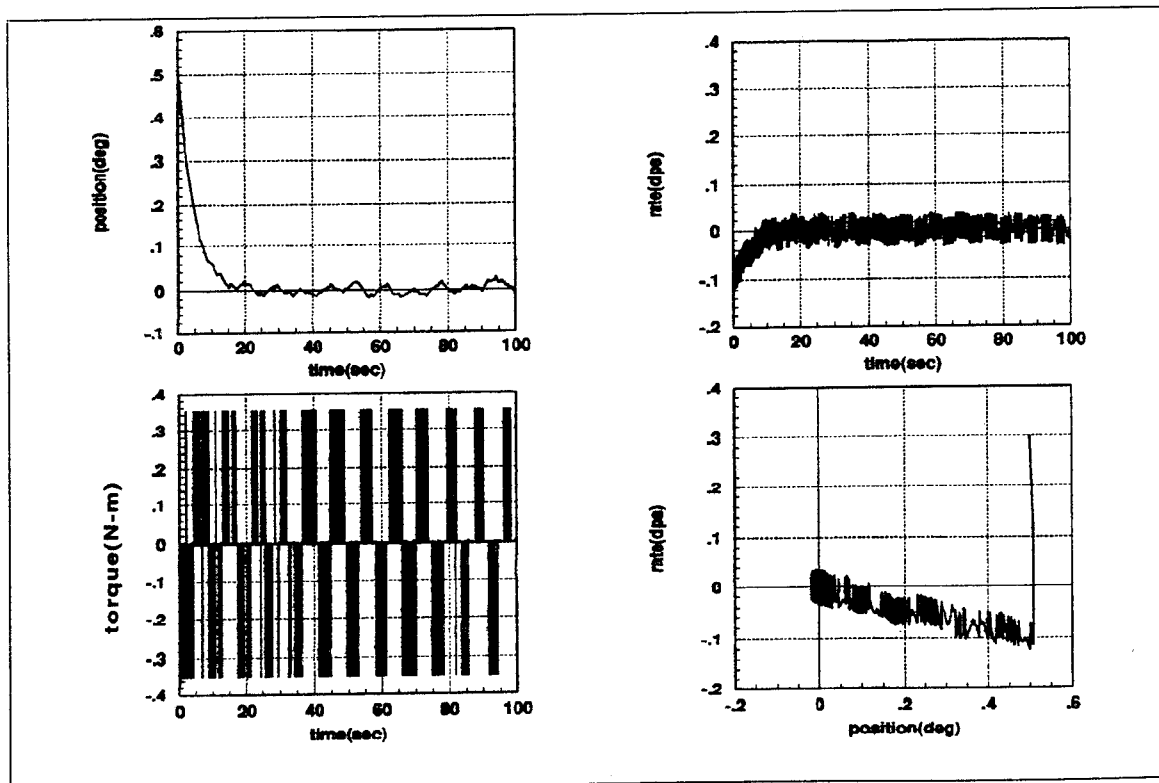
Figure 44.   Simple Bang-Bang Initial Condition Response

50
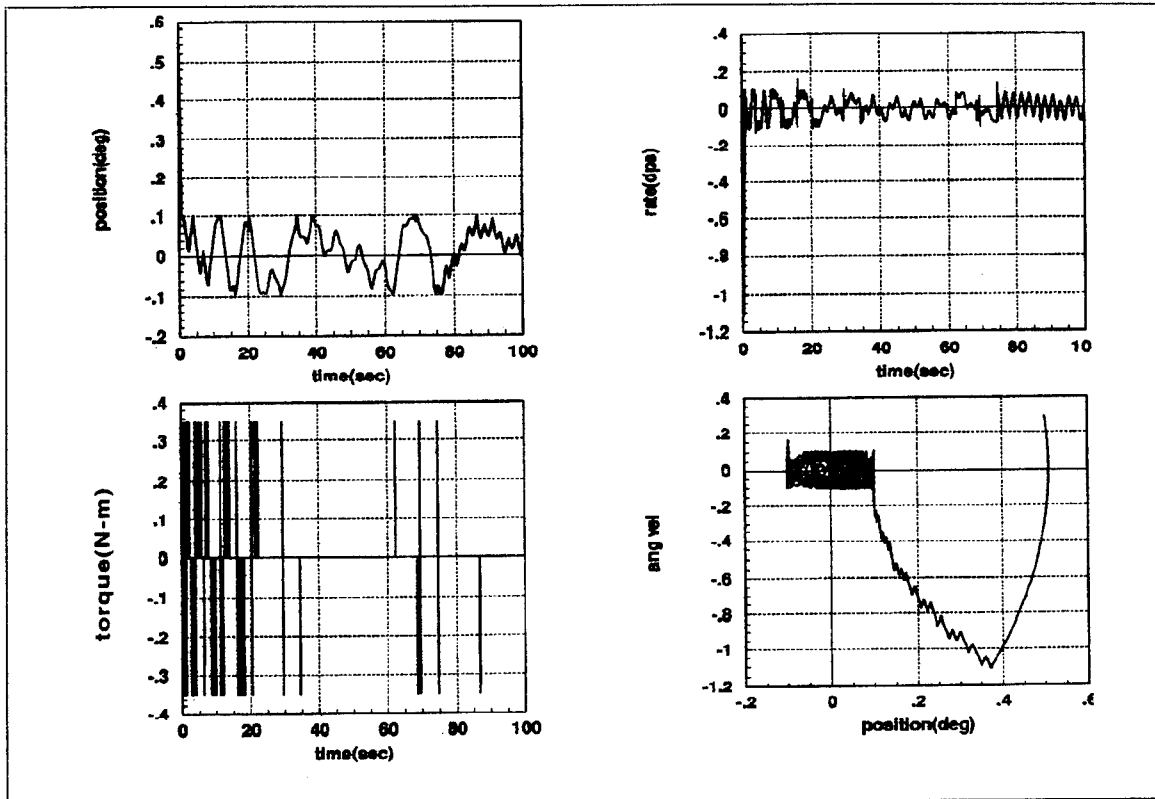
Figure 45. Time-Optimal Bang-Bang Initial Condition Response

3. Disturbance Rejection with PWPF-Modulated Controller

The behavior of the modulated control system during a constant disturbance is illustrated in **Figures 46-50**. The disturbance of .015 N-m was applied for 20 seconds (except for Figure 46), starting at one second. **Figure 46** shows that with K=30, the required pointing accuracy appears to be achieved. After the disturbance, a rigid body limit cycle of frequency .05 Hz appears to have been established. The longer run of **Figure 47** (70 second disturbance) clearly shows that the required pointing accuracy is maintained. The results of **Figures 48-50** show that as the input gain is increased, the steady-state error is reduced, however some degree of modulator instability is shown for the case of K= 200 (**Figure 50**). After the disturbance, the over-excited modulator still manages to drive the system toward zero pointing error.

Figure 46. Modulated Controller Response to Disturbance Torque, K=30
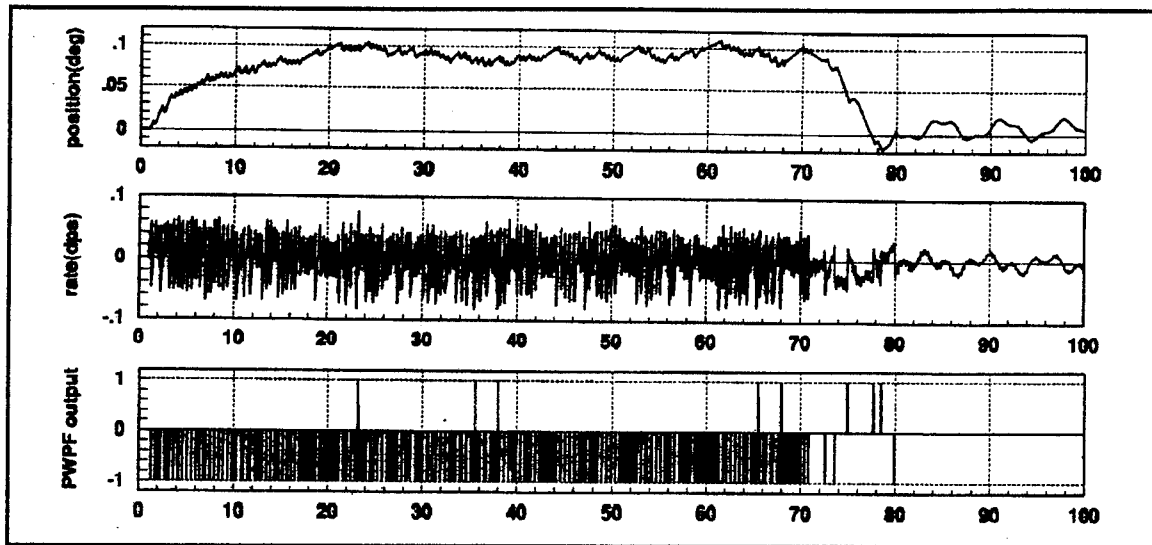
Figure 47. Modulated Controller Response to Disturbance Torque, K=30
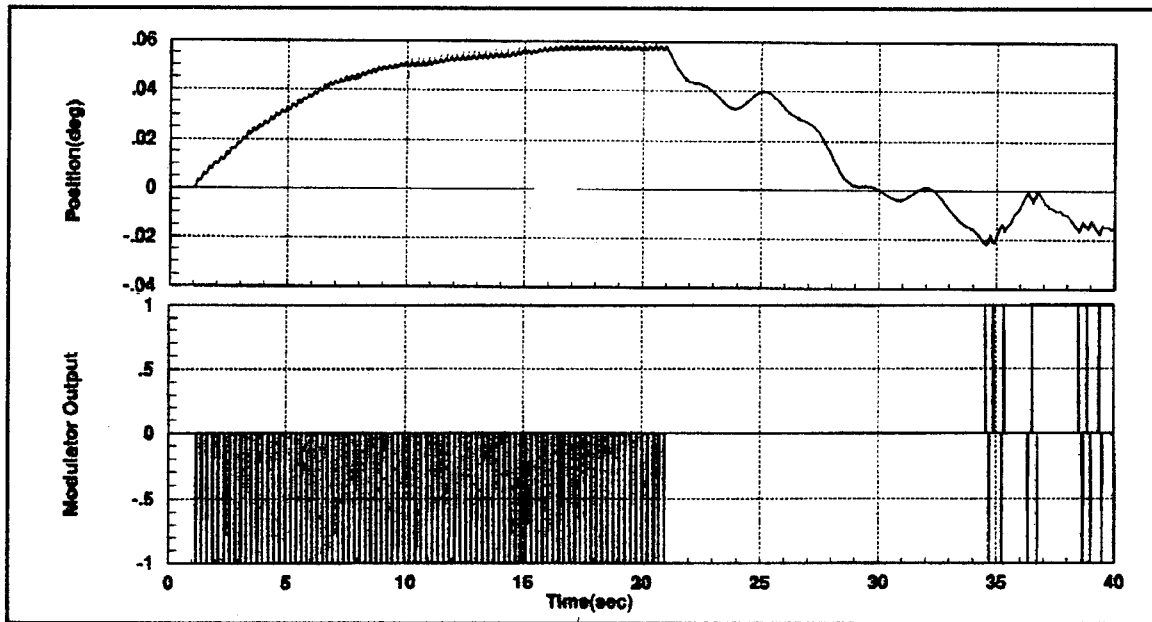
Figure 48. Modulated Controller Response to Disturbance Torque, K=50

53
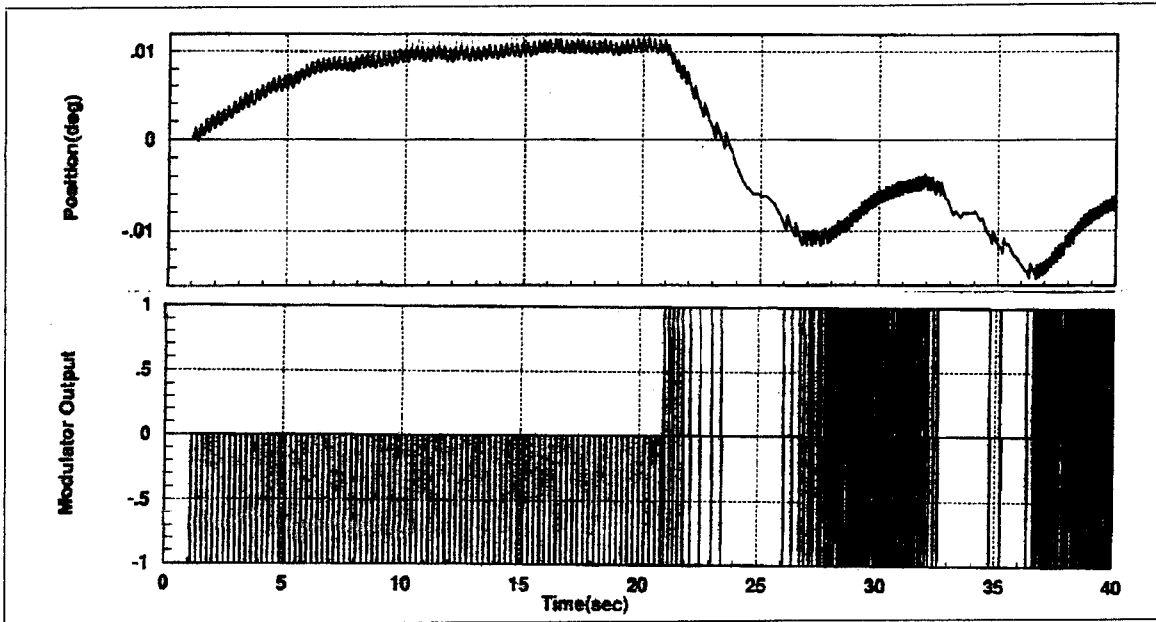
Figure 49. Modulated Controller Response to Disturbance Torque, K=100
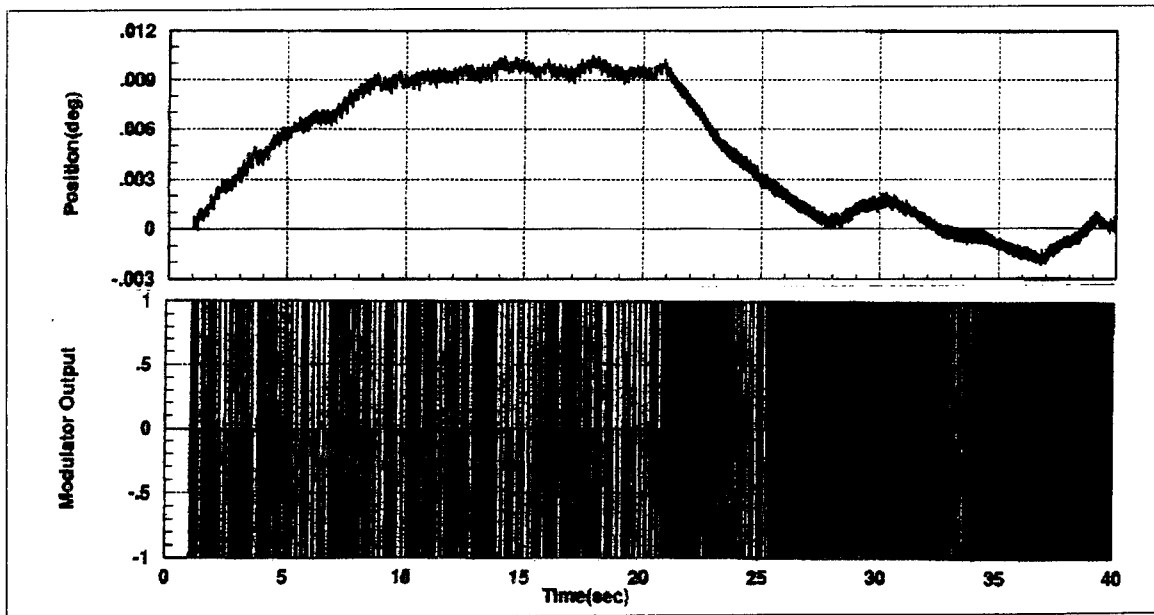
Figure 50. Modulated Controller Response to Disturbance Torque, K=200

54

V. NONLINEAR CONTROL LOOP STABILITY ANALYSIS IN THE PRESENCE OF STRUCTURAL FLEXIBILITY
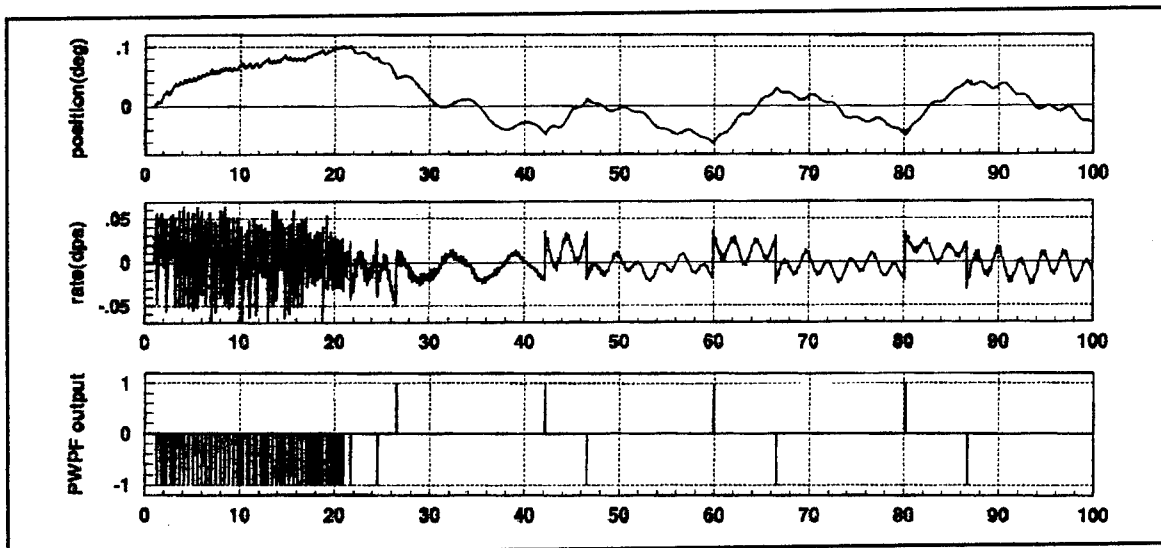
The stability of the control system is a function of all elements of the control loop. The various elements other than constant gain add phase lead or lag (along with gain contribution except in the case of pure time delay), and hence contribute to the overall gain margin and phase margin. As was previously stated, for a control loop with linear actuation and position and rate feedback, the stability of each mode is assured. Though the control loop may induce oscillations in the structure, the oscillations will experience exponential decay. The discontinuous nature of the PWPF modulator, however, can cause the control to interact with the dynamics and result in self-sustained, or limit cycle, oscillations.

A. LIMIT CYCLE DETERMINATION USING DESCRIBING FUNCTION ANALYSIS

In order to predict the existence and characteristics of limit cycles in a system, describing function analysis can be employed. Consider the block diagram depiction of a system which has been separated into linear and nonlinear elements (**Figure 51**, adapted from Reference 2).
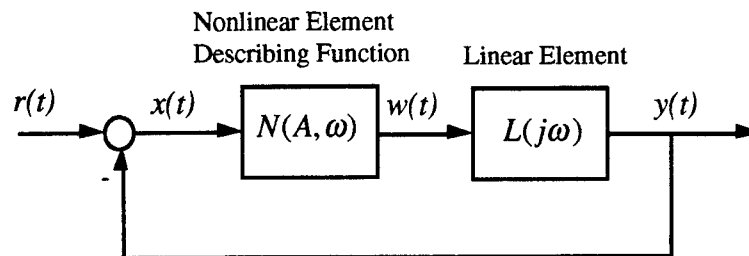
Figure 51. Control System with Nonlinear Element

For a sinusoidal input to the nonlinear element, i.e. $x(t) = A\sin(\omega t)$, the output $w(t)$ of the nonlinear element is generally periodic and hence can be represented by a Fourier series expansion. The describing function method makes the approximation that only the components corresponding to the fundamental harmonic of the expansion, $n\omega$ with $n=1$, are to be considered. This approximation is based on the assumption that the linear element has low-pass properties and hence tends to attenuate the higher harmonics of $w(t)$. The describing function of the nonlinear element is defined as the complex fundamental-harmonic gain of a nonlinearity in the presence of a driving sinusoid [Ref. 14]:

$$N(A, \omega) = \frac{\text{phasor representation of output component at frequency } \omega}{\text{phasor representation of input component at frequency } \omega}$$

$$= \frac{A_1(A, \omega)}{A} e^{j\phi_1(A, \omega)} \qquad (26)$$

$$= \frac{1}{A}(b_1 + ja_1)$$

where the magnitude and phase of the describing function are

$$|N(A, \omega)| = \frac{1}{A}\sqrt{a_1^2 + b_1^2}$$

$$\angle N(A, \omega) = \phi = \tan^{-1}(a_1 / b_1) \qquad (27)$$

The describing function $N(A, \omega)$, is analogous to the frequency response function, $H(j\omega)$, of a linear system. But whereas the linear frequency response function is independent of the amplitude of the input signal, the nonlinear "transfer function" or describing function depends on both the input amplitude and frequency. In linear control loop design, closed-loop poles can be placed to assure a stable response. With a nonlinear element, however, the closed-loop pole locations vary with time due to the gain variation

56

with input amplitude. Hence, the root locations in the complex plane can oscillate between locations in the left and right-half plane, giving rise to limit cycle behavior.

By representing the nonlinear element by a describing function approximation, some of the same graphical techniques from linear control analysis can be employed to predict the limit cycle behavior and to determine stability margins with respect to the limit cycle condition. Consider the configuration from Figure 51, assuming that a self-sustained oscillation of amplitude A and frequency ω is established and hence the input, $r(t) = 0$. The following relations can be obtained from the figure:

$$x = -y$$

$$w = N(A,\omega)x$$

$$y = L(j\omega)w$$

and hence

$$y = L(j\omega)N(A,\omega)(-y) , \text{ or}$$

$$y(1 + L(j\omega)N(A,\omega)) = 0$$

Since y≠0, the limit cycle frequency and amplitude must satisfy the relationship

$$L(j\omega) = -\frac{1}{N(A,\omega)} \tag{28}$$

A bode plot representation of a system with nonlinearity is depicted in **Figure 52**. The negative inverse of the describing function gain and phase are superimposed with the linear plot. The gain and phase margins are redefined with respect to the nonlinear boundary, as opposed to the -180 degree phase and 0 dB gain lines. The limit cycle frequency and amplitude corresponds to the point which satisfies Equation (28), the point of intersection between the nonlinear and linear gain plots.
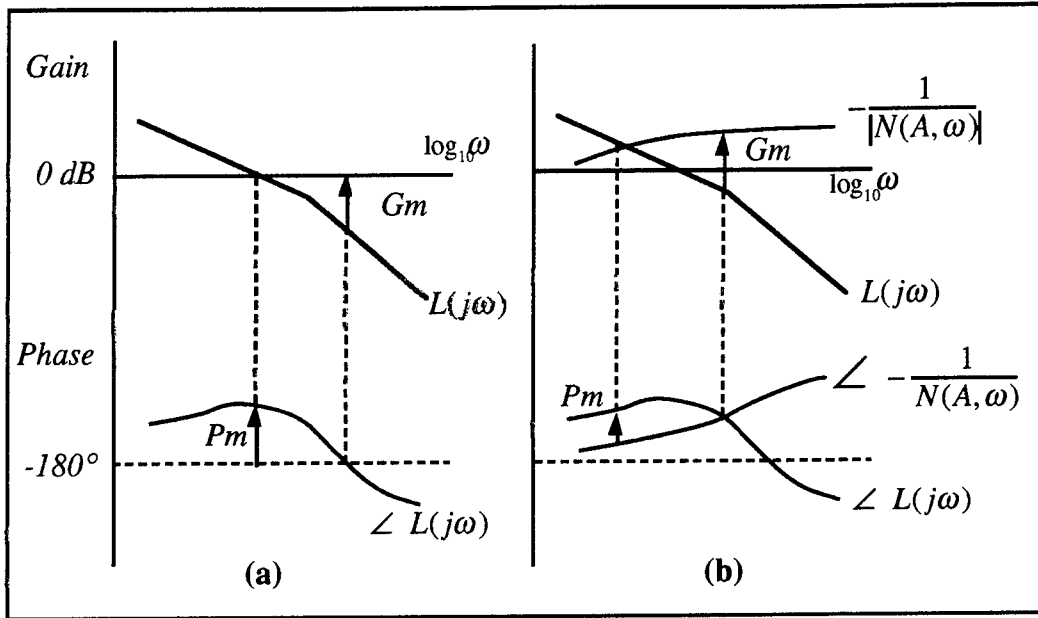
Figure 52. Gain Margin (Gm) and Phase Margin (Pm) for (a) Linear System, and (b) System with Nonlinear Element

B. ANALYSIS OF PWPF MODULATOR

For the rigid body case, the limit cycle frequency was easily determined by simulation. With a flexible spacecraft the dynamic characteristics of the modulator need to be considered in order to predict the limit cycle behavior which can result from the interaction of the nonlinearity of the PWPF modulator with the control system. The dynamic characteristics can be analyzed using the describing function method.

Although the describing function method is based on the assumption that only the fundamental harmonic of the nonlinear response is significant, the residual higher harmonics have been considered [Ref. 14]. The corrected-conventional describing function uses the root-mean-square value of the first and third harmonics, with the phase of the fundamental. A corrected-conventional single input describing function (SIDF) for the PWPF modulator is presented in Reference 1, for which the gain and phase of the SIDF boundary, $N(A_m, j\omega)$, are determined to be

$$Gain(dB) = 20\log(B/A_m)$$
$$Phase(\text{deg}) = -57.3\tan^{-1}(T_m\omega)$$

(29)

where

$$h = U_{on} - U_{off} = \text{hysteresis width}$$

$$A_m = \left[U_{on} - \frac{h}{1 + \exp(\Delta/(T_m\omega))}\right]\frac{\sqrt{(T_m\omega)^2 + 1}}{K_m}$$

$$B = \sqrt{B_1^2 + B_3^2}$$

$$B_1 = \frac{4U_m}{\pi}\sin\left(\frac{\Delta\omega}{2}\right)$$

$$B_3 = \frac{4U_m}{3\pi}\sin\left(\frac{3\Delta\omega}{2}\right)$$

$$h = U_{on} - U_{off} = \text{hysteresis width}$$

$$\omega = \text{ input frequency (rad / s)}$$

$$\Delta = \text{ minimum pulse width (s)}$$

A block diagram representation of the continuous-time control system is shown in **Figure 53**.
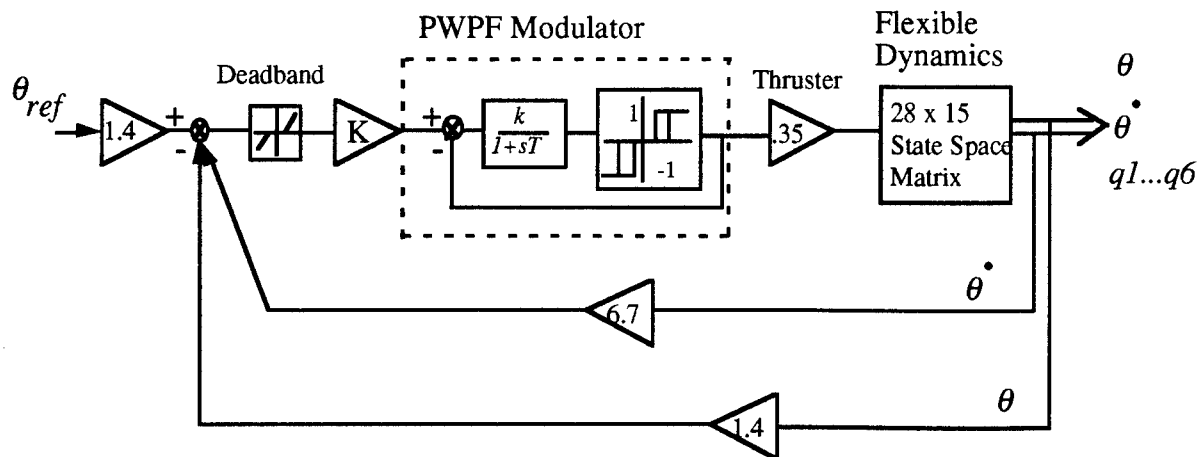
Figure 53. PWPF-Modulated Thruster Control Loop

59

Bode plots for the control loop were developed in Matlab using the continuous-time dynamics description from Equation (24). The code is included in **Appendix C**. The bode plot for the first five pole-zero pairs of the plant dynamics is shown in **Figure 54**. The gain plot agrees closely with that found in Matrix$_X$ using the DBODE command on the discrete-time state space model of the plant (see Figure 32). The phase plot from Matrix$_X$, however, shows phase lag at the higher frequencies which is not seen in Figure 54. This is thought to be another consequence of the discretization process. The possible effect that this discrepancy could have is that the predicted phase margin with respect to a limit cycle may be smaller than the analysis using the Matlab model would indicate.
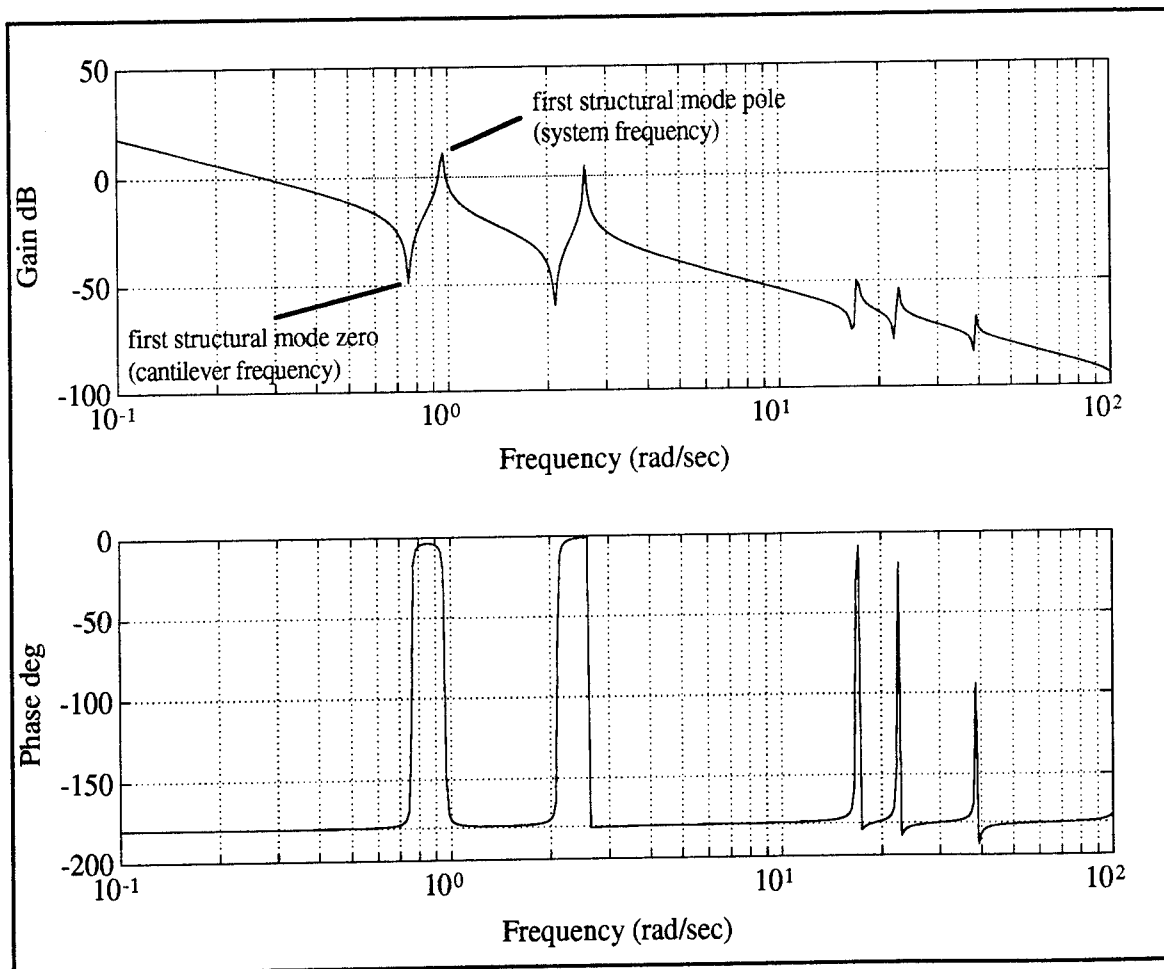
Figure 54. Bode Plot of Flexible Dynamics

60

Figure 55 shows the plant with position and rate feedback control (with K=30) superimposed with the SIDF boundary developed using Equations (29). The nonlinear boundary intersects the linear plot for the first five modes, with linear control loop gain reduction for the sixth system mode frequency sufficient enough that limit cycle interaction is not predicted. Hence five possible limit cycle interactions are indicated; only the third structural mode limit cycle at ≈ 21 rad/sec was found to be significant, as will be discussed shortly. It is interesting to note that in Reference 1 only the first mode pole (representing the first system mode of vibration) needed to be considered because the other modes of vibration were far removed in frequency from the first and thus far below the SIDF boundary. For the flexible spacecraft model in this study, however, the modal density was high enough that higher frequency flexible mode limit cycles could be expected. Hence a fairly accurate plant model is desired since exclusion of the higher frequency modes in initial analysis would fail to predict the higher frequency limit cycles.
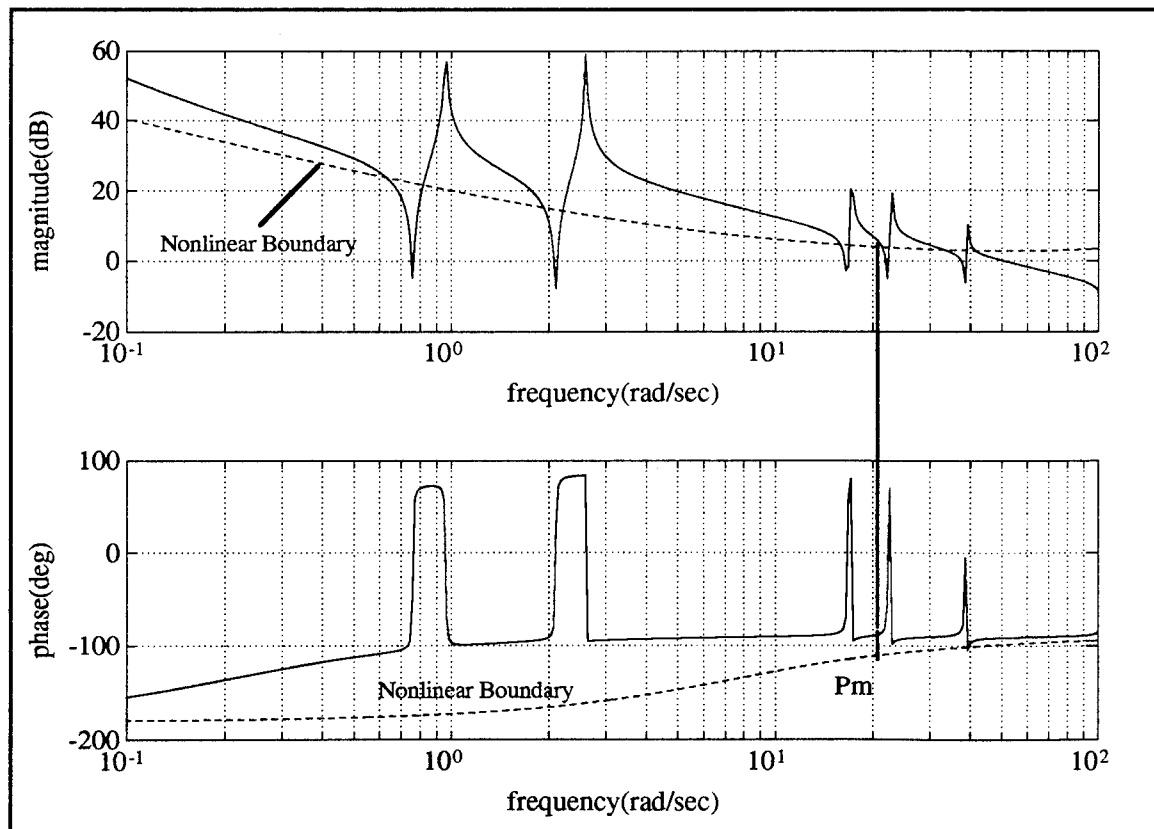
Figure 55. Control Loop Bode Plot with Nonlinear Boundary, K=30.

61

Note that the position and rate feedback effectively provide lead compensation which is indicated in Figure 55 by the increase in gain of the higher frequency underdamped pole-zero pairs (in addition to the 32 dB contributed by the total gain factor of 42), and by the phase lead. The phase lead is desirable as it provides greater phase margin with respect to the nonlinear boundary. The gain increase however causes the linear boundary to intersect with the SIDF boundary at the higher frequencies where limit cycle interaction is of even more concern since higher frequency limit cycles are more wasteful of fuel. With the lead effect modeled as $\tau s + 1$, a decrease in the rate feedback gain τ would increase the break frequency and hence lessen the gain increase seen for the third-through-fifth pole-zero pairs. But it follows from Equation 12 (Chapter III) that this would also decrease the damping ratio, which may produce undesirable system response (i.e. too much overshoot).

The stability of the control loop with respect to the third structural mode limit cycle can be evaluated by adding pure time delay to the control loop, which introduces phase lag with no gain contribution. With a large enough time delay the phase margin is effectively eliminated and limit cycling is predicted to occur. Pure time delay in the s-domain is by definition:

$$G(s) = e^{-Ts} \tag{30}$$

where T is the delay time.

Employing a Taylor series expansion where higher order terms are neglected, an approximation to pure time delay with sample and zero-order-hold [Ref. 1] is

$$\frac{1 - e^{-Ts}}{Ts} \cong \frac{1}{T^2 s^2 / 12 + Ts / 2 + 1} \tag{31}$$

Note that for this analysis the use of continuous-time descriptions of the control loop elements is founded because the sampling rate used in the discrete-time simulations is sufficiently higher than the dynamic response frequencies.

A time delay of 60 msec was added to the control loop via the formulation of Equation (31). **Figure 56** shows that for the 60 msec time delay, the phase margin with respect to the third structural mode limit cycle has vanished and hence limit cycling is predicted to occur. This will be verified through simulation in the next section.
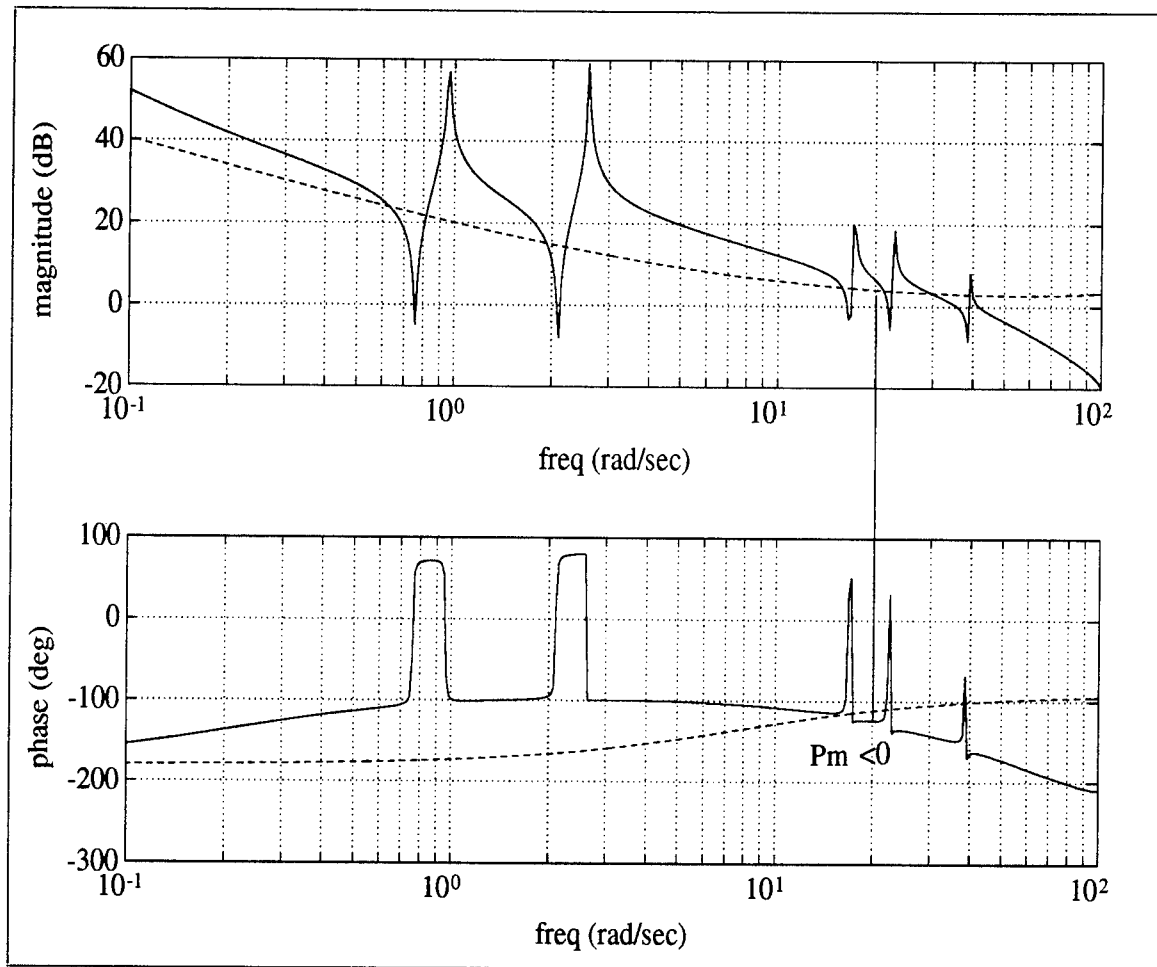
Figure 56. Loop Bode Plot with 60 msec Delay, K=30.

C. SIMULATION OF LIMIT CYCLE BEHAVIOR

The analytical stability margin was verified by adding loop time delay to the simulation block diagram and performing simulations for various delay times. In real satellite control system implementation, the on-board processing capability often limits the sampling rate and the speed with which each subsequent control signal command is computed. A multi-rate sampling scheme was incorporated to simulate the microprocessor sampling interval (which contributes to the delay). The block diagram of **Figure 57** incorporates the two sampling rates and the process delay. The microprocessor sampling interval was chosen to be 40 msec. The total time delay is a combination of the microprocessor sampling interval and pure computational delay. The PWPF modulator continues to cycle at 100 Hz (providing pulse command updates every 10 msec), but receives an input signal every 40 msec. Hence the modulator sees a constant input for four 10 msec cycles at a time.
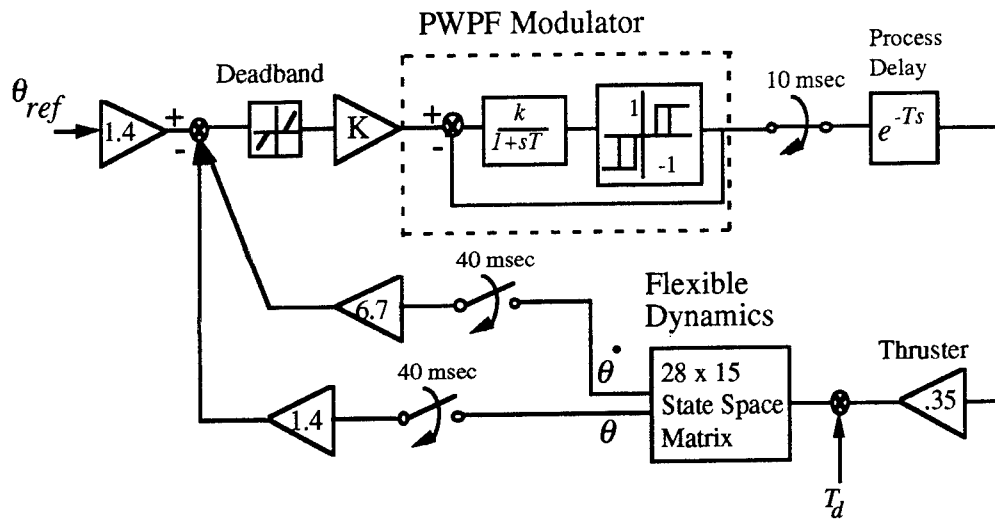
Figure 57. Higher Fidelity Control Loop Model

The structural mode limit cycle was excited in the simulations first by placing initial conditions on the controlled angle (θ) and the modal coordinate (q_i) corresponding to the deformed shape of the satellite and flexible appendage, for whichever mode was closest to

64

the predicted limit cycle frequency. It was found, however, that just about any initial condition would trigger the limit cycle in the presence of the proper amount of time delay. **Figures 58** and **59** shows the time history of the physical and modal coordinates, respectively with initial conditions on θ, q_1 and q_2, and a 60 msec time delay. A limit cycle of frequency 17.3 rad/sec is established after about four seconds, close to the predicted frequency of about 20 rad/sec from the analysis of Figure 56. The limit cycle amplitude (from the q plot) is of acceptable magnitude, within the pointing accuracy "requirement" of +/- .1 degrees. Note the decay of all modal coordinates except q_3, which grows in amplitude to the limit cycle condition. The PWPF modulator output shows sustained alternating positive and negative thruster firings, characteristic of the limit cycle condition.

The modal coordinate time histories could be converted into physical arm deflections. However, the modal magnitudes are somewhat smaller than in the results from Reference 7, indicating that the physical deflections are not of concern from the standpoint of the possibility of structural damage. Also, the main concern here is the control of the central body.
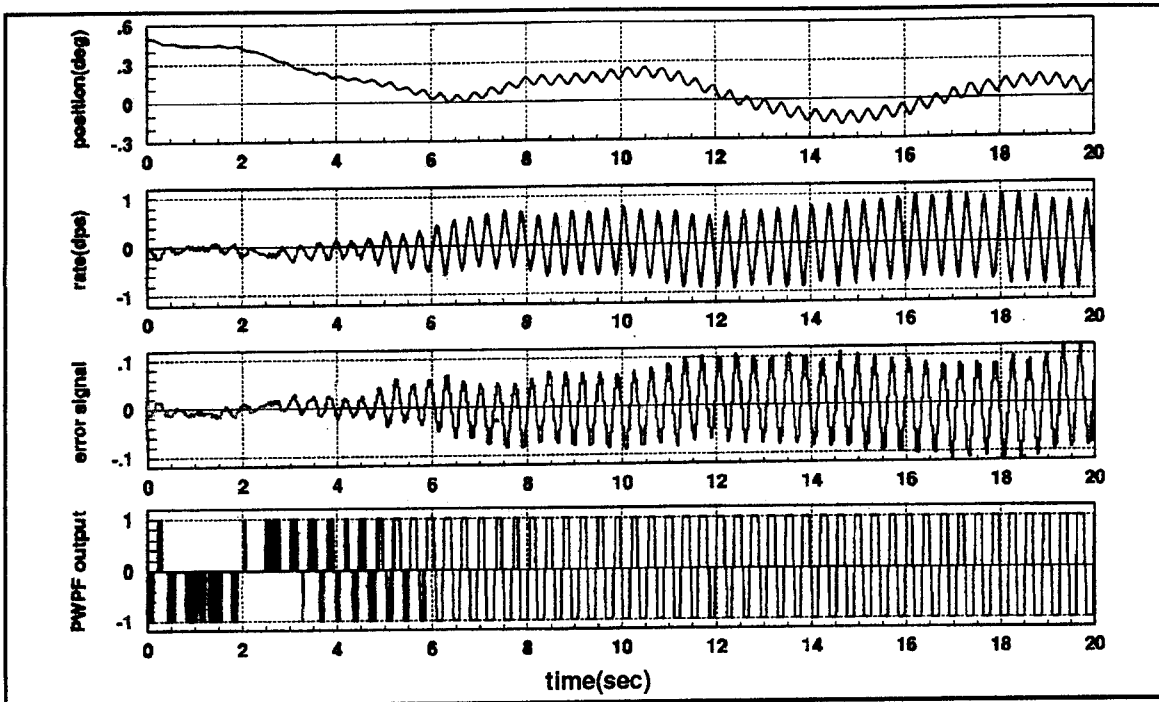
Figure 58. Initial Condition Response with K=30, 60 msec Delay
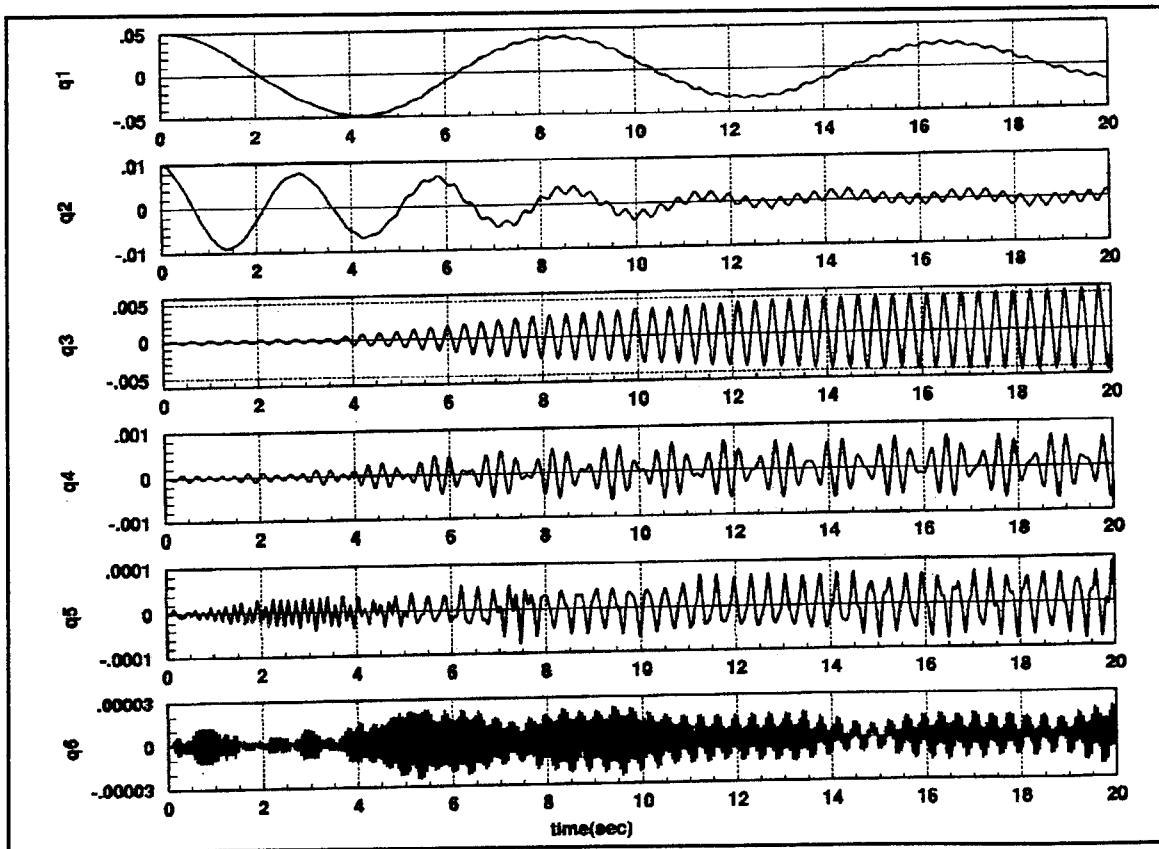
Figure 59. Initial Cond. Modal Response with K=30, 60 msec Delay

66

Figures **60** and **61** show that with a reduced time delay of 20 milliseconds the limit cycle is not excited. Note the .12 Hz oscillation in θ , the frequency of the first cantilever mode. It was not possible to excite limit cycles near the fourth and fifth system modes, as predicted by the analysis.
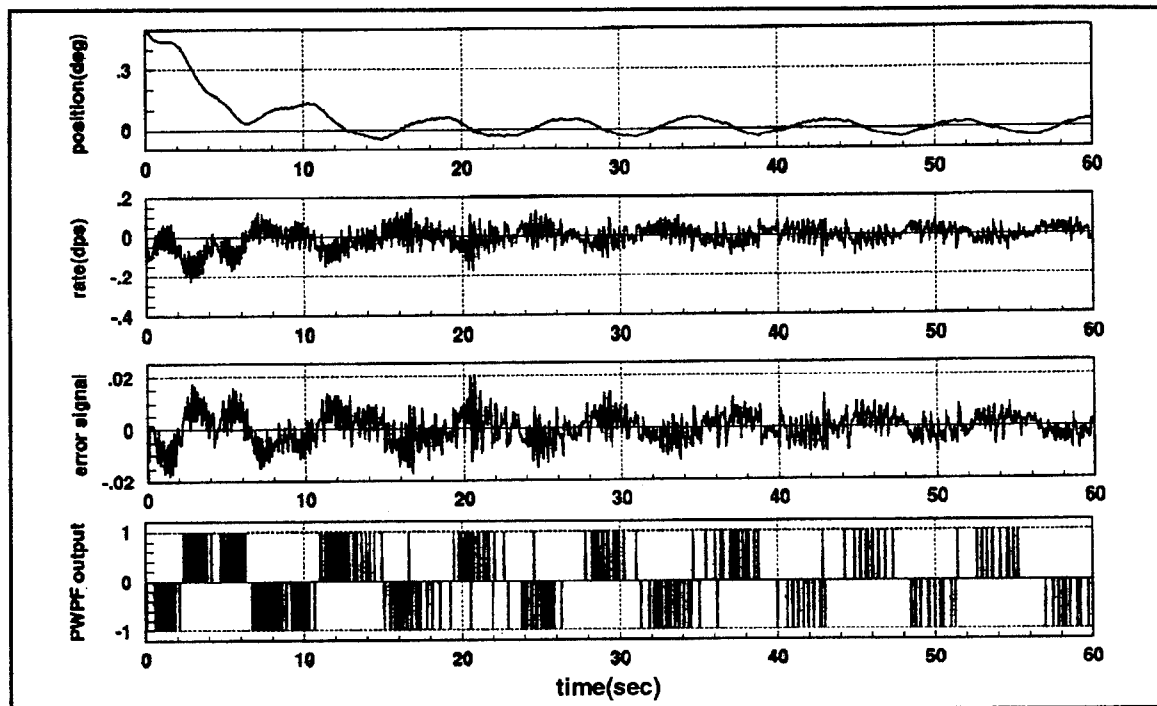
Figure 60. Initial Condition Response, K=30, 20 msec Delay
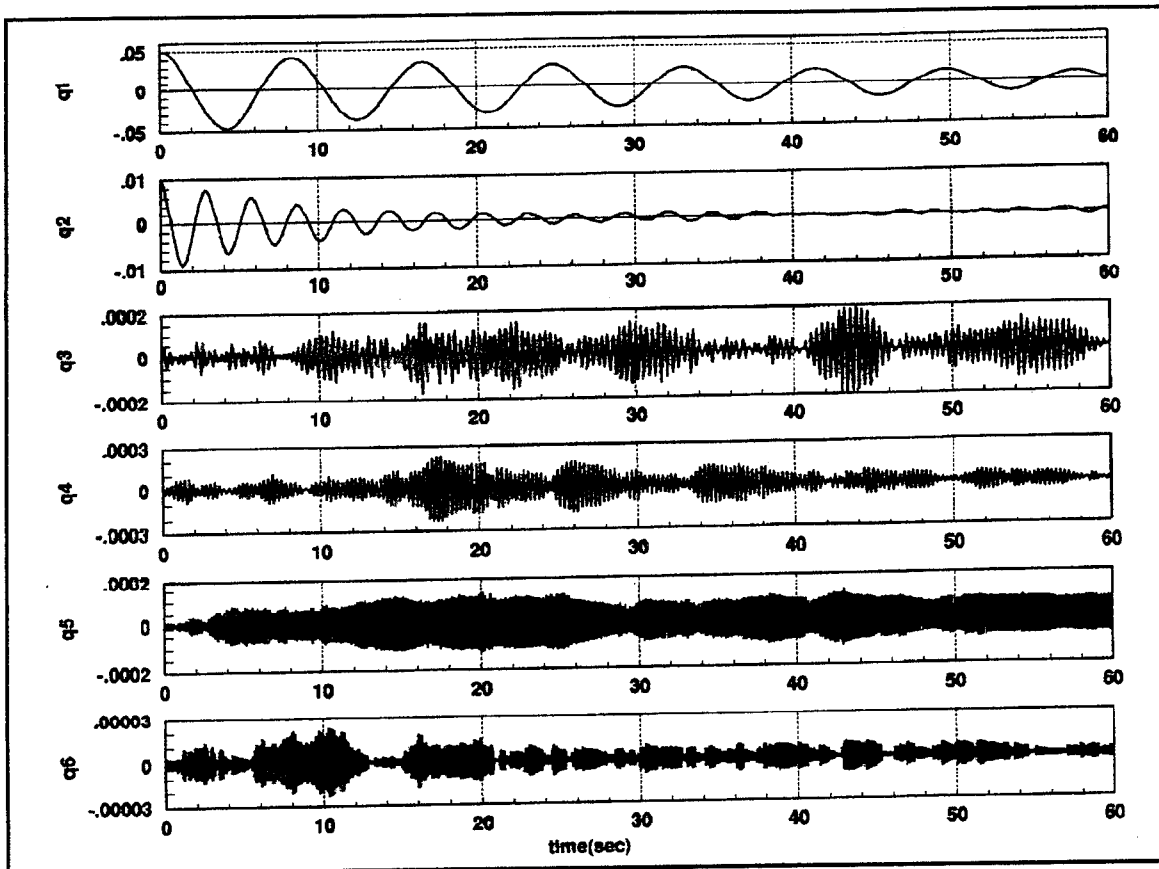
Figure 61. Initial Condition Modal Response, K=30, 20 msec Delay

The simulation of **Figures 62** and **63** was performed with no time delay. Note that after the thruster firing stops, the body oscillates at the first system mode frequency of .15 Hz. An important implication of on-off thruster control can be noted from the modal coordinate response. Note that each thruster firing excites the higher modes, and the modes ring down between pulses. This points out one of the shortcomings of trying to think of an on-off thruster system in linear response terms. Even though the output in θ appears to be typical of a sinusoidally forced linear system, each thruster pulse input to the plant actually has high frequency content, as we know from the trigonometric series expansion of a square wave. Note that the sampling rate of 100 Hz is six times the highest system frequency, so that proper capture of the q_6 dynamics is assured.

68
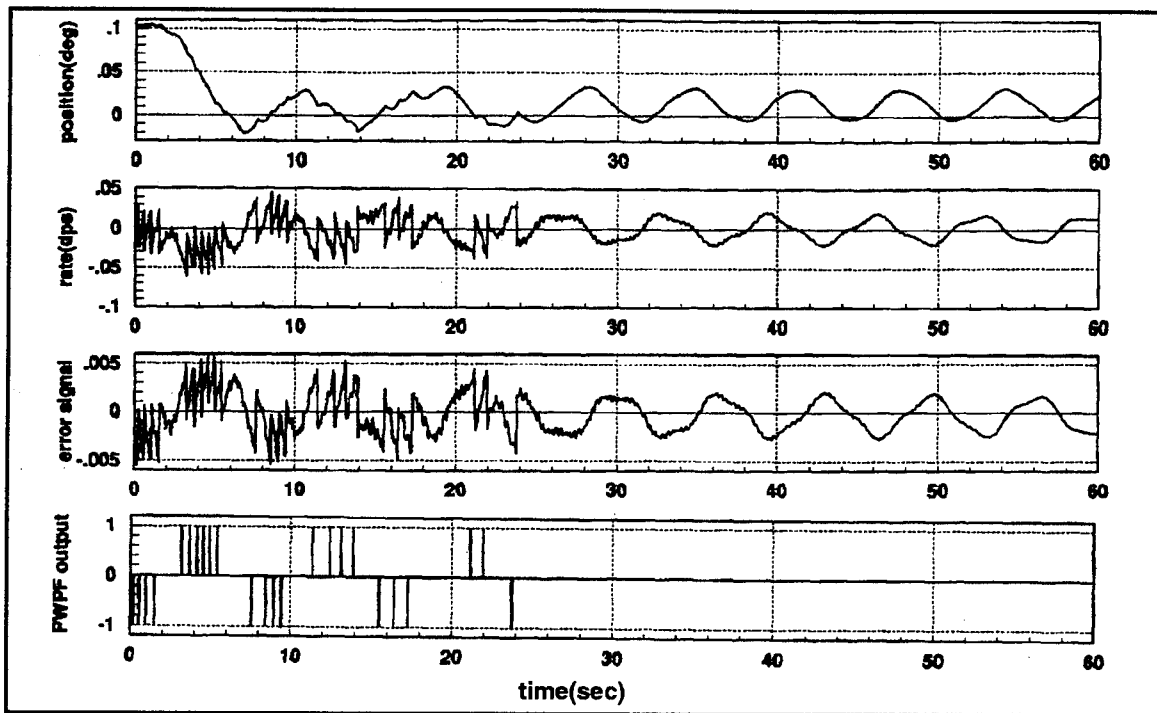
Figure 62. Initial Condition Response with K=30, No Delay
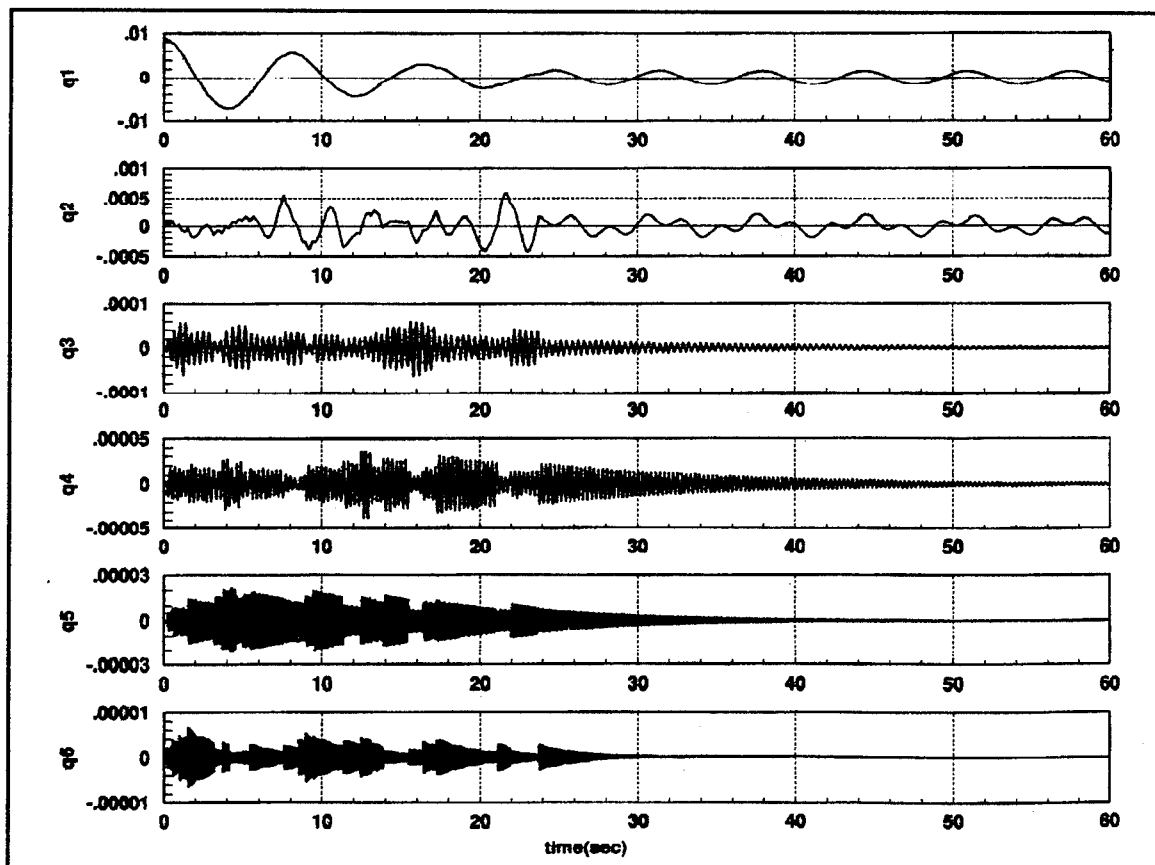
Figure 63. Initial Condition Modal Response with K=30, No Delay

69

Figures **64** and **65** show that a slew maneuver can still be performed in the presence of the third system-mode limit cycle.
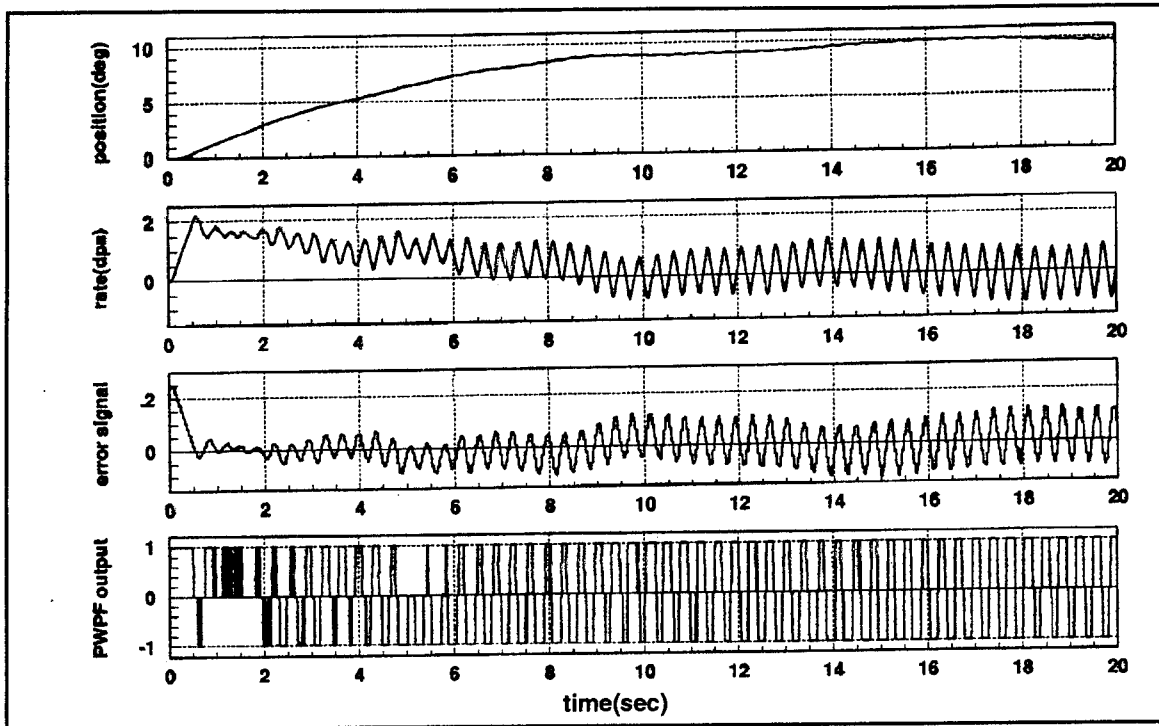
Figure 64. Slew Maneuver with K=30, 60 msec Delay
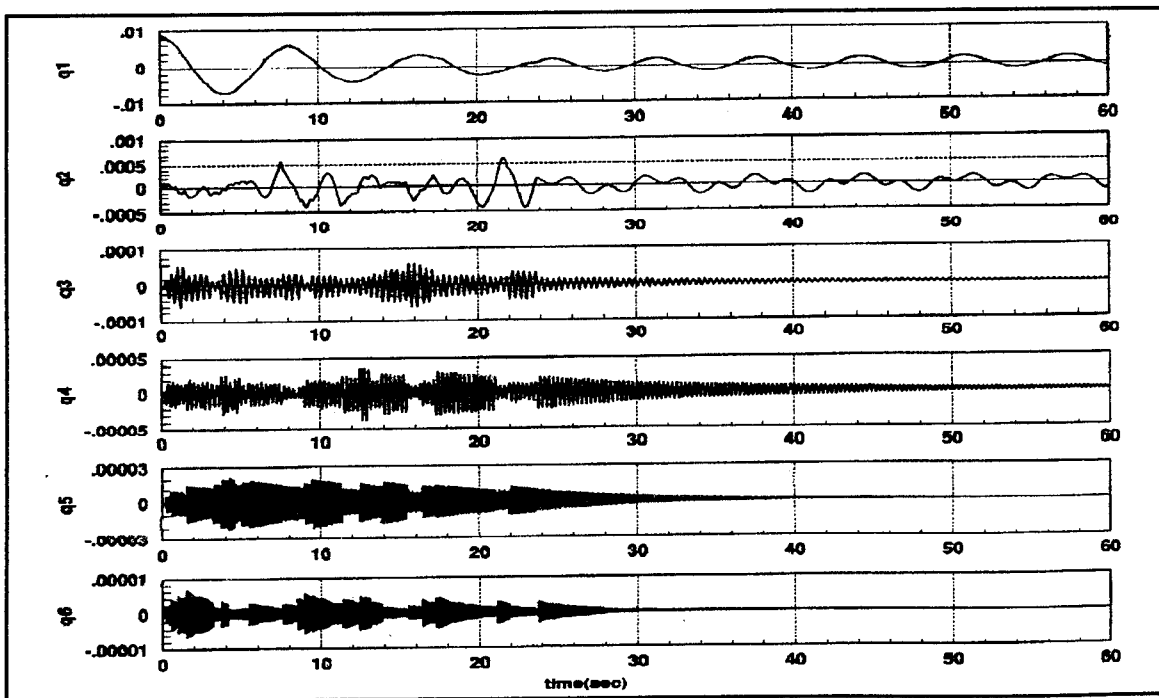
Figure 65. Slew Maneuver Modal Response, K=30, 60 msec Delay

70

The analysis was continued by considering a lower PWPF input gain, predicting the limit cycle frequency from the bode plot, then adding delay until limit cycling occurred. **Figure 66** is the linear bode plot with nonlinear boundary for the case K=10. For the case with K=30 the fourth and fifth system mode limit cycles were not excitable, hence the SIDF boundary is overly conservative. Assuming the same conservatism for the case K=10, it was predicted that only the second mode limit cycle would be evident. The predicted frequency from the bode plot is 5.5 rad/sec.
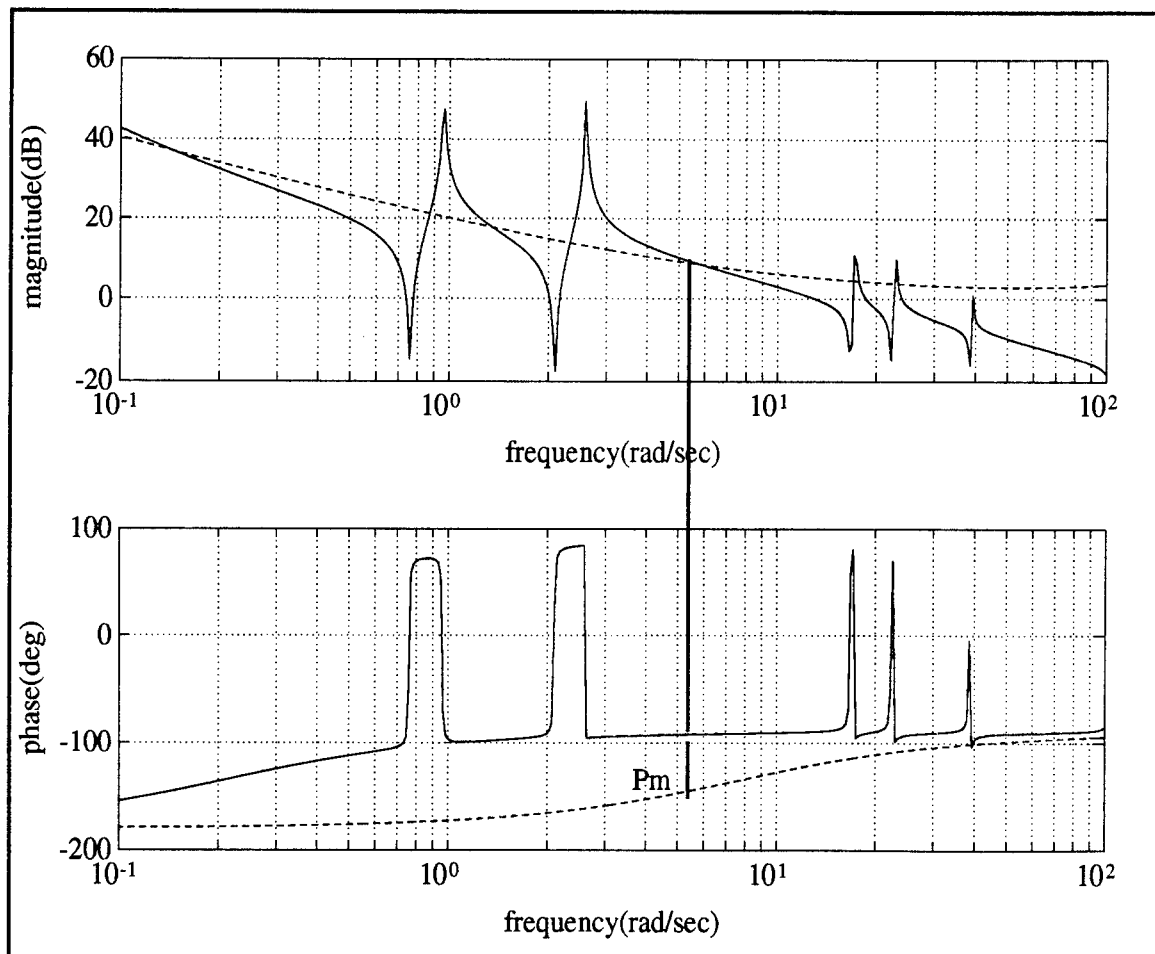
Figure 66. Loop Bode Plot With Nonlinear Boundary, K=10, No Delay

With a delay of 280 milliseconds, the gain margin with respect to the second mode limit cycle is eliminated (**Figure 67**). The gain attenuation after 10 rad/sec is due to the approximate model of the pure time delay.
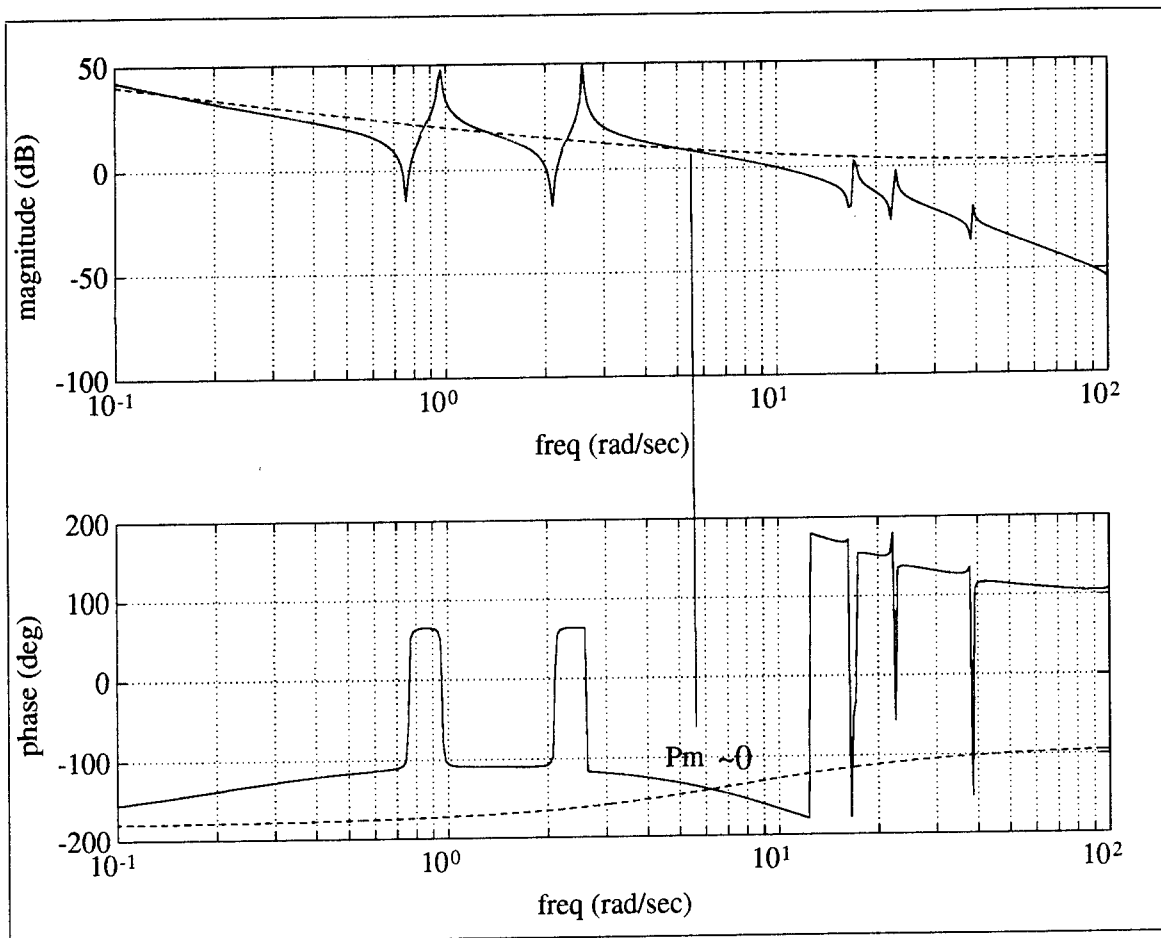
**Figure 67. Loop Bode Plot With Nonlinear Boundary
K=10, 280 msec Delay**

The predicted stability margin with respect to the second mode limit cycle was verified and the results are shown in **Figures 68** and **69**. The limit cycle frequency is 4.7 rad/sec (.75 Hz). Simulations were run with delays of up to 270 milliseconds, but limit cycle behavior was not established until 280 milliseconds of delay was added. The assumption that the SIDF formulation is conservative was once again verified as the third mode limit cycle could not be excited for the case K=10. Note that the limit cycle amplitude violates the pointing requirement.

72
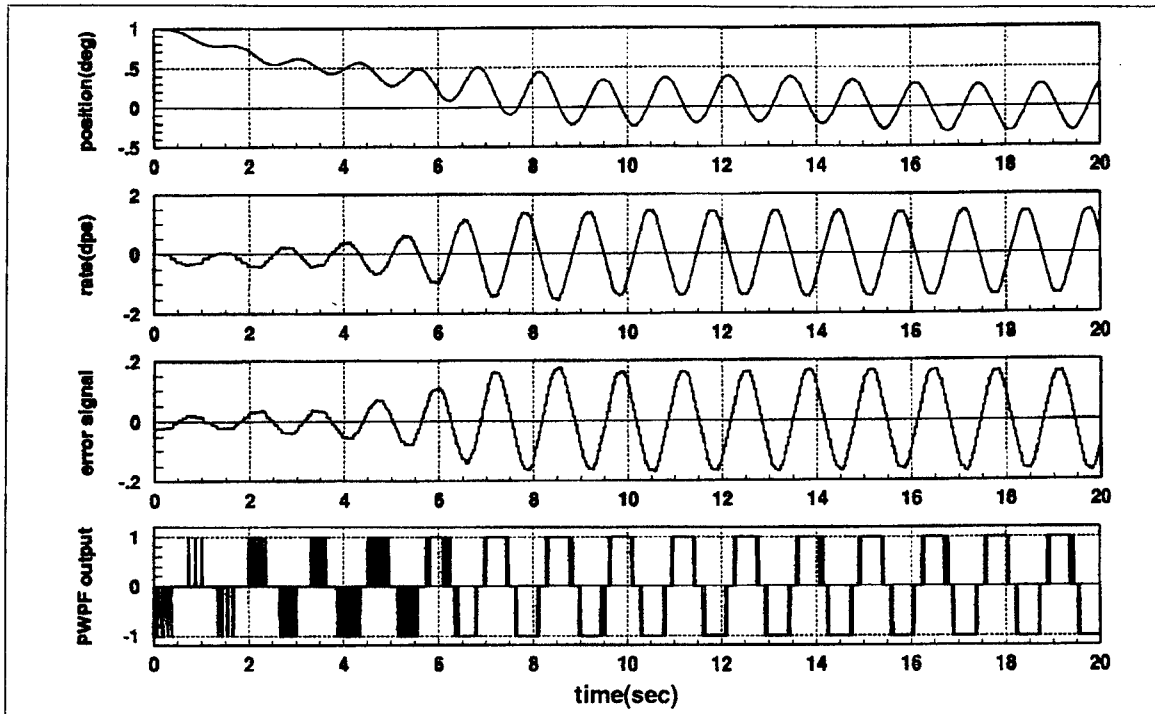
Figure 68.   Initial Condition Response with K=10, 280 msec Delay
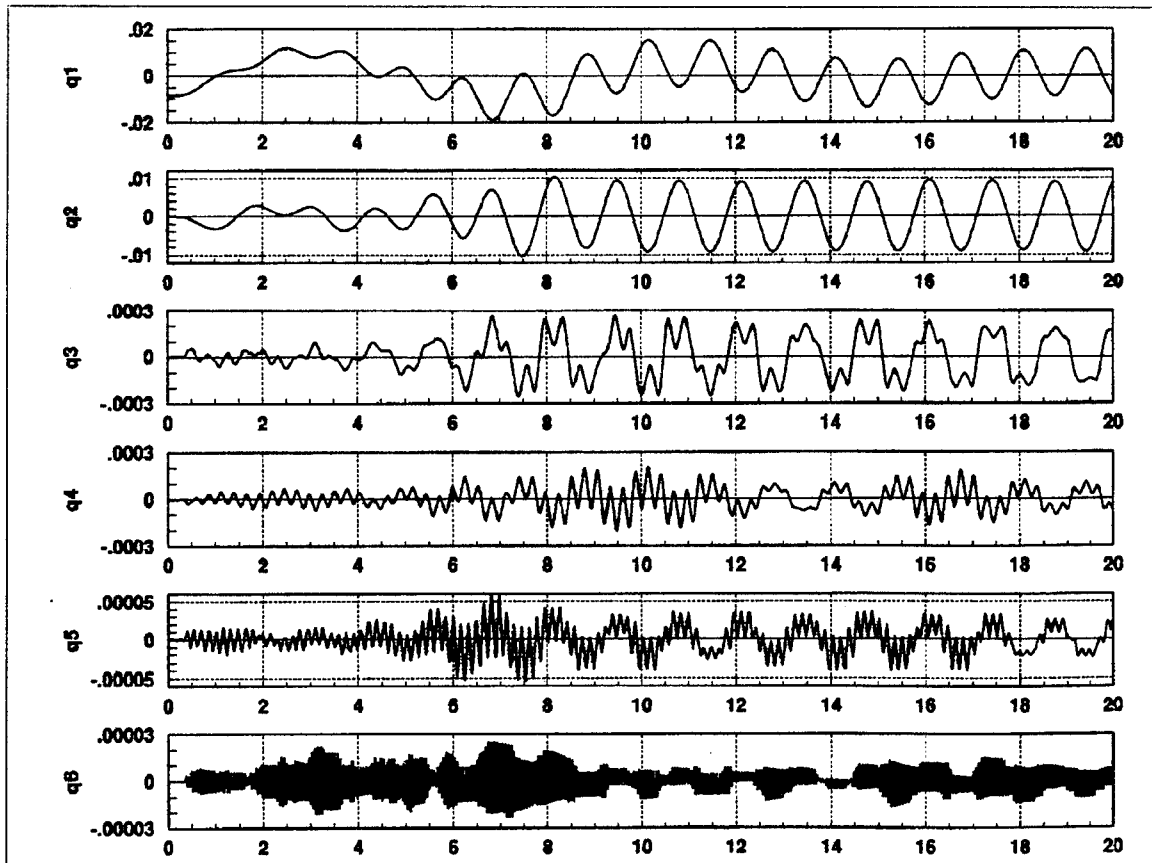
Figure 69.   Initial Cond. Modal Response, K=10, 280 msec Delay

73

This analysis has shown that the control-structure interaction predicted using the SIDF formula is overly conservative. The K=30 case predicts limit cycling near the fourth and fifth structural modes, and likewise with K=10 a third-mode interaction is still predicted. Since the describing function method is by definition an *approximate* method of predicting instability, this is acceptable. But the value of backing up the analysis with simulation is clearly demonstrated.

VI. CONCLUSIONS

A pulse-width pulse-frequency modulator has been successfully implemented and shown to provide pseudo-linear operation over a certain range of input. Simulations using the modulator indicate that this technique provides closer-to-linear actuation than conventional bang-bang thruster control methods. This facilitates a more tailorable response, which means that a single set of thrusters can be used to meet various control objectives. The resulting smoother control results in less thruster firing for identical maneuvers as compared to simple bang-bang and time-optimal bang-bang controllers.

Analysis of the control loop was shown to be important because of the interaction between the modulator nonlinearity with the flexible dynamics. Nonlinear describing function analysis proved to be useful in predicting flexible-mode limit cycle behavior.

A. RECOMMENDATIONS FOR FURTHER STUDY

• The PWPF modulator in this study required a fairly large input gain to provide adequate pointing accuracy. The resulting loop gain caused the bandwidth of the controller to overlap with flexible modes. The various elements of the modulator could be studied and further optimized for the specific system in hand in order to reduce the excitation to the structure introduced during maneuvers. Filtering of the first flexible mode (as in Reference 1) could also be applied.

• Operation of the PWPF modulator and comparisons to the performance of other controllers should be verified by experiments with the Flexible Spacecraft System.

• Use of thruster pulse modulation for momentum dumping should be investigated with the goal of reducing the angular offset noted in Reference 7.

• A combined-controller approach should be investigated. For instance, the minimum time solution could be implemented to provide initial slewing, with switching to a PWPF-modulated controller to avoid excessive thruster activity at the termination of the maneuver.

• The combination of center body control with active control of the flexible appendage using piezoelectric actuators and sensors is recommended. The "smart structures" experiments to date have been performed with the appendage cantilevered from a fixed center body. A multiple-input multiple-output controller could be developed which simultaneously considers end point control of the flexible appendage with the center body pointing control.

APPENDIX A

The following graphs depict the modulator output for various constant inputs.

PWPF Modulator Output for Constant Inputs

PWPF Modulator Output for Constant Inputs

PWPF Modulator Output for Constant Inputs

78
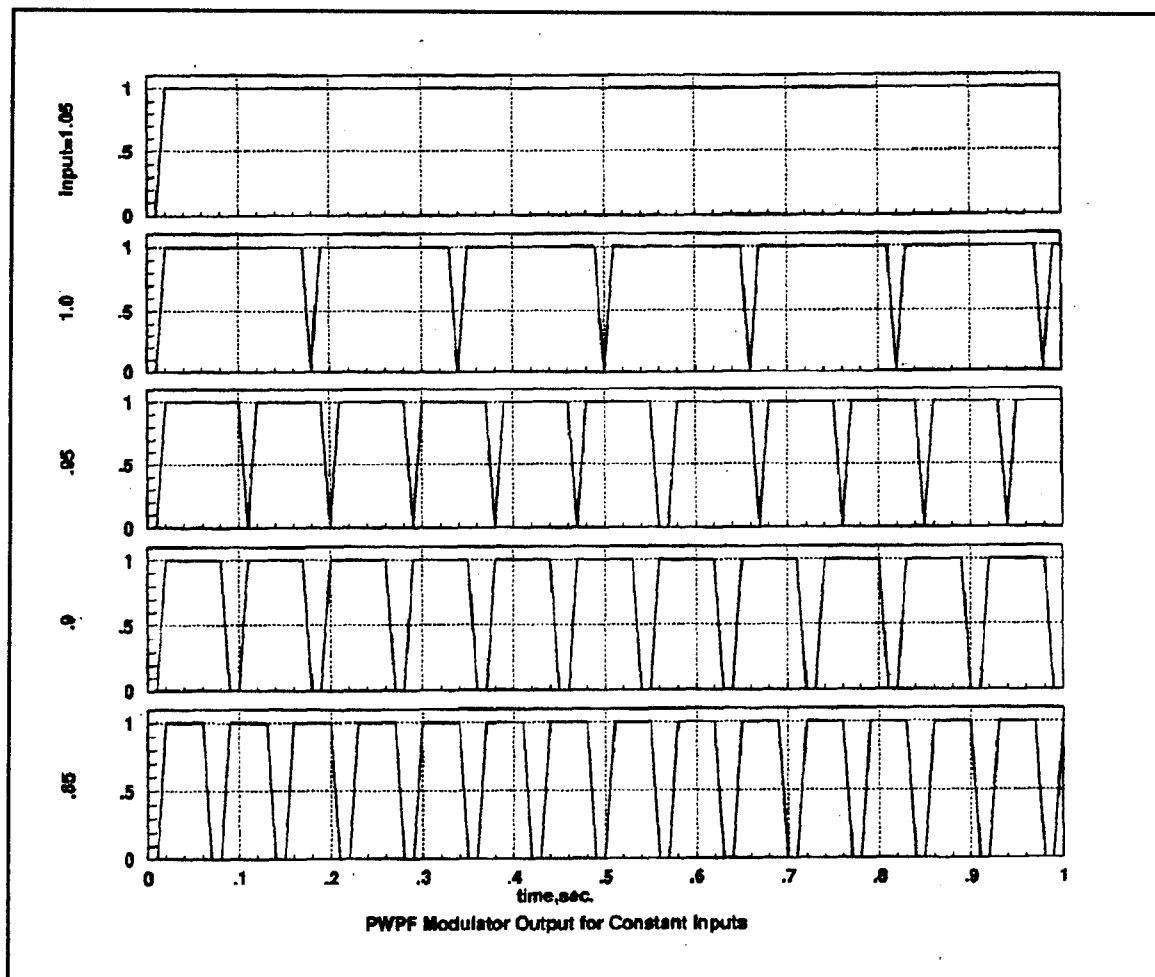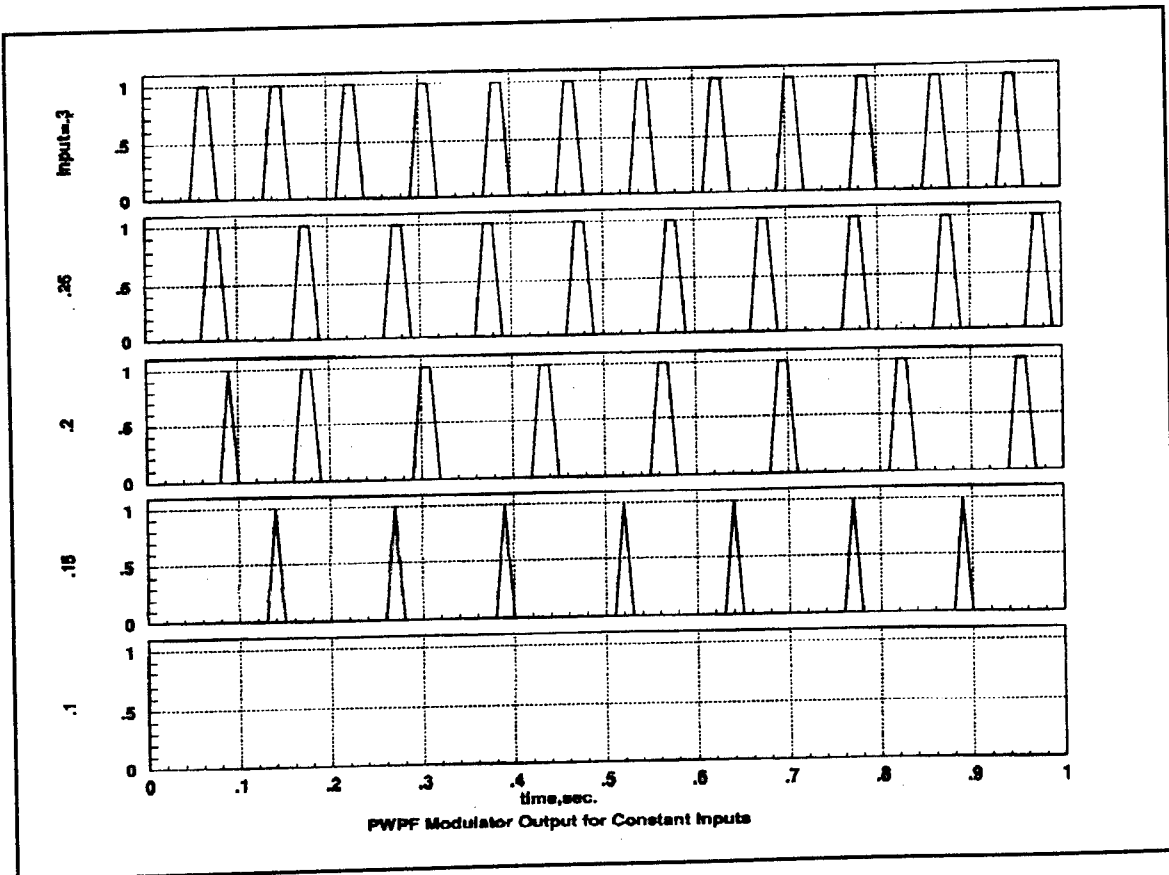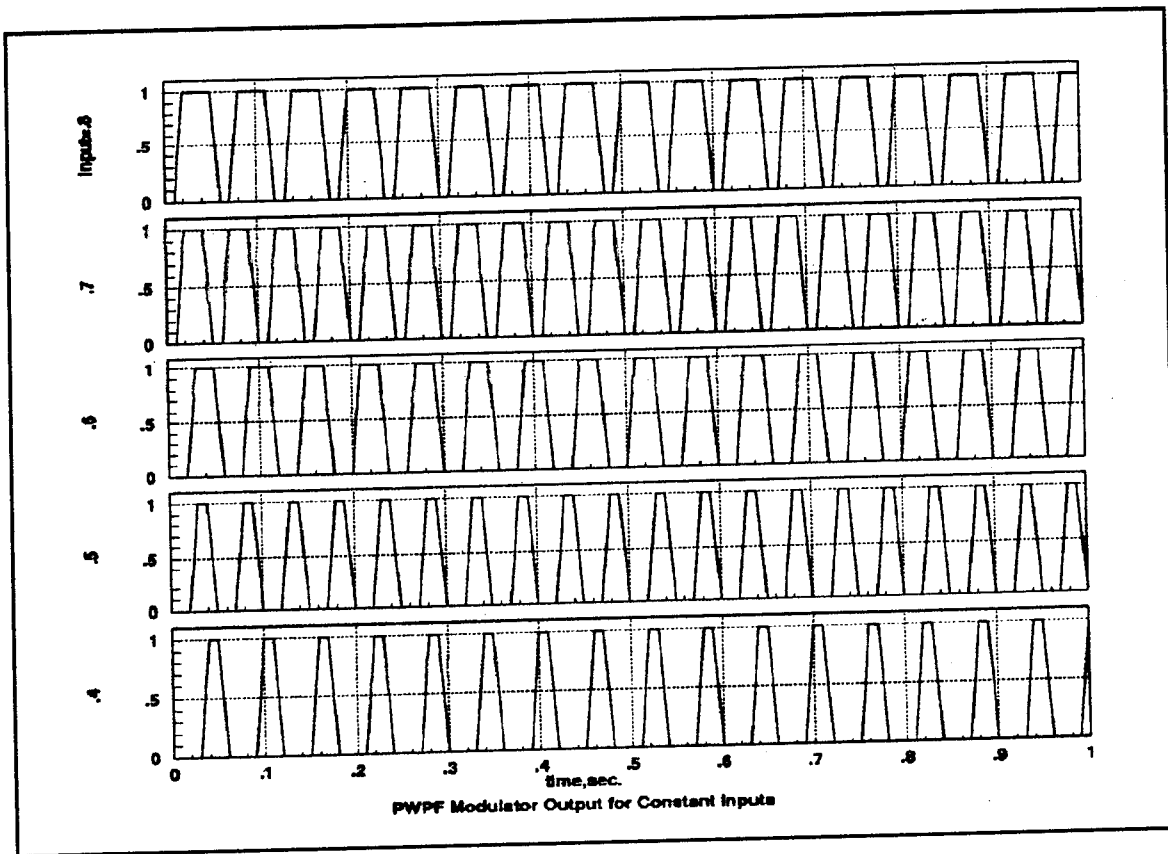
The following is a listing of the digital implementation of the PWPF modulator. The code was implemented within the format of the general Userblock subroutine (USR01.FOR). Refer to Figure 5 (Chapter 2) for definition of the parameters. The Userblock is implemented in simulations by first compiling the progam ($ FOR USR01) followed by linking ($ MWSLINK USR01) which creates an appended MWS executable file with default name MYMWS. Entrance into Systembuild is then accomplished using the command $MWS MYMWS. See Chapter 5 of the Matrix$_x$/Systembuild Modeling and Simulation manual for more information on Usercode Blocks.

```
c INITIALIZATION

      IF(TIME.EQ.0)THEN

c Modulator parameters
      K=4.5
      Tau= .12976
      lm=.54
      um=1
      uon= .45
      uoff= .15
      dt= .01

c limiter
      if(a1.gt.lm) a1= lm
      if(a1.lt.-lm) a1= -lm

c +fire (schmidt trigger)
      if(a1.gt.uon)then
       m17= 1.
       else
       m17=0.
       end if
      if(a1.gt.uoff)then
       n17=1.
       else
       n17=0.
       end if
      if((m17+n17).gt.0.) then
       o17=1.
       else
       o17=0.
       end if
```

79

```
c -fire (schmidt trigger)
      if(a1.lt.-uon)then
        p17=1.
        else
        p17=0.
       end if
      if(a1.lt.-uoff)then
        q17=1.
        else
        q17=0.
       end if
      if((p17+q17).gt.0.)then
        r17=1.
        else
        r17=0.
       end if

c initial output
        a3= um*(o17-r17)
        y(2)= a3    // y is output vector of Usercode Block
        go to 100
        END IF

c  MAIN LOOP

c new input u from simulation
        a2= u(1)

c filter
        a1= dt/Tau*K*(a2-a3) + a1old*(1.-dt/Tau)

c limiter
        if(a1.gt.lm) a1=lm
        if(a1.lt.-lm) a1=-lm

c + fire (schmidt trigger)
        if(a1.gt.uon) then
          m18=1.
          else
          m18=0.
         end if
        if(a1.gt.uoff)then
          n18=1.
          else
          n18=0.
         end if
        if((m18+n18*o17).gt.0.)then
          o18=1.
          else
          o18=0.
         end if

c - fire (schmidt trigger)
```

80

```fortran
      if(a1.lt.-uon)then
        p18=1.
         else
         p18=0.
       end if
      if(a1.lt.-uoff)then
        q18=1.
         else
         q18=0.
       end if
      if((p18+q18*r17).gt.0.)then
        r18=1.
         else
         r18=0.
       end if

c OUTPUT
      a3= um*(o18-r18)
      y(1)= a1
      y(2)= a3

c reassign the fire commands and filter output for next time step
      o17= o18
      r17= r18
      a1old= a1

100  RETURN
      end
```

The following listing of a sample simulation/ plotting routine is included for the benefit of the next Matrix$_x$ user. These routines help minimize the amount of time spent retyping/ modifying commands on the Matrix$_x$ command line. The program is accessed using <>\\edt filename, and executed using <>execute ('filename'). In the editor use 'ctrl z' to get back to the editor command line, 'quit' to exit without saving revisions, 'exit' to exit and save revisions, 'ch' to get back to editing.

```
dt=.01;
tmax=100;
t= [0:dt:tmax]';   // Define time vector
ll= 1;             // lower limit for graphs
ul= 6000;          // upper limit for graphs
u= ones(t)*10*pi/180;    // input for simulation (10° step)
y= sim(t, u);         // simulation command


plot(t(ll:ul),y(ll:ul,4),'upper left, ylabel/position(deg)/ xlabel/time(sec)/')
plot(t(ll:ul),y(ll:ul,3),'upper right, ylabel/rate(dps)/ xlabel/time(sec)/ date')
plot(y(:,4),y(:,3),'lower right, xlabel/posittion(deg)/ ylabel/ang vel/...
  title/phase plane trajectory/')
pause
hard  //hardcopy of plot
\\print/queue=ln03r matplot.ps


plot([t(ll:ul) t(ll:ul) t(ll:ul)], [y(ll:ul,9) y(ll:ul,10) y(ll:ul,11)],...   //strip chart plot
  'strip ylabel/q1lq2lq3/ xlabel/time(sec)/ ymin-1.2 ymax1.2')
pause
hard
\\print/queue=ln03r matplot.ps
```

APPENDIX B

Matrix$_X$/ Systembuild block diagrams

[multirate PWPF-modulated control loop]
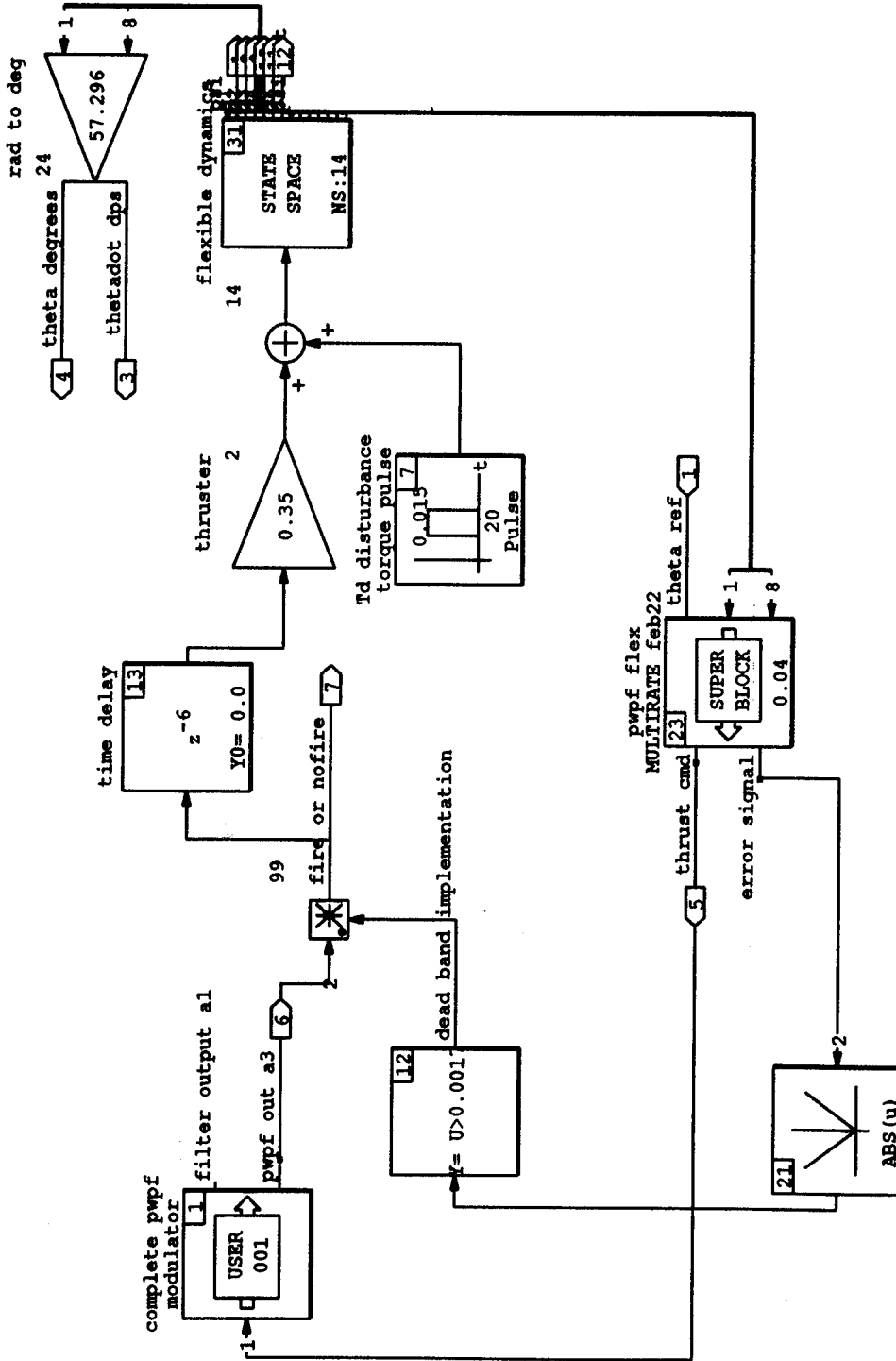
Discrete Super-Block
PWPF modulated ctrl multirate

| Sampling Interval | First Sample | Ext.Inputs | Ext.Outputs | Enable |
| 0.0100 | 0. | 1 | 12 | Parent |

rad to deg
57.296
theta degrees 24
thetadot dps
1
8
4
3

flexible dynamics
STATE SPACE   NS:14
31
14

thruster 2
0.35

Td disturbance torque pulse
7
0.015
20   Pulse
t

time delay 13
z^{-6}
Y0= 0.0

fire or nofire 7
99
2

dead band implementation 12
U= U>0.001

complete pwpf modulator
filter output a1
pwpf out a3
1
USER 001
6

pwpf flex
MULTIRATE feb22
theta ref
SUPER BLOCK
0.04
23
1
8

thrust cmd 5
error signal

ABS(u)
21
2
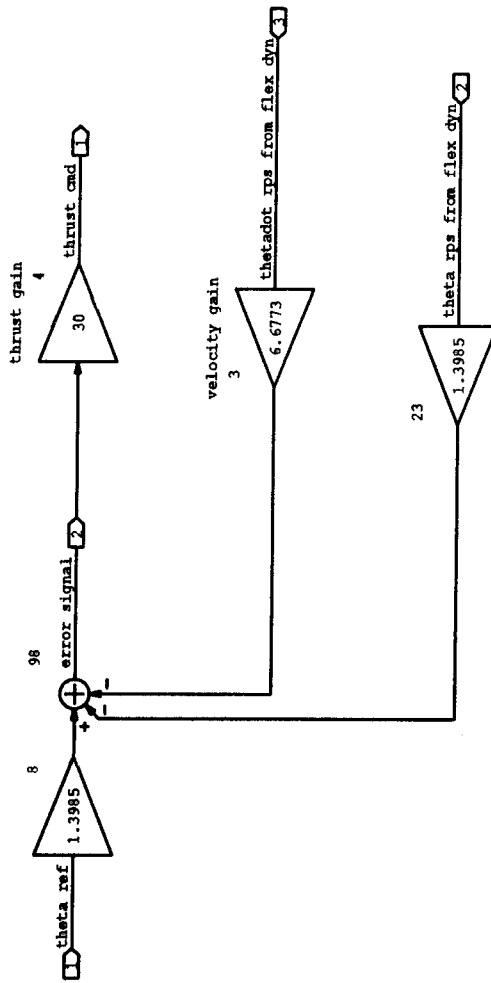
[multirate PWPF-modulated control loop (part 2)]

Discrete Super-Block
pwpf flex MULTIRATE feb22

Sampling Interval   First Sample
0.0400   0.

Ext.Inputs   Ext.Outputs   Enable
3   2   Parent

thrust cmd

thrust gain
4

30

thetadot rps from flex dyn 1

velocity gain
3

6.6773

theta rps from flex dyn 2

23

1.3985

error signal 2

98

+
−
+

8

theta ref 1.3985

84

Discrete Super-Block | Sampling Interval | First Sample | Ext. Inputs | Ext. Outputs | Enable
time optimal bang bang flexible | 0.0100 | 0. | 1 | 5 | Parent

[minimum-time bang-bang]

[simple bang-bang with deadband]
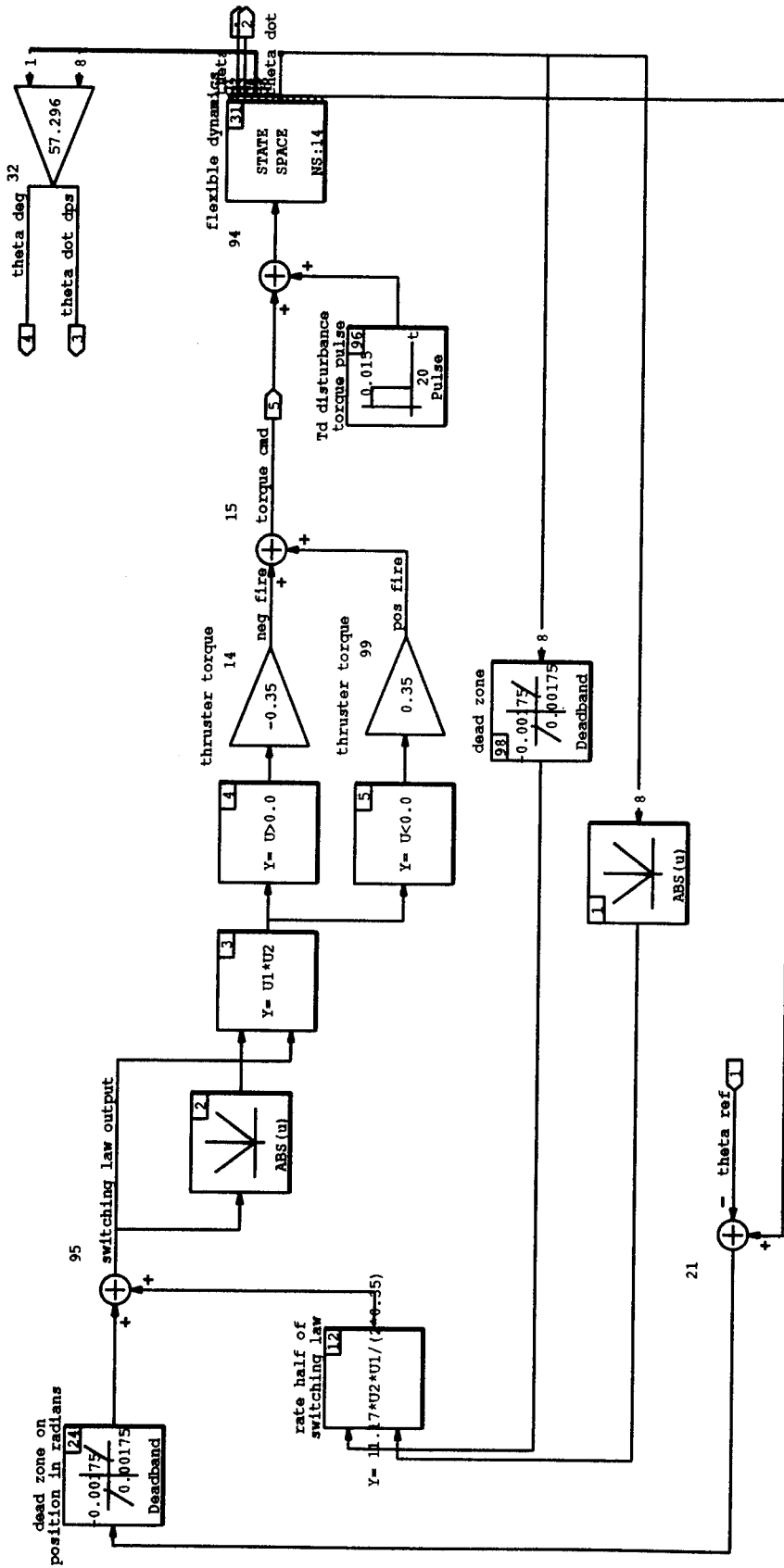
Discrete Super-Block
on off ctrl w d zone flex 29jan

	Sampling Interval	First Sample	Ext.Inputs	Ext.Outputs	Enable
	0.0100	0.	1	10	Parent

theta deg 32

57.296

theta dot dps

flexible dynamics

STATE
SPACE   NS:14

theta cmd

94   thrust cmd

Td disturbance
torque

97

y   0.015

Step

k1 x tau
23

6.6773   8

fire or nofire   2

92

THRUSTER TORQUE

4

0.35

m= 0.0
Preload

dead band   99

Y= U>0.005

112

ABS(u)

k1
3

1.3985   1

for unity DC gain
96

theta ref

1.3985

filter at
point96 rps   95

$$\frac{0.9971z^3 - 2.991z^2 + 2.99z - 0.9971}{z^4 - 2.994z^3 + 2.988z^2 - 0.9943z}$$

98

Attempts were made (unsuccessfully) to implement the PWPF modulator using a Usercode Block for the Schmidt trigger and Systembuild elements for the remainder of the loop.

Discrete Super-Block   Sampling Interval First Sample   Ext.Inputs Ext.Outputs   Enable
pwpf early implementation   0.0156   0.   1   4   Parent

schmidt trigger logic

| 14 |
| USER 001 |

3

Im _54

| 13 |
| 0.54 / -0.54 |
| Saturation |

2

fil27oct dt _015625

| 12 |
| $\dfrac{0.5105}{z - 0.8866}$ |

1

1

fil27oct zxform bythebook dt _01

| 3 |
| $\dfrac{34.679z}{z - 0.9258}$ |

filter z transformed old

| 2 |
| $\dfrac{8.9831(z+1)}{z + 0.77029}$ |

fil27oct dt _001

| 99 |
| $\dfrac{0.0345}{z - 0.9923}$ |

fil3novmatrixx ztrans 01562

| 95 |
| $\dfrac{0.5418z}{z - 0.8795}$ |

fil27oct dt _01

| 4 |
| $\dfrac{0.3338}{z - 0.9258}$ |

nov3 num den coef 0156 tustin

| 22 |
| $\dfrac{0.2555z + 0.2555}{z - 0.8864}$ |

fil27oct dt _015625

| 5 |
| $\dfrac{0.5105}{z - 0.8866}$ |

fil 3nov matrixx 0156 tustin

| 98 |
| $\dfrac{0.2555(z+1)}{z - 0.8864}$ |

fil3novmatrixx ztrans 01562

| 96 |
| $\dfrac{34.679z}{z - 0.8866}$ |

APPENDIX C

These Matlab programs were used for development of the loop transfer function and single input describing function (SIDF) boundary for analysis in the frequency domain.

```
%  The zeros of the plant transfer function correspond to the
%  eigenvalues of the appendage only, the cantilever frequecies (rad/sec):
z(1)= .76;  z(2)= 2.1;  z(3)= 16.7;
z(4)= 22.3; z(5)= 38.6; z(6)= 104.4;


%  Construct the plant transfer function numerator polynomial:
zeta= .004;   % .4 percent modal damping assumed
numplant= [1 2*zeta*z(1) z(1)^2];
denfactor= z(1)^2;
for i=2:6
      numplant= conv(numplant,[1 2*zeta*z(i) z(i)^2]);
      denfactor= denfactor*z(i)^2;
end


%  The poles of the plant transfer function correspond to the free-free or
%  system modes (rad/sec):
p(1)= .96;  p(2)= 2.6;  p(3)= 17.2;
p(4)= 22.8; p(5)= 39;  p(6)= 106;



%  Construct the plant transfer function denominator polynomial:
denplant= [1 2*zeta*p(1) p(1)^2];
numfactor= p(1)^2;
for i=2:6
      denplant= conv(denplant,[1 0 p(i)^2]);
      numfactor= numfactor*p(i)^2;
end
```

```
% Factor in the rigid body dynamics and the product-of-poles^2 to
% product-of-zeros^2 ratio:
Iest= 11.4;   % estimate of the total MOI
denplant= Iest*conv( denplant,[ conv([1 0],[1 0]) ] );
factor= numfactor/denfactor;
numplant= numplant*factor;


% Poles and zeros of transfer function (no control)
axis([-10 10 -150 150])
rlocus(numplant,denplant)  %title(' Poles and zeros of plant xfer function')
pause
clg
axis


% Bode plot of plant
w= logspace(-1,2,400);
bode(numplant,denplant,w), pause


% Now factor in the controller/feedback loop to form the loop xfer function
K= 10;              % PWPF modulator input gain
k= K*1.3985;         % forward loop gain
tau= 4.7746;         % factor for rate gain
numH= [tau 1];        % H is feedback loop
denH= 1;
numloop= k*conv(numplant,numH);     % combine plant and controller
denloop= conv(denplant,denH);
bode(numloop,denloop,w)         % Bode of loop xfer funtion, GH
pause
[maglinear,phaselinear,w]= bode(numloop,denloop,w);  %linear mag and phase
%[Gm,Pm,Wcg,Wcp]=margin(maglinear,phaselinear,w);    %linear margins


% Determine the SIDF boundary (magnitude and phase):
[magsidf,phasesidf]= sidf;   % calls function sidf
```

magsidf= magsidf+1.5; % corrected to reflect [Bayloc] experimental results

% Plot both linear mag and phase and nonlinear boundary:
 subplot(211),semilogx(w,magsidf,'--',w, 20*log10(maglinear)),grid
%title('Linear magnitude with SIDF boundary NO DELAY 24feb')
%gtext('Nonlinear Boundary') %gtext('Gm')
 xlabel('frequency(rad/sec)'),ylabel('magnitude(dB)')
 subplot(212),semilogx(w,phasesidf,'--',w,phaselinear),grid
%title('Linear phase with SIDF boundary')
%gtext('Nonlinear Boundary')
 gtext('Pm')
 xlabel('frequency(rad/sec)'),ylabel('phase(deg)')
 pause

% The pure time delay causes a phase lag which shrinks the nonlinear phase
% margin. Use sample and zero-order-hold formula from [Wie & Plescia]
T= .280; % 60 msec. delay
numdelay=[1];
dendelay= [T^2/12 T/2 1];

% augment numloop and denloop and calculate new magnitude and phase:
numloop=conv(numloop,numdelay);
denloop=conv(denloop,dendelay);
[maglinear,phaselinear,w]=bode(numloop,denloop,w); %linear mag and phase

% Plot both linear mag and phase and nonlinear boundary again for comparison:
clg
subplot(211),semilogx(w,magsidf,'--',w, 20*log10(maglinear)),grid
gtext('Nonlinear Boundary')
xlabel('freq (rad/sec)'),ylabel('magnitude (dB)')
subplot(212),semilogx(w,phasesidf,'--',w,phaselinear),grid
gtext('Nonlinear Boundary')
gtext('Pm ')
xlabel('freq (rad/sec)'),ylabel('phase (deg)')

90

SIDF subroutine:

```
function [magsidf,phasesidf]= sidf
% Modulator characteristics and SIDF analysis from [Wie]

% Static characteristics:
Uon= .45;
Uoff= .15;
h= Uon-Uoff;
del= .01;    %minimum pulse width
Um= 1;
Tm= .12976;
Km= 4.5;

% Calculate SIDF boundary gain and phase:
w=logspace(-1,2,400);
Am= ( Uon-h./( 1 + exp(del/Tm./w) ) ).*( ( sqrt(Tm.*w) ).^2 + 1 )/Km;
B1= 4/pi*Um*sin(del.*w/2);
B3= 4/3/pi*Um*sin(3*del.*w/2);
B= sqrt(B1.^2+B3.^2);

magsidf= -20.*log10(B./Am);

phasesidf= -180-( -57.3*atan(Tm.*w) );
```

REFERENCES

1.   Wie, B. and Plescia, C.T., "Attitude Stabilization of Flexible Spacecraft During Stationkeeping Maneuvers," *Journal of Guidance and Control*, Vol. 7, July-August 1984, pp. 430-436.

2.   Slotine, J.-J. E. and Li, W., *Applied Nonlinear Control*, Prentice-Hall, Englewood Cliffs, New Jersey, 1991, pp. 25-27, 157-188.

3.   Wertz, J. R., Editor, *Spacecraft Attitude Determination and Control*, Kluwer Academic Pub., Dordrecht, The Netherlands, 1978, pp. 655-659.

4.   Agrawal, B.N. and Bang, H., "Slew Maneuver of a Flexible Spacecraft Using On-Off Thrusters," *Proceedings of AIAA Guidance, Navigation, and Control Conference*, Monterey, California, August 1993, pp.224-233.

5.   Haloulakos, V.E., "Thrust and Impulse Requirements for Jet Attitude-Control Systems," *Journal of Spacecraft and Rockets*, Vol. 1, January 1964, pp. 84-90.

6.   Melcher, H.J. and Otten, D.D., "Modulating Bang-Bang Attitude Controls", *Control Engineering*, November 1965, pp. 73-75.

7.   Hailey, J. A., *Experimental Verification of Attitude Control Techniques for Flexible Spacecraft Slew Maneuvers*, Master's Thesis, Naval Postgraduate School, Monterey, California, March 1992.

8.   Agrawal, B.N., *Design of Geosynchronous Spacecraft*, Prentice-Hall, Englewood Cliffs, New Jersey, 1986, pp. 150-153.

9.   Martin, G.D., and Bryson Jr., A.E., "Attitude Control of a Flexible Spacecraft," Vol. 3, *Journal of Guidance and Control*, Jan.-Feb. 1980, pp. 37-41.

10.   Likins, P.W. and Fleisher, G.E., "Results of Flexible Spacecraft Attitude Control Studies Utilizing Hybrid Coordinates," *Journal of Spacecraft and Rockets*, Vol. 8, March 1971, pp. 264-273.

11.   Watkins Jr., R.J., *The Attitude Control of Flexible Structures*, Master's Thesis, Naval Postgraduate School, Monterey, California, June 1991.

12.   Franklin, G.F. and Powell, J.D., *Digital Control of Dynamic Systems*, Addison-Wesley Pub. Co., Reading, Mass., 1982.

13.   Dodds, S.J., and Williamson, S.E., "A Signed Switching Time Bang-Bang Attitude Control Law for Fine Pointing of Flexible Spacecraft," *International Journal of Control*, Vol. 40, 1984, pp. 795-811.

14.   Gelb, A., and Vander Velde, W.E., *Multiple-Input Describing Functions and Nonlinear System Design*, McGraw-Hill, New York, 1968.

15.   Yocum, J.F., and Slafer, L.I., "Control System Design in the Presence of Severe Structural Dynamics Interactions," *Journal of Guidance and Control*, Vol. 1, March-April 1978, pp. 109-116.

16.   Millar, R.A., and Vigneron, F.R., "Attitude Stability of a Pseudorate Jet-Controlled Flexible Spacecraft," *Journal of Guidance and Control*, Vol. 2, March-April 1979, pp. 111-118.

17.   Skaar, S.B., Tang, L., and Yalda-Mooshabad, I., "On-Off Control of Flexible Satellites," *Journal of Guidance and Control*, Vol. 9, July-August 1986, pp. 507-510.

18.   Dorf, R.C., *Modern Control Systems*, Addison-Wesley Pub. Co., Reading, Mass., 1992.

INITIAL DISTRIBUTION LIST

No. Copies

1. Defense Technical Information Center   2
   Cameron Station
   Alexandria, Virginia 22304-6145

2. Library, Code 52   2
   Naval Postgraduate School
   Monterey, California 93943-5002

3. Chairman, Code ME   1
   Department of Mechanical Engineering
   Naval Postgraduate School
   Monterey, California 93943

4. Chairman, Code SP   1
   Department of Aeronautics and Astronautics
   Naval Postgraduate School
   Monterey, California 93943

5. Professor Brij N. Agrawal, Code AA/Ag   2
   Department of Aeronautics and Astronautics
   Naval Postgraduate School
   Monterey, California 93943

6. Professor Morris Driels, Code ME/Dr   1
   Department of Mechanical Engineering
   Naval Postgraduate School
   Monterey, California 93943

7. Professor Robert G. Hutchins, Code EC/Hu   1
   Department of Electrical and Computer Engineering
   Naval Postgraduate School
   Monterey, California 93943

8. Mr. John P. Schaub   1
   Naval Research Laboratory, Code 8213
   4555 Overlook Ave., SW
   Washington, DC 20375-5320

9. Mr. Samuel Hollander   1
   Naval Research Laboratory, Code 8230
   4555 Overlook Ave., SW
   Washington, DC 20375-5320

10. Mr. Marvin Levenson   1
    Naval Research Laboratory, Code 8231
    4555 Overlook Ave., SW
    Washington, DC 20375-5320

11. Mr. Robert S. McClelland   2
    Naval Research Laboratory, Code 8213
    4555 Overlook Ave., SW
    Washington, DC 20375-5320